

Portable and Wearable Biomedical Devices for Pre-diagnosis, Detection, and Treatment

by

Xuanjie Ye

A thesis submitted in partial fulfillment of the requirements for the degree of

Doctor of Philosophy

in

Biomedical Engineering

Department of Electrical and Computer Engineering
University of Alberta

© Xuanjie Ye, 2023

Abstract

This dissertation explores portable, wearable biomedical devices, focusing on bioimpedance and low-intensity pulsed ultrasound (LIPUS) for pre-diagnosis, detection, and treatment. It includes five studies, three on bioimpedance and two on LIPUS. First, in the bioimpedance area, this dissertation investigates the feasibility of using bioimpedance measurement with a bipolar electrode configuration for knee injury assessment, demonstrating its potential for knee injury detection and monitoring. The second study presents an electrochemical impedance spectroscopy (EIS) based method for biomarker detection with the anti-SARS-CoV-2 IgG antibody being used as the biomarker in the study. The results show that this method can offer rapid response, high sensitivity, and minimal sample requirements. After that, the third study introduces the development of a portable, low-cost EIS system for point-of-care (POC) testing, showcasing excellent accuracy and precision in biosample measurements. Within the LIPUS domain, an interface chip for miniaturized LIPUS driver systems is presented. This chip integrates multiple modules onto a single chip so as to ensure the compatibility and low cost of the system. With an inductor-free design, the chip can be magnetic resonance imaging (MRI) compatible. The last study explores the effect of LIPUS with various parameter settings on promoting neuronal growth and nervous system regeneration. In sum, this dissertation advances portable and wearable biomedical devices, with significant implications for bioimpedance and LIPUS technologies in early diagnosis, biomarker detection, and treatment.

Preface

This dissertation is submitted in partial fulfillment of the requirements for the degree of Doctor of Philosophy at the University of Alberta. The research presented in this Ph.D. thesis was conducted at the Department of Electrical and Computer Engineering, University of Alberta, under the supervision of Professor Jie Chen between September 2018 and April 2023. Some chapters incorporate published articles that I have authored or co-authored. The authors' contributions to the associated published articles are delineated as follows:

Chapter 2 of this thesis encompasses research published in IEEE Transactions on Biomedical Circuits and Systems 16, no. 5 (2022): 962-971 as "Bioimpedance measurement of knee injuries using bipolar electrode configuration" by Xuanjie Ye, Lexi Wu, Kaining Mao, Yiwei Feng, Jiajun Li, Lei Ning, and Jie Chen. I spearheaded the experimental design, measurements, data acquisition, data interpretation, and manuscript composition. Lexi Wu assisted in data collection. Kaining Mao, Yiwei Feng, and Jiajun Li contributed to the data analysis. Dr. Jie Chen and Lei Ning provided supervision, guidance, and manuscript revision.

Chapters 3 and 4 of this thesis embody research published in Biosensors and Bioelectronics: X 13 (2023): 100301 as "A portable, low-cost and high-throughput electrochemical impedance spectroscopy device for point-of-care biomarker detection" by Xuanjie Ye, Tianxiang Jiang, Yuhao Ma, Daniel To, Shuren Wang, and Jie Chen. I led the experimental design, measurements, data acquisition, data interpretation, circuit design, hardware prototyping, debugging, and manuscript composition. Shuren Wang participated in hardware troubleshooting. Tianxiang Jiang, Yuhao Ma, and Daniel To were responsible for conducting experiments and preparing materials. Dr. Jie Chen supervised the work, offered valuable project guidance, and contributed to manuscript review and editing.

Chapter 5 of this thesis has been submitted for review to IEEE Transactions on Very Large Scale Integration Systems as "A Low-Intensity Pulsed Ultrasound Interface ASIC Chip for Wearable Medical Therapeutic Device Applications" by Xuanjie Ye, Xiaoxue Jiang, Shuren Wang, and Jie Chen. I took the lead in experimental design, measurements, data acquisition, data interpretation, chip schematic design, hardware prototyping, debugging, and manuscript composition. Xiaoxue Jiang was involved in chip schematic and layout design, as well as simulation. Shuren Wang contributed to hardware troubleshooting. Dr. Jie Chen supervised the work, provided valuable project guidance, offered insights on the biomedical applications of the prototype, and contributed to manuscript review and editing.

Chapter 6 of this thesis has been submitted for review to Nature Mental Health as " Low-intensity Pulsed Ultrasound Enhances Neurite Growth in Serum-starved Human Neuroblastoma Cells" by Xuanjie Ye, Zitong Wang, Rebekah van Bruggen, Yanbo Zhang, and Jie Chen. I was responsible for the design and execution of experiments, data analysis, and manuscript development. Zitong Wang and Rebekah van Bruggen offered guidance in experimental design and data interpretation. Dr. Jie Chen and Dr. Yanbo Zhang supervised the work, provided valuable guidance, and revised the manuscript.

The content of this dissertation underwent polish and proofreading using the software tools Grammarly and QuillBot to ensure its linguistic accuracy.

Acknowledgments

First, and most importantly, I would like to express my heartfelt appreciation and gratitude to my dear supervisor, Prof. Jie Chen, for providing me with the valuable opportunity to pursue the Doctor of Philosophy degree at the University of Alberta. He accepted me as his graduate student and allowed me to work in his research team under his guidance, which was the beginning of my academic career. His help, patience, and encouragement have been valuable in my growth as a researcher. He believed in me and always encouraged me, helping me to do my best in my field.

I would also like to show my sincere appreciation to Prof. Bruce Cockburn, Prof. Kambiz Moez, and Prof. Adetola Adesida. They helped a lot during my candidacy examination. Their insightful suggestions, careful evaluation, and challenging questions have helped me to improve and develop my research perspective and methodology.

In addition, I extend sincere thanks to Xiaoxue Jiang, Yufeng Li, Shiang Qi, Kaining Mao, Jiajun Li, Shuren Wang, Tianxiang Jiang, and Zitong Wang, my lab colleagues who provided a conducive environment that facilitated learning as well as extended help whenever it was needed. Their friendship has made this journey both enjoyable and rewarding.

I feel indeed fortunate to have the opportunity to work, learn, and grow with these learned people. I appreciate all of them from the bottom of my heart for their help in my academic journey and personal growth.

Finally, I also want to acknowledge myself for persevering through difficult times which contributed immensely toward reaching where I stand today.

Table of Contents

Abstract.....	ii
Preface.....	iii
Acknowledgments	v
Table of Contents	vi
List of Tables	ix
List of Figures.....	x
List of Abbreviations	xiii
1. Introduction.....	1
1.1 Background of Portable and Wearable Medical Devices.....	1
1.2 Bioimpedance	3
1.3 Low-intensity Pulsed Ultrasound	7
1.4 Contribution and Novelty of This Thesis.....	13
1.5 Thesis Outline.....	14
2. Bioimpedance Measurement of Knee Injuries using Bipolar Electrode Configuration ..	16
2.1 Introduction.....	16
2.1.1 Knee Injury Diagnosis Methods	16
2.1.2 Fundamentals of Knee Injury Diagnosis Based on Bioimpedance.....	17
2.1.3 Current Research Status of Knee Injury Diagnosis Based on Bioimpedance.....	22
2.1.4 Contribution of This Study	24
2.2 Materials and Methods.....	25
2.2.1 Feasibility Study of the Bipolar Electrode Configuration	25
2.2.2 Bioimpedance Measurement of Knee Injuries	27
2.3 Results	29
2.3.1 Feasibility Study of the Bipolar Electrode Configuration	29
2.3.2 Bioimpedance Measurement of Knee Injuries	32
2.4 Discussion.....	35
2.4.1 Implications from the Feasibility Study of Bipolar Electrode Configuration	35
2.4.2 Detection of Knee Injuries Based on the Bioimpedance.....	37
2.5 Conclusion	39

3. Electrochemical Impedance Spectroscopy Based Point-of-care Biomarker Detection: A Case Study on SARS-CoV-2 Detection	41
3.1 Introduction	41
3.2 Materials and Methods	45
3.2.1 Detection Principles	45
3.2.2 Materials	46
3.2.3 IDE Chip Design and Manufacture	46
3.2.4 Surface Functionalization of S Protein	48
3.2.5 Formation of GNP	48
3.2.6 Surface Characterization of GNP	49
3.2.7 Verification of IgG Antibody Interaction with the SARS-CoV-2 Spike Protein .	49
3.3 Results and Discussion	51
3.4 Conclusion	53
4. A Portable and Low-cost Electrochemical Impedance Spectroscopy System for Point-of-care Testing	55
4.1 Introduction	55
4.2 Hardware and Algorithm Design	58
4.2.1 Analog Front-End Circuit Design	60
4.2.2 Digital Circuit Design	62
4.2.3 Excitation Signal Design	64
4.3 Results and Discussion	69
4.3.1 Multi-tone Signal Synthesis	69
4.3.2 Measurement Performance Evaluation	71
4.4 Conclusion	75
5. A Low-Intensity Pulsed Ultrasound Interface ASIC Chip for Miniaturized Medical Therapeutic Device Applications	77
5.1 Introduction	77
5.2 System Design	80
5.2.1 Charge Pump	81
5.2.2 High Voltage Level Shifter	84
5.2.3 Voltage-Controlled Oscillator	86
5.2.4 Half-bridge Driver	87

5.3 Results and Discussion	89
5.3.1 Simulation Results	90
5.3.2 Test Results	97
5.3.3 Discussion	101
5.4 Conclusion	103
6. Exploring the Potential of Low-Intensity Pulsed Ultrasound for Neural Cell Growth Promotion and Nervous System Regeneration: An In-vitro Study	105
6.1 Introduction	105
6.2 Materials and Methods	108
6.2.1 LIPUS Exposure System	108
6.2.2 Cell Culture and LIPUS Treatment	110
6.2.3 Cell Cytotoxicity Quantification	112
6.2.4 Cell Visualization	113
6.2.5 Western Blot	114
6.2.6 Statistical Analysis	115
6.3 Results and Discussion	115
6.3.1 Effect of LIPUS on Cell Proliferation in SK-N-SH Cells	115
6.3.2 Effect of LIPUS on Neurite Outgrowth in SK-N-SH Cells	117
6.3.3 Effect of LIPUS on Signaling Transduction in SK-N-SH Cells	122
6.3.4 The Impact of Different LIPUS Parameters	125
6.4 Conclusion	127
7. Conclusions and Future Work	129
References	134

List of Tables

Table I Dielectric properties of the components at 100 kHz [137, 143-145]	20
Table II Anthropometric characteristics of the patient group and the control group.....	32
Table III T-test results of ΔZ_p and ΔZ_h at different frequencies.....	33
Table IV Crest Factor Optimization Results Using Various Algorithms	70
Table V Evaluation of Accuracy and Precision for the Proposed EIS System Using Resistors. .	72
Table VI Comparison of Specifications.....	75
Table VII Transistor parameters of different modules in the system	90
Table VIII Post-layout simulation performance results.....	96
Table IX Comprehensive overview of the system performance for the proposed LIPUS chip.	100
Table X Comparison with other similar state-of-art works ICs.....	102

List of Figures

Figure 1.1 Demonstration of the relationship between the current through biological tissue and the frequency.....	4
Figure 1.2 Demonstration of a LIPUS wave and its essential parameters.....	8
Figure 2.1 The anatomy of a right knee (Figure source: https://www.webmd.com/pain-management/knee-pain/picture-of-the-knee).....	18
Figure 2.2 (a) the locations of the bursae around the knee joint (source: https://www.midliferunning.com/knee-bursitis.html) (b) the synovial membrane of the knee joint (source: https://www.arthritis-health.com/types/joint-anatomy/knee-anatomy).....	19
Figure 2.3 (a) Electrode placement in Neves’s study [134]. (b) Electrode placement in Hersek’s study [159].	23
Figure 2.4 (a) Illustration of the positions of Xiyan (reproduced from [165]). (b) The placement of bipolar electrodes on Xiyan in a real test (reproduced from [166]). (c) Setup for the bioimpedance measurement (not to scale) (reproduced from [166]).....	26
Figure 2.5 The mean and standard deviation of bioimpedance reduction percentages across various DS segments over a frequency range of 100 Hz to 1 MHz (reproduced from [166]).....	30
Figure 2.6 Bioimpedance measurements of left and right knees for three healthy individuals taken at 5-minute DS on four consecutive days, presented across a frequency range of 100 Hz to 1 MHz. (reproduced from [166]).	31
Figure 2.7 Box plots of the relative bioimpedance differences ΔZ_p and ΔZ_h at all frequency nodes, where the abbreviation SFSP(s) denotes significant frequency sampling point(s) (reproduced from [166]).	34
Figure 2.8 Principal components of the patient and control groups’ SFSPs generated by PCA, along with the predictor created using SVM in the 2D plane (reproduced from [166]).....	35
Figure 2.9 Equivalent circuit model in bioimpedance measurement: (a) Equivalent circuit model, and (b) Evolution of primary equivalent circuit elements representing external factors across a frequency range from low (DC) to high (>1MHz). Both were reproduced from [166].	36
Figure 3.1 Overall representation of the proposed EIS-based method for biomarker detection utilizing an IDE chip (reproduced from [201]).....	43
Figure 3.2 The mechanism of anti-SARS-CoV-2 IgG detection in serum samples using the IDE chip (reproduced from [201]).....	45
Figure 3.3 IDE biosensor and its micrograph (reproduced from [201]).....	47
Figure 3.4 Fluorescence microscopy images of IDE chips: (a) control without serum exposure, (b) incubated with SARS-CoV-2 positive serum sample, and (c) incubated with SARS-CoV-2 negative serum sample (reproduced from [201]).....	50

Figure 3.5 $ \Delta Z $ between serum incubation and GNP binding steps for positive and negative samples across a frequency range of 10 Hz to 1 MHz (N = 12) (reproduced from [201]).	51
Figure 4.1 (a) Comprehensive circuit block diagram of the EIS system. (b) Prototype of the proposed EIS system. Both were reproduced from [201].	58
Figure 4.2 Flow chart of the impedance measurement process (reproduced from [201]).	59
Figure 4.3 (a) Block diagram of traditional potentiostat topology (b) Block diagram of automatic balance bridge topology (reproduced from [201]).	61
Figure 4.4 (a) Time-frequency domain swapping algorithm (b) Time-frequency domain swapping algorithm revised by Yang <i>et al.</i>	66
Figure 4.5 Performance Assessment of the Proposed EIS System with an IDE Chip Immersed in PBS Solution (reproduced from [201]).	74
Figure 5.1 Comparison of the Highly Integrated LIPUS System with a Canadian Two-Dollar Coin.	79
Figure 5.2 Proposed ASIC Chip System Architecture and Associated Peripheral Components.	81
Figure 5.3 (a) 4-stage charge pump topology. (b) Operation timing of a typical unit CTS MA2.	82
Figure 5.4 Schematic representation of the HVLS and explanation of its functioning.	84
Figure 5.5 Circuit diagram of the 3-stage CSVCRO	86
Figure 5.6 Schematic of the dead time generator and its corresponding waveform illustrating the generated timing intervals.	88
Figure 5.7 Micrograph of the bare die and its brief floor plan	89
Figure 5.8 Post-layout simulation results of the charge pump under varying loads and clock frequencies: (a) Output power and efficiency comparison; (b) Ripple voltage and startup time comparison.	91
Figure 5.9 Post-layout transient simulation result of the HVLS.	92
Figure 5.10 Post-layout simulation results illustrating the frequency-voltage characteristics of the CSVCRO.	93
Figure 5.11 The brief schematic of the ASIC chip post-layout simulation.	94
Figure 5.12 Post-layout simulation results depicting the output voltage waveforms for the charge pump (V _{PP}) and the HB driver (V _{SW}) with power supplies of (a) 3.7 V and (b) 5 V.	95
Figure 5.13 Microsecond-scale waveforms depicting the voltage on the load (V _{load}), the output voltage of the charge pump (V _{PP}), and the current on the load (I _{load}) using power supplies of (a) 3.7 V and (b) 5 V.	98
Figure 5.14 Millisecond-scale waveforms depicting the voltage on the load (V _{load}), the output voltage of the charge pump (V _{PP}), and the current on the load (I _{load}) using power supplies of (a) 3.7 V and (b) 5 V.	99
Figure 6.1 Overview of the LIPUS exposure setup.	109

Figure 6.2 LIPUS stimulation methodology (Created with BioRender.com).	109
Figure 6.3 LDH result of different groups (N=3). The results were normalized to the complete media group.	116
Figure 6.4 Representative ICC images of SK-N-SH cells subjected to different LIPUS treatment conditions: (A) Complete Media; (B) Starving control; (C) Treatment A 50 mW/cm ² , 40%; (D) Treatment B 25 mW/cm ² , 20%; (E) Treatment C 50 mW/cm ² , 20%; (F) Treatment D 25 mW/cm ² , 10%.	119
Figure 6.5 Quantified data representing the average neurite length (μm) for different treatment groups (N=90).	120
Figure 6.6 Hypothesized signaling pathway under LIPUS stimulation (Created with BioRender.com).	122
Figure 6.7 Comparison of normalized band intensity of Western Blot among different treatment groups (N=3) : (A) BDNF, (B) mTOR, (C) ERK1/2, (D) Akt.	123
Figure 6.8 Representative Western Blot image illustrating the expression levels of GAPDH, BDNF, p-mTOR, mTOR, p-ERK1/2, ERK1/2, p-Akt, and Akt.	124

List of Abbreviations

Alternating current (AC)

Analog front-end (AFE)

Analog-to-digital converter (ADC)

Analysis of variance (ANOVA)

Anterior cruciate ligament (ACL)

Application-specific integrated circuit (ASIC)

Artificial bee colony (ABC)

Bacterial Foraging Optimization (BFO)

Bioelectrical impedance analysis (BIA)

Bioimpedance spectroscopy (BIS)

Body mass index (BMI)

Bovine serum albumin (BSA)

Brain-derived neurotrophic factor (BDNF)

Charge transfer switch (CTS)

Chronic obstructive pulmonary disease (COPD)

Complementary Metal-Oxide-Semiconductor (CMOS)

Crest factor (CF)

Current-starved voltage-controlled ring oscillator (CSVCRO)

Device under test (DUT)

Digital-to-analog converter (DAC)

Direct digital synthesis (DDS)

Discrete Fourier transform (DFT)

Dulbecco's Modified Eagle Medium (DMEM)

Duration of sticking (DS)

Electrocardiogram (ECG)

Electrochemical impedance spectroscopy (EIS)

Enzyme-linked immunosorbent assay (ELISA)

Extracellular fluid (ECF)

Extracellular signal-regulated kinase (ERK)

Fast Fourier Transform (FFT)

Fetal bovine serum (FBS)

Field-programmable gate array (FPGA)

Flower Pollination Algorithm (FPG)

Food and Drug Administration (FDA)

Genetic algorithm (GA)

Glyceraldehyde 3-phosphate dehydrogenase (GAPDH)

Gold nanoparticle (GNP)

Gold nanoparticle conjugated with protein G (GNP-G)

Half-bridge (HB)

High-voltage (HV)

High-voltage level shifter (HVLS)

Immunocytochemistry (ICC)

Lactate dehydrogenase (LDH)

Interdigitated micro-electrode (IDE)

Integrated circuit (IC)

Intracellular fluid (ICF)

Inverse discrete Fourier transform (IDFT)

Isopropyl alcohol (IPA)

Lab-on-chip (LOC)

Lateral collateral ligament (LCL)

Leave-one-out cross-validation (LOOCV)

Low-dropout (LDO)

Low-intensity pulsed ultrasound (LIPUS)

Magnetic resonance imaging (MRI)

Mammalian target of rapamycin (mTOR)

Medial collateral ligament (MCL)

Mitogen-activated protein kinase (MAPK)

National Institute for Health and Care Excellence (NICE)

Nerve growth factor (NGF)

Nitric oxide (NO)

Nonlinear Chebyshev approximation method (NCAM)

Numerically Controlled Oscillator (NCO)

Osteoarthritis (OA)

Paraformaldehyde (PFA)

Particle Swarm Optimization (PSO)

Phase-locked loop (PLL)

Phosphate-buffered saline (PBS)

Point of care (POC)

Polydimethylsiloxane (PDMS)

Polyethylene glycol (PEG)

Polyvinyl alcohol (PVA)

Posterior cruciate ligament (PCL)

Principal component (PC)

Principal component analysis (PCA)

Printed circuit board (PCB)

Process, voltage, temperature (PVT)

Programmable-gain amplifiers (PGA)

Protein kinase B (PKB)

Pulse repetition frequency (PRF)

Reactive Ion Etching (RIE)

Root mean square (RMS)

Schwann cell (SC)

Signal-to-noise ratio (SNR)

Significant frequency sampling point (SFSP)

Single-pole double-throw (SPDT)

Spatial average temporal average (SATA)

Spurious-free dynamic range (SFDR)

Standard errors of the mean (SEM)

Successive approximation register (SAR)

Support vector machine (SVM)

Time-frequency domain swapping (TFDS)

Transimpedance amplifier (TIA)

Transcutaneous electrical nerve stimulation (TENS)

Tris-buffered saline (TBS)

Total knee arthroplasty (TKA)

Ultrasound fundamental frequency (UFF)

Water-soluble tetrazolium (WST)

World Health Organization (WHO)

1. Introduction

1.1 Background of Portable and Wearable Medical Devices

In recent years, there has been a surge in the popularity of portable and wearable healthcare devices owing to their diverse medical applications such as biomarker detection, pre-diagnostic analysis, and therapeutics [1, 2]. These devices are not only compact but also capable of real-time monitoring, which makes them very efficient and precise especially when used in point-of-care (POC) settings [3]. In contrast with conventional costly medical instruments priced over 10K USD, which require trained personnel to operate and have bulky sizes, these affordable easy-to-use alternatives can provide rapid results. Moreover, traditional medical instruments often involve the delivery of biosamples obtained from patients to stationary equipment, which is time-consuming. In contrast, portable and wearable healthcare systems can deliver rapid on-the-spot results while requiring fewer medical supplies. This significantly reduces patient waiting times and costs. With the potential to transform the field of healthcare by providing better patient care at lower costs, the use of portable and wearable systems is becoming increasingly popular among researchers and companies in the healthcare sector worldwide [4, 5].

Portable and wearable healthcare devices have become popular for their ability to detect biomarkers in biosamples like blood, urine, and human secretions. For instance, handheld blood glucose monitors enable diabetes patients to measure their glucose levels anytime, anywhere, [6]. This provides them with information that can help them to better manage their blood glucose condition, and it also allows patients to respond promptly to abnormal glucose levels. In addition, researchers have also been making efforts to develop POC biomarker detection methods for various cancers [7], such as prostate cancer [8], liver cancer [9], ovarian cancer [10], colorectal cancer [11], breast cancer [12], lung cancer [13], bladder cancer [14], and others.

These POC tumor biomarker detection solutions make early detection possible leading to improvement in survival rates. On the other hand, these technologies also offer promising applications in digital biomarker detection. This includes commercially available electrocardiogram (ECG) monitors providing high accuracy continuous monitoring while recording data or even sending it in real-time helping doctors monitor heart disease management effectively [15, 16]. Moreover, wearable devices, such as smart bracelets and watches, can track a patient's health condition, including heart rate, sleep quality, exercise intensity, and more [17, 18]. A famous example is the Apple Watch. Compared to conventional medical equipment, these portable and wearable healthcare devices assist in the timely collection and analysis of the physiological data of patients for personalized treatment decisions.

Regarding treatment, the utilization of portable and wearable medical devices can provide comprehensive healthcare services to patients by delivering drugs, physical therapy sessions, and other functions. For instance, individuals with diabetes can benefit from using wearable insulin pumps that help control blood sugar levels anytime, anywhere [19]. The use of electroceuticals in wearables or implants for therapeutic electrostimulation provides efficient delivery of electrical signals to targets such as nerve modulation or muscle activation while offering comfortable attachment [20]. Additionally, knee rehabilitation progress visualization is possible by using a sensor system worn on the body which facilitates at-home physical therapy programs [21].

In conclusion, portable and wearable medical devices have become an innovative area in healthcare development for their capabilities of providing continuous monitoring capabilities supporting remote care options along with personalized health management solutions. Also, this topic presents new opportunities for innovation within the healthcare industry increasing its growth potential and leading towards enhanced patient quality-of-life experiences. With further

advancements in technology and research, we can anticipate that these devices will continue to make increasingly important contributions toward human health advancement.

1.2 Bioimpedance

Bioimpedance is a non-invasive and cost-effective detection technique utilized in the biomedical research field that measures the electrical properties of biological tissues. Current research has been focused on improving the accuracy and reliability in bioimpedance measurements, particularly for complex biological systems. This focus is reflected in various aspects of bioimpedance measurement system development such as impedance tomography, microelectrode arrays, and wearable sensors [22-24]. Over the years, bioimpedance technology has found widespread application across several domains including medical diagnosis, health monitoring, food quality control, and others [25].

The fundamental principle of the bioimpedance technique is that different tissue types possess different electrical properties resulting from their unique composition and organization [26]. The impedance of biological tissue is expressed using a complex value— the real part resistance (R) and the imaginary part reactance (X_c). Resistance represents the opposition of a material to electric current flow, whereas reactance reflects its capacitive and inductive attributes [27]. To measure a tissue's impedance, a known alternating current (AC) signal is applied as an excitation signal, and the voltage across the sample is subsequently recorded, or vice versa. The bioimpedance measurement at various frequencies enables the differentiation between resistive and capacitive properties, thus offering more comprehensive insight into the tissue's electrical characteristics [28].

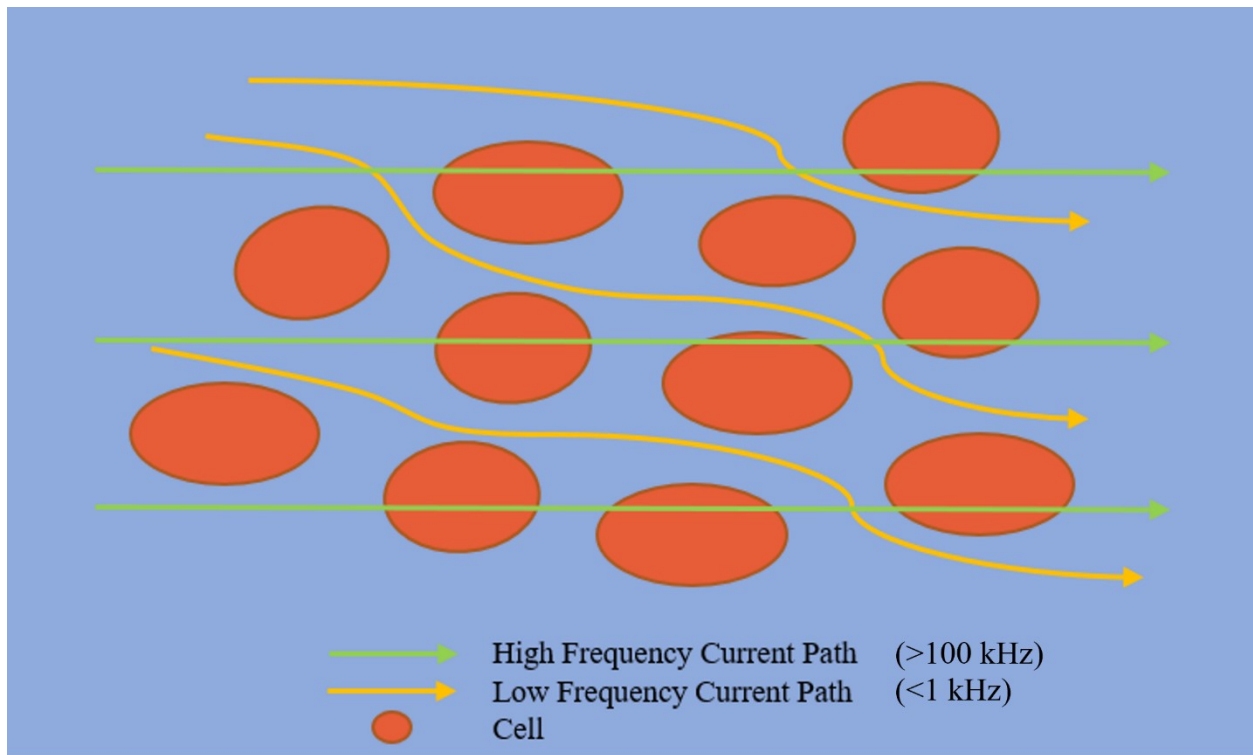


Figure 1.1 Demonstration of the relationship between the current through biological tissue and the frequency.

Bioimpedance measurements provide valuable insights into the properties of biological tissue [29-32]. The measurements involve electric currents at different frequencies, which behave differently within biological tissues as depicted in Figure 1.1. In the low-frequency range (typically below 1 kHz), the capacitive properties of cell membranes prevent electric current from penetrating them, hence it primarily flows through extracellular fluids. Therefore, bioimpedance readings obtained in this frequency range mainly reflect characteristics associated with the extracellular matrix and interstitial fluid, giving insight into their composition and structure. Conversely, high-frequency bioimpedance measurements (usually above 100 kHz) allow for an assessment of both intracellular and extracellular compartments since cell membranes no longer pose a barrier to electrical current flow; thus offering a more comprehensive measurement of overall tissue composition, structure, and function including

cellular components along with the intracellular fluids (ICF) within them. Researchers can obtain essential information about various aspects of biological tissues by measuring bioimpedance across a spectrum of frequencies. This method is called bioimpedance spectroscopy. This method is versatile for characterizing complex biological materials in different fields like healthcare, fitness, or agriculture due to its broad range of applications [28, 30, 33, 34].

To date, there have been numerous studies showing bioimpedance as a promising medical diagnostic tool. One of the most studied areas is the skin cancer diagnosis. For example, the research conducted by D. Kamat *et al.* exhibits that bioimpedance owns the potential in distinguishing between malignant and benign skin lesions [35]. Furthermore, P. Aberg *et al.* also demonstrated its potential capability to differentiate various types of skin cancers, including melanoma, squamous cell carcinoma, and basal cell carcinoma [36]. In addition to diagnosing skin diseases, researchers have also utilized bioimpedance measurements as a diagnostic technique for chronic obstructive pulmonary disease (COPD) diagnosis. Researchers evaluated the bioimpedance of the lungs in patients with COPD and found a statistically significant difference among different stages of the disease [37, 38]. Bioimpedance has also been studied in assessing other respiratory illnesses like pneumonia [39]. These findings suggest promising possibilities for non-invasive diagnostic tools employing bioimpedance analysis across many health concerns.

Apart from its diagnostic applications, bioimpedance has also been explored as a promising technique for health monitoring. For instance, it has been investigated in predicting the risk of heart failure progression by measuring the bioimpedance of patients with cardiovascular conditions [40-43]. Additionally, it can be utilized to measure body hydration levels [44-46]. This is especially useful for athletes who require fluid balance to enhance

performance [47]. Monitoring changes in body fat percentage is another application where bioimpedance can provide valuable information especially when tracking the progress of weight loss programs [48-50]. Furthermore, studies have shown that utilizing bioimpedance measurements could potentially enable healthcare professionals to track nutritional status accurately [51]. For instance, they may identify individuals at risk of malnutrition while undergoing chemotherapy treatment [52].

Bioimpedance technology has also demonstrated its potential in the food industry for assessing the quality control of various food products. For instance, it has been utilized to measure the electrical properties of meat products to indicate their freshness and overall quality [53]. Tomislav Ćurić *et al.* measured the bioimpedance of fish and found that it was able to predict the freshness of the fish based on salt and moisture content determination reflected by the bioimpedance [54]. Food water content measurement using this technique can be advantageous for classification purposes as well as ensuring high-quality food standards [55, 56]. Furthermore, Pietro Ibba *et al.* confirmed the utility of bioimpedance in monitoring aging evolution across a diverse range of fruits [57]. Regarding vegetable oils, Tjaša Prevc *et al.* proposed a system that utilizes electrodes immersed within vegetable oil samples which could classify edible oil's qualities due to the inherent higher insulating characteristics within the better vegetable oil [58]. F.J. Ferrero *et al.* developed an electronic detection tool designed specifically for early mastitis diagnosis for cows via analyzing milk conductivity during milking operations [59]. The versatility and potential applications of bioimpedance technology in various food quality controls make it a promising solution for further research and development.

In summary, bioimpedance is a versatile and non-invasive method that measures the electrical properties of biological tissues, with numerous applications in fields such as medical

diagnosis, health monitoring, and food quality control. The progress made over recent decades has seen significant advancements in mechanisms, techniques, and application areas. The current research state of bioimpedance indicates that it still holds great potential for advancing our understanding of various biological systems, resulting in more biomedical outcomes. However, there are still challenges, such as enhancing the accuracy and reliability of measurements, establishing appropriate models for various subjects, and the development of more portable user-friendly devices.

1.3 Low-intensity Pulsed Ultrasound

Ultrasound technology has been utilized for nearly a century in various medical applications such as diagnosis, therapy, and surgery [60, 61]. Initially, it focused on high-intensity ultrasound to utilize its thermal effects to elevate the temperature of the targeted tissue. This method paved the way for numerous medical procedures and interventions [60, 61]. In recent years, however, there has been an increasing interest in low-intensity ultrasound which does not rely on thermal effects. This emerging field of research has potential versatility in medicine. Promising progress has been reported for many applications including bone fracture healing promotion [62], neuromodulation [63], peripheral nerve regeneration [64], cancer therapy [65, 66], and so on.

Low-intensity pulsed ultrasound (LIPUS), a derivation of low-intensity ultrasound, is an innovative non-invasive therapeutic method gathering attention across biomedical research domains due largely in part due to its demonstrated potential to promote tissue repair and regeneration. As illustrated in Figure 1.2, LIPUS has pulses of ultrasound waves and comes with three timing parameters including pulse repetition frequency (PRF), ultrasound fundamental frequency (UFF), and duty cycles. The amount of delivered energy is determined by these

parameters alongside ultrasound amplitude to ensure that a therapeutic effect is achieved without thermal issues. The unique characteristic of LIPUS is its capability of providing sufficient ultrasound amplitude without causing thermal problems as it concentrates energy within pulses, instead of providing continuous delivery [67].

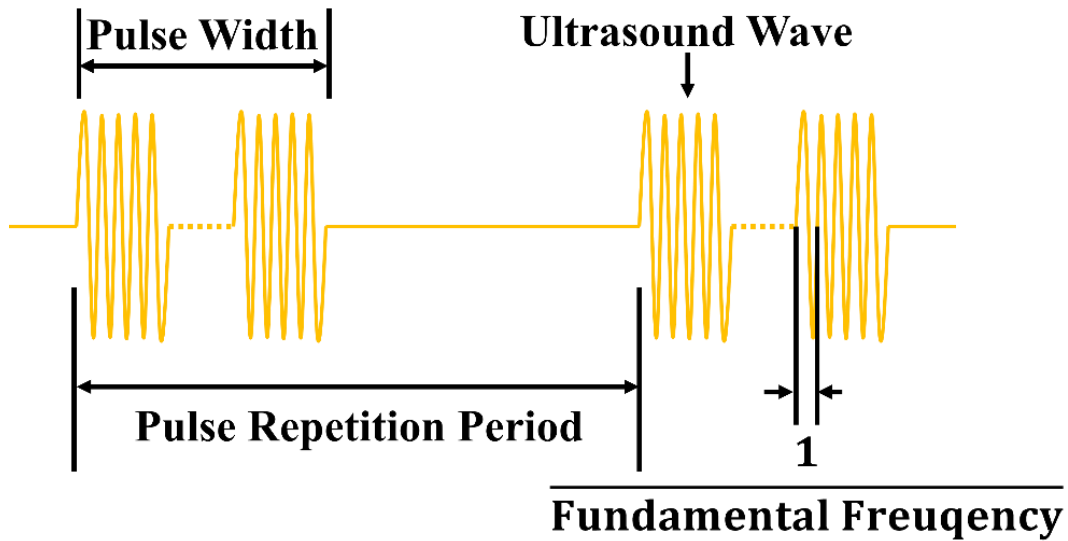


Figure 1.2 Demonstration of a LIPUS wave and its essential parameters.

The complete comprehension of the therapeutic efficacy mechanism for LIPUS in medical applications remains to be studied extensively [63]. Nevertheless, several hypothetical mechanisms have been proposed, including mechanical stimulation, cavitation, and Nitric oxide (NO) production. (a) mechanical stimulation: Pressure waves generated by LIPUS result in mechanical stress on cells and tissues. Consequently, mechanotransduction pathways are activated upon conversion of these signals into biochemical responses causing an increase in growth factors' secretion alongside cytokines and extracellular matrix proteins' production crucial for tissue repair or regeneration [68-72]. (b) cavitation: LIPUS can cause the formation and collapse of microscopic gas bubbles within biological tissues, a phenomenon known as

cavitation. The rapid collapse of these bubbles generates localized mechanical stress, which increases cell membrane permeability. This phenomenon facilitates the transport of essential biomolecules, including growth factors and nutrients, into and out of cells, thereby promoting healing and regeneration [73-79]. (c) NO production: LIPUS has also been demonstrated to stimulate the production of NO, a gaseous signaling molecule that participates in numerous physiological processes. NO possesses vasodilatory properties, which can enhance blood flow and oxygen delivery to damaged tissues. Moreover, NO contributes to angiogenesis, inflammation modulation, and tissue repair, thereby augmenting the therapeutic effects of LIPUS [80-84].

LIPUS has been gaining attention for its various clinical applications, primarily due to its ability to stimulate tissue regeneration and healing. First, LIPUS has demonstrated the potential in accelerating bone healing in instances of fractures and non-union fractures [79]. LIPUS may significantly expedite the overall process by promoting new bone formation, increasing bone mineral density, and shortening consolidation duration [85-87]. The first LIPUS device for promoting fresh fracture healing received approval from the U.S. Food and Drug Administration (FDA) in 1994 [88, 89]. Subsequently, in 2000, the FDA approved the use of LIPUS in nonunion treatment [90, 91]. These can be valuable options particularly beneficial for patients experiencing delayed or impeded fracture healing.

Second, the effectiveness of LIPUS in enhancing tendon and ligament healing has been extensively investigated. Through promoting cellular proliferation, collagen synthesis, and growth factor expression, LIPUS therapy presents an alternative therapeutic option for soft tissue disorders, like tendinopathies or ligament injuries, as it aids with repairing and regenerating the injured tissues [92, 93]. As early as 1990, Enwemeka *et al.* investigated the effects of low-

intensity ultrasound on the human tendon calcaneus healing process; their study concluded that low-intensity sonication yields superior results than high-intensity ones [94]. Similarly, a research investigation by Hsu *et al.* revealed that LIPUS therapy significantly improved clinical outcomes and structural healing in patients with Achilles tendinopathy [95]. Animal studies undertaken by Takakura *et al.* also suggested early recovery potential post-medial collateral ligament injury upon using LIPUS therapy, which highlights its value as a promising therapeutic intervention [96]. These findings support the use of LIPUS for treating various types of tendon or ligament injuries to assist established treatments.

Third, the utilization of LIPUS has also shown promise in inflammation treatment [97]. The study conducted by Binder *et al.* demonstrated the therapeutic effects of LIPUS on epicondylitis, presenting improved weight-lifting capacity, grip strength, and relief from pain for subjects in LIPUS-treated groups [98]. Harris *et al.* subsequently investigated the anti-inflammatory benefits provided by LIPUS with evaluations of facial swelling, trismus, pain, and serum C-reactive protein outcomes [99, 100]. They were the first to observe that lower-intensity ultrasound yielded greater benefits than higher intensities. From 2012 to 2013, Engelmann *et al.* and Nagata *et al.* skeletal muscle injury treatment using LIPUS combined with gel dimethylsulfoxide (DMSO) [101, 102]. Their findings revealed that pro-inflammatory cytokines (TNF α , IL-1 β , phosphor JNK, and NF κ B) were inhibited effectively with the treatment, which had been elevated due to muscle injury. In addition, Nakamura *et al.* and Chung *et al.* studied its potential application in treating synovitis-associated inflammatory activity, with the results indicating a significant decline rate regarding cellular proliferation with LIPUS [103, 104]. These studies also demonstrated a decrease in cell growth and DNA fragmentation levels (an apoptosis indicator) in synovial membrane cells stimulated by cytokines TNF α , IL-1 β , iNOS, and

chemokine receptor CCR5. Skepticism persisted for a long time regarding the efficacy of LIPUS in inflammation inhibition, and many researchers suspected that it merely functioned as a placebo. However, accumulating evidence has dispelled this doubt, and LIPUS now holds considerable promise for inhibiting inflammation in various medical applications.

Fourth, some studies indicate that LIPUS has shown promise in facilitating nerve regeneration and treating nerve injuries [105, 106]. Recently, Haffey *et al.* conducted a systematic review, highlighting the potential of LIPUS in nerve regeneration and carpal tunnel syndrome treatment [107]. As early as 2002, Crisci AR *et al.* found that LIPUS promoted rapid nerve regeneration after neurotomy by improving Schwann cell (SC) activity, generating thick fibers, and accelerating myelin sheath recovery [108]. In 2011, Tsuang *et al.* observed that LIPUS facilitated primary cultured SC proliferation and prevents cell death, even in severe injuries [109]. Yue *et al.* demonstrated that adipose-derived stem cell coculture increased promyelination markers in SCs, with effects amplified by LIPUS, suggesting its potential as a mechanical stress inducer in nerve regeneration [110]. Sato *et al.* explored the impact of daily LIPUS exposure on transected inferior alveolar nerves in rats, suggesting LIPUS as an effective therapy for such injuries [111]. Then, Jiang *et al.* investigated the influence of different LIPUS intensities on autograft peripheral nerve regeneration in rats and identified an optimal intensity for improved outcomes [112]. Although most studies are preclinical, they presented promising outcomes that have the potential to be extrapolated into human studies. Therefore, LIPUS is a promising treatment option for nerve injuries, but it needs further research to optimize parameters and protocols.

Last but not least, LIPUS has also demonstrated potential in cancer therapy as an adjunctive treatment modality [65]. It assists cancer therapy by augmenting drug delivery,

facilitating sonodynamic therapy, modulating gene transfection, and integrating with other therapeutic modalities [65]. Sonodynamic therapy that utilizes ultrasound-induced cavitation and sonosensitizers for generating free radicals destroying rapidly dividing cancer cells is a promising approach to treating tumor growth [113]. Jin *et al.* found a substantial inhibition of 77% in the squamous cell carcinoma's murine model by using LIPUS [114]. In addition, LIPUS has also been explored for enhancing chemotherapeutic agent delivery [115]. Yu *et al.* observed ultrasound suppressing cell proliferation in chemoresistant human ovarian cancer cells with chemosensitive cells that remained unaffected [116]. Furthermore, Li *et al.* (2013) reported inhibited tumor growth, angiogenesis, and lymphangiogenesis in human tongue squamous cell carcinoma when combining scutellarin oral administration and LIPUS treatment [117]. More recently studies focused on linking LIPUS and microbubbles, and it has been applied to assist gene delivery to neoplastic cells. The underlying idea behind this is that the controlled destruction of DNA-loaded microbubble targets in the tumor vasculature with focused ultrasound generates the local release of genetic materials into the tumor parenchyma [118-121]. These studies suggest that LIPUS has the potential to optimize therapeutic outcomes, mitigate adverse effects, and amplify the efficacy of established cancer treatments. Nevertheless, further human studies and clinical trials are required to comprehensively understand its prospective role and improve its implementation in cancer therapy.

Over the past few years, significant advancements have been taken in LIPUS research. Many studies underscored its capacity as a non-invasive therapeutic modality for tissue rejuvenation and healing. Nevertheless, realizing its clinical potential still encounters obstacles such as the lack of standardized treatment protocols and inadequate comprehension of underlying mechanisms. Therefore, future research should prioritize addressing these challenges while also

exploring how combining LIPUS with alternative therapies can maximize promising therapeutic effects through synergetic effects.

1.4 Contribution and Novelty of This Thesis

The dissertation primarily contributes to the field of biomedical engineering by advancing the development and application of portable, cost-effective, and wearable technologies for biomarker detection, diagnosis, and treatment.

First, in the study on knee injury bioimpedance measurements, the dissertation presents a novel and cost-effective technique that demonstrates promise for the early detection and ongoing monitoring of knee injuries. This work not only validated the feasibility of using a bipolar electrode configuration for such measurements, but also developed a highly sensitive classification model for identifying injured knees based on bioimpedance data.

Second, the electrochemical impedance spectroscopy (EIS) -based POC biomarker detection study is introduced as a rapid method to detect anti-SARS-CoV-2 IgG in serum samples. The results showed a clear distinction between negative and positive samples, presenting a statistical significance with a p-value of 7×10^{-6} . Its adaptability for detecting other biomarkers makes it a versatile and powerful tool for the development of efficient diagnostic tools for a wide range of diseases and health conditions.

Third, in developing a portable, low-cost EIS system for POC testing, the dissertation provides a highly precise and efficient biosensor platform with excellent measurement speed and accuracy. This system supports simultaneous EIS across eight channels and adopts bio-safe low excitation amplitude, making it a valuable contribution to the field of POC diagnostics.

Fourth, the dissertation presents a LIPUS interface application-specific integrated circuit (ASIC) chip for miniaturized medical therapeutic device applications. The highly integrated LIPUS system, which is compatible with magnetic resonance imaging (MRI) environments, has numerous potential applications in various therapeutic scenarios and offers a competitive advantage over existing commercial devices due to its compact and affordable design.

Lastly, the *in vitro* study investigated LIPUS for neural cell growth promotion and nervous system regeneration. It provides valuable insights into the potential therapeutic effects of LIPUS for promoting neuronal growth. The study examined the BDNF, ERK, Akt, and mTOR signaling pathways in response to LIPUS treatment. The outcome also emphasizes the importance of optimizing LIPUS timing and amplitude parameters.

In summary, this dissertation represents a significant achievement in the advancement and practical implementation of portable, wearable, and low-cost biomedical devices. Through exploring novel techniques for biomarker detection, diagnosis, and treatment of diverse medical conditions, these studies present contributions to the scientific community. The findings also pave a pathway for future research and development in this area.

1.5 Thesis Outline

This dissertation is structured into seven chapters, comprehensively presenting my research progress in the fields of bioimpedance and LIPUS. Chapter 1 provides an overview of the background and current research advancements related to bioimpedance and LIPUS. Chapter 2 explores the feasibility of using a bipolar electrode configuration for knee bioimpedance measurements and investigates the relationship between bioimpedance and knee injuries. Chapter 3 introduces an EIS-based method for detecting the anti-SARS-CoV-2 IgG antibody in

serum samples utilizing interdigitated micro-electrode (IDE) biosensors. Chapter 4 presents a portable, low-cost EIS system specifically designed for POC applications, showcasing exceptional accuracy and precision in biosample measurements. Chapter 5 introduces a LIPUS interface ASIC chip, specifically engineered for portable medical therapy devices. Chapter 6 examines the effects of LIPUS treatment on SK-N-SH cells cultured in low-serum conditions and analyzes the influence of various LIPUS parameters on cellular response. Lastly, Chapter 7 summarizes the aforementioned research findings and outlines potential directions for future work.

2. Bioimpedance Measurement of Knee Injuries using Bipolar Electrode Configuration

The content of this chapter has been published in IEEE Transactions on Biomedical Circuits and Systems 16, no. 5 (2022): 962-971 as "Bioimpedance measurement of knee injuries using bipolar electrode configuration" by Xuanjie Ye, Lexi Wu, Kaining Mao, Yiwei Feng, Jiajun Li, Lei Ning, and Jie Chen.

2.1 Introduction

2.1.1 Knee Injury Diagnosis Methods

Knee injuries, including osteoarthritis (OA), ligament disruptions, and meniscal damage, are the leading cause of clinical consultations [122-124]. The prevalence of OA is particularly high in individuals aged 60 years and above with around 10% experiencing this condition worldwide according to WHO scientific groups [125, 126]. As life expectancy continues to increase globally, there is an anticipated rise in the occurrence of OA cases during subsequent years [126, 127]. Physical activities like vigorous exercise have been associated with knee injuries that commonly lead to injuries like ligament disruptions or meniscal damage which has reached unprecedented levels due to more people integrating these activities into their daily routines [122-124].

Diagnostic imaging remains the primary approach for diagnosing knee disorders presently because of its comprehensive assessment capabilities on structures within the joint area. MRI stands out amongst other diagnostic methods utilized by clinicians because it boasts an accuracy rate exceeding over 90% based on various studies conducted thus far [128]. Additional diagnostic methods commonly utilized in clinical practice include X-ray and

ultrasound scans [129, 130]. While these imaging-based techniques provide accurate information about knee conditions, they demand costly and bulky medical instruments as well as skilled technicians. In certain clinical practices, knee injury diagnosis may merely involve inquiries about a patients' physical constraints and impairments [131-133]. This subjective approach, however, lacks reliability due to its inability to evaluate physiological or pathological alterations in the knee joints [134]. Furthermore, current diagnostic methods for knee injuries cannot be easily expanded to the applications such as long-term rehabilitation tracking or early detection. Therefore, the development of a rapid, noninvasive, and accessible diagnostic tool for knee disorders is urgent and necessary.

2.1.2 Fundamentals of Knee Injury Diagnosis Based on Bioimpedance

Bioimpedance measurement is a promising and emerging medical technology, which offers non-invasive data acquisition of biological tissues using low-cost and portable devices. The current hypothesis suggests that physiological and pathological changes occurring during knee disorders may result in a decrease in bioimpedance. Synovial fluid, a small volume of extracellular fluid (ECF) with an egg-white-like consistency, is present in healthy knee joints and serves to reduce friction between the articular cartilage during joint movement [135]. However, the accumulation of synovial fluid may occur in cases of knee disorders, probably leading to synovitis [136]. From a view of bioimpedance, synovial fluid, as a type of ECF, exhibits higher conductivity compared to other tissues in the knee joint [137]. When synovial fluid accumulates and disperses throughout the knee joint cavity, its bioimpedance decreases due to a "short-circuit" effect. Furthermore, disruptions or cartilage damage may also reduce their resistance to electrical current. Consequently, the bioimpedance of an injured knee is expected to be lower than that of a healthy knee.

The knee joint is recognized as the most complex joint in the human body, as depicted in Figure 2.1. Its osseous components display a complex anatomical structure that consists of four distinct bones: femur, tibia, fibula, and patella. The two distal ends of the femur—commonly referred to as lateral and medial condyles—correspond with morphology on top of the tibial plateau forming this way an elaborate articular surface for weight-bearing purposes. Shock absorption within such movement relies upon menisci which are semicircular-shaped structures located between these bone surfaces [138]. Positioned anteriorly from this point where both aforementioned bones converge lies another crucial bone tissue called the patella; known by its function representing our largest sesamoid (a small round bone embedded inside tendons). The knee joint has four primary ligaments that connect the femur to the tibia, and the function to maintain knee stability. The anterior cruciate ligament (ACL) prevents excessive anterior displacement of the tibia relative to the femur. By contrast, the posterior cruciate ligament (PCL) restricts the femur from sliding over forward on the tibia. Similarly, the medial collateral ligament (MCL) and lateral collateral ligament (LCL) function to prevent abnormal lateral and medial movements between the femur and tibia [139, 140].

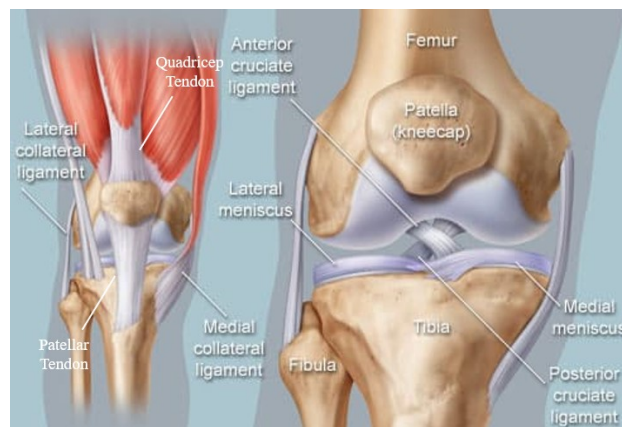


Figure 2.1 The anatomy of a right knee (Figure source: <https://www.webmd.com/pain-management/knee-pain/picture-of-the-knee>)

Bursae are small sacs filled with fluid that play a crucial role in reducing friction between bones and soft tissues. They contribute to the smooth movement of knee joints by enabling tendons and muscles to slide freely. The human knee joint contains multiple bursae, as shown in Figure 2.2(a). Apart from bursae, the synovial membrane generates synovial fluid which lubricates the knee joint while also facilitating nutrient circulation within it; an average healthy individual's knees contain around 5 mL of this essential liquid [141, 142]. As shown in Figure 2.2(b), the knee joint is enveloped by the synovial membrane—the largest synovial membrane in the human body.

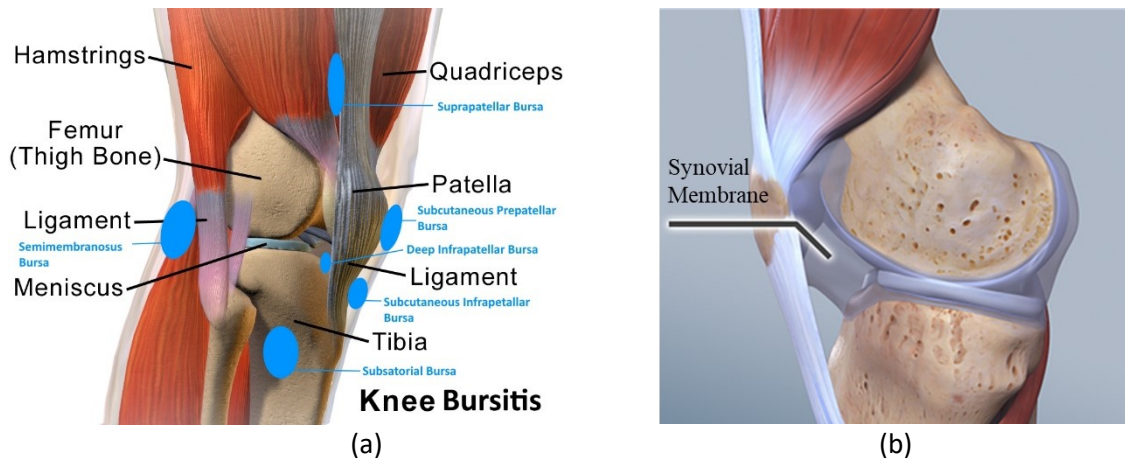


Figure 2.2 (a) the locations of the bursae around the knee joint (source: <https://www.midliferunning.com/knee-bursitis.html>) (b) the synovial membrane of the knee joint (source: <https://www.arthritis-health.com/types/joint-anatomy/knee-anatomy>).

Table I displays dielectric property information about various components present inside the knee joint. The ECF has been found out having the highest conductivity among all these entities. The ECF refers here to fluids outside cells like blood plasma, cerebrospinal fluid, etc., that have different conductivities ranging across their constituent types: for instance, blood

shows a conductivity of 0.7 S/m [143], while cerebrospinal fluid has a conductivity of 1.56 S/m [144]. The exact value concerning the conductivity of synovial fluid remains unknown but is expected to be alike other ECFs. Furthermore, cancellous bone exhibits roughly four times more significant electrical conductivity than cortical bone because porous structures may provide increased pathways current may follow through them. By contrast, fat and cortical osseous tissue show much lower electrical conductivity compared to other tissues in the knee joints.

Table I Dielectric properties of the components at 100 kHz [137, 143-145]

Component	Conductivity (S/m)	Relative Permittivity
Extracellular Fluid (Blood)	0.7	5000
Extracellular Fluid (cerebrospinal fluid)	1.56	1000
Bone (Cancellous)	0.09	600
Bone (Cortical)	0.02	210
Fat	0.04	150
Muscle	0.4	10000
Skin (Dry)	0.0004	1000
Skin(Wet)	0.04	20000
Tendon	0.4	800
Cartilage	0.18	6000

Among fractures in the knee region, patellar fractures are the most prevalent, followed by the distal femur and proximal tibia fractures [146]. Similar to the conductivity difference between cancellous and cortical bones, fractured bones likely present fewer obstacles to electrical current. The presence of cracks in a fractured bone might provide additional current pathways, which presents as reduced bioimpedance. One clinical manifestation of knee joint fractures is swelling, resulting from blood leakage from the fractured bones into the joint [147, 148]. The spread of blood within the joint space has a short-circuit effect on adjacent tissues, consequently decreasing the bioimpedance.

Acute knee injuries, such as sprains and tears of the menisci, ligaments, and tendons, usually result in rapid swelling within 24 to 48 hours [149]. This kind of effusion can be either bloody or non-bloody. Bloody effusion is often associated with ligament tears or cartilage fractures [150], and such swelling potentially occurs within hours. A prospective study involving 106 acute hemarthrosis cases revealed that patients diagnosed with acute knee injuries, including ligament disruptions, meniscal tears, and osteochondral fractures, would experience swelling within 12 hours of injury [151]. Non-bloody fluid, typically caused by ligament sprains or meniscal tears, exhibits a slower progression than bloody fluid and may be observed hours or even days after the injury. Furthermore, acute knee injuries can trigger synovial inflammation, leading to the accumulation of synovial fluid [152]. Both bloody and non-bloody fluids display higher conductivity than osseous tissues and soft tissues in the knee joint.

In chronic knee injuries, such as OA and rheumatoid arthritis, the degree of swelling varies with different symptoms. The inflammation associated with OA can generate excess fluid within the knee joint [153], with fluid volume positively correlating to symptom severity [142]. Heilmann *et al.* found significant differences in synovial fluid volume between human knee joints with latent OA, activated OA, and a control group; knee joints with latent OA exhibited a synovial fluid volume of 13.6 ± 7.4 ml, while those with activated OA had a volume of 24.2 ± 16.3 ml [141]. As an autoimmune disorder, rheumatoid arthritis can lead to persistent swelling due to ongoing inflammation [154]. Additionally, septic arthritis arises from bacterial, viral, or fungal infections within the knee joint, with the ensuing inflammatory response also resulting in fluid accumulation [155].

Some studies investigated the effect of knee swelling on bioimpedance following total knee arthroplasty (TKA). In 2015, Yong-Hua Pua *et al.* analyzed bioimpedance spectroscopy

(BIS) data obtained from 85 patients before surgery and on days 14 and 90 post-surgery, and results indicated that the bioimpedance of the TKA knee decreased during swelling development and increased during recovery [156]. In the same year, Claude Pichonnaz *et al.* compared the percentage difference of bioimpedance between healthy knees and those that underwent TKA to track swelling changes. As swelling developed after the surgery, the bioimpedance of the TKA knee significantly decreased. They also found that BIS exhibited better sensitivity (100%) and specificity (96%) for diagnosing swelling than volume or circumference measurements [157]. Additionally, Pichonnaz *et al.* assessed the bioimpedance of knees recovering from TKA using bioelectrical impedance analysis (BIA). The research included 15 patients who had undergone TKA surgery at least one year before the bioimpedance evaluation. The study found no significant differences between the recovered TKA group and the healthy control group. This result implied that metallic implants did not affect knee bioimpedance, which would return to normal levels after recovery [158].

2.1.3 Current Research Status of Knee Injury Diagnosis Based on Bioimpedance

Numerous research groups have tried to study the relationship between knee bioimpedance and injuries, as well as develop innovative wearable devices for the early detection and monitoring of knee injuries. Two notable studies in this field are those conducted by Neves *et al.* [134] and Hersek *et al.* [159].



Figure 2.3 (a) Electrode placement in Neves’s study [134]. (b) Electrode placement in Hersek’s study [159].

Neves *et al.* investigated the differences in knee bioimpedances between healthy individuals and subjects diagnosed with OA [134]. The major outcome they discovered is that extracellular resistance and reactance of the knees would increase as a consequence of OA. They employed a bipolar electrode configuration to obtain localized bioimpedance measurements. The electrodes were placed on the lateral and medial sides of the knee's interarticular line, as demonstrated in Figure 2.3(a). During the bioimpedance measurement process, a 500-mV step voltage was applied to the subjects' knees, and its current response was recorded. This current response data was then used to fit a seven-component equivalent circuit model, which consists of two resistors and one capacitor that represented the resistance of ECF, ICF, and the capacitance of the cellular membrane, respectively. The analysis indicated that OA-affected knees exhibited higher ECF resistance and greater cellular membrane capacitance in comparison to healthy knees ($p < 0.001$). However, the study has certain potential limitations. The impedance measurements based on step response are naturally unreliable compared to conventional methods [160]. Multiple parameter combinations fitting results may come with similar errors, and no algorithm

can search for the optimal fitting result. Furthermore, it lacks the validation for the proposed equivalent circuit model as an accurate representation of the knee.

In 2016, Hersek et al. developed a wearable vector electrical bioimpedance system specifically designed to assess knee joint health [159]. The system functioned by injecting a sinusoidal current (50 kHz, 1 mA) into the knee and measuring the voltage across it. The electrode placement for this system is illustrated in Figure 2.3(b). The study involved two groups of subjects: 7 patients who had recently experienced acute knee injuries and 42 healthy controls. This study revealed that injured knees could be distinguished from healthy knees based on their lower resistance and higher reactance values ($p < 0.05$). Furthermore, the wearable system demonstrated a 98.2% accuracy in detecting knee health when subjects maintained a specific posture during measurements. Their proposed wearable system holds significant promise for POC assessment and monitoring of knee joint health.

2.1.4 Contribution of This Study

The primary objective of this study was to validate the feasibility of utilizing bioimpedance measurements with a bipolar electrode configuration as a non-invasive technique for detecting knee injuries. The Xiyuan acupuncture point was selected due to its ease of identification, ensuring that individuals with minimal anatomical knowledge could locate it easily. Initially, experiments were conducted to assess the feasibility of the bipolar electrode configuration in obtaining accurate bioimpedance measurements of the knees. After that, 45 patients with knee injuries and 45 healthy individuals were then recruited to obtain bioimpedance data from their knees. This step was to explore the relationship between knee injuries and bioimpedance. Machine learning techniques such as Principal Component Analysis (PCA) and Support Vector Machine (SVM), together with IBM SPSS Statistics 25.0 software, were used in

analyzing the data [161, 162]. These analyses aimed at identifying potential correlations between bioimpedance levels and knee injury. After careful evaluation of the data, 76 valid samples were selected to investigate the relationship between bioimpedance and knee injuries. The sample included 39 patients with unilateral knee injuries and 37 healthy controls. The self-contrast results suggest that knee injuries led to an average reduction of approximately 5% in knee bioimpedance, which was detectable at 100 kHz ($p = 0.001$). Our study contributes to the research on bioimpedance-based technologies for knee injury detection and reveals the potential of bipolar electrode configuration.

2.2 Materials and Methods

2.2.1 Feasibility Study of the Bipolar Electrode Configuration

In this study, we positioned the electrodes on the two Xiyan points of each knee. The Xiyan points, found in traditional Chinese medical science, are referred to as the "eyes" of the knee in traditional Chinese culture. These points are located in the two hollows formed when the knee is bent, next to both the medial and lateral aspects of the patellar ligament and below the patella, as illustrated in Figure 2.4(a) [163]. There are no primary ligament or skeletal structures beneath the Xiyan points, ensuring that the injected current can easily traverse the knee joint cavity, where effusion most frequently occurs [164]. Moreover, the knee was required to flex at 90° during the bioimpedance measurement. With this posture, the knee joint cavity volume expands, potentially increasing the sensitivity of the injection current to changes within the joint cavity.

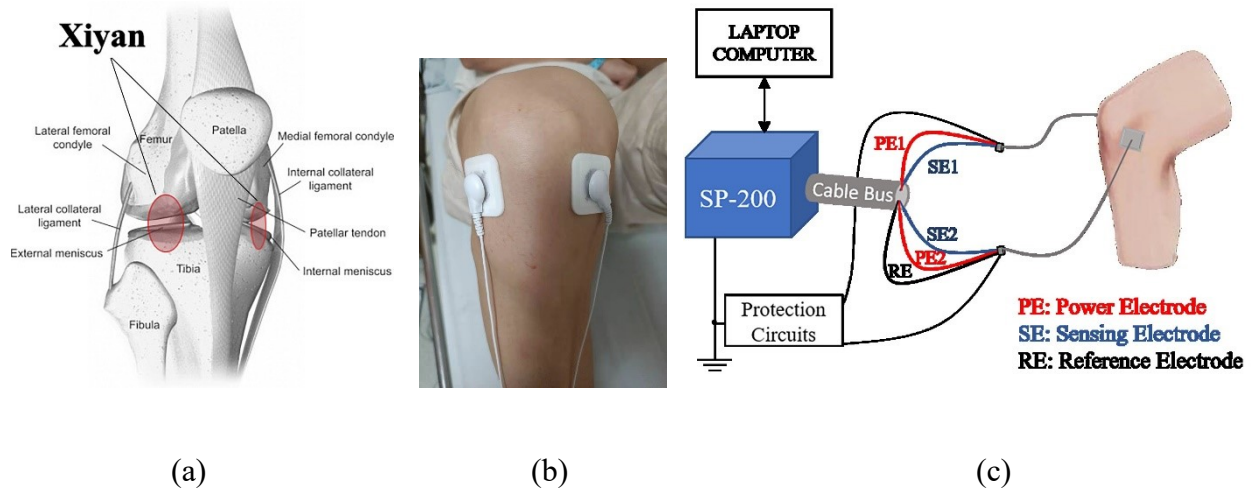


Figure 2.4 (a) Illustration of the positions of Xiyan (reproduced from [165]). (b) The placement of bipolar electrodes on Xiyan in a real test (reproduced from [166]). (c) Setup for the bioimpedance measurement (not to scale) (reproduced from [166]).

We selected the bipolar electrode configuration (two electrodes) over the tetrapolar electrode configuration (four electrodes) for knee bioimpedance measurements due to its simplicity and ability to minimize irrelevant signals when measuring bioimpedance in a small section of the human body [134]. Conversely, when the tetrapolar electrode configuration is improperly applied to an anatomically complex and spherical structure like the knee, it is difficult to determine which part contributes to the measured impedance values due to the negative sensitivity effect [167-169]. Additionally, the tetrapolar configuration is suitable for small impedance, since it typically requires the injection of a constant current into the objective. Our preliminary experiments indicated that the knee's bioimpedance could reach millions of ohms at 100 Hz. Even when injecting a 0.1 mA current at a low frequency, the required applied voltage could reach hundreds of volts, which is dangerous for human beings. Consequently, we employed the bipolar electrode configuration in our study.

However, the bipolar electrode configuration may be influenced by external factors, such as electrode-skin impedance, lead inductance, and parasitic capacitance. The primary external factor, electrode-skin impedance, varies depending on skin type, electrode gel, adhesion degree, and thermal noise [170, 171]. Additionally, the electrode-skin impedance is affected by the duration of sticking (DS), referring to how long electrodes have stuck on the skin [172]. Lead inductance and parasitic capacitance primarily depend on the geometric configuration of the lead, probe, and electrodes, which is extremely difficult to maintain consistency across all tests. Thus, it is important to examine the impact of these external factors to evaluate the feasibility of the bipolar electrode configuration.

We employed three volunteers with bilateral healthy knees to investigate the influence of external factors on bioimpedance measurement. During the measurement process, knees were flexed at 90° to expand the knee joint volume, and two disposable Ag/AgCl electrodes (model 2228 3M Inc., USA) were placed on the two Xiyan points of each knee, as depicted in Figure 2.4(b). The bioimpedance of both knees was measured once per day for four consecutive days. The bioimpedance of the knees was scanned from 100 Hz to 1 MHz using the SP-200 (Biologic Inc., France) at 1 min, 5 min, 15 min, 30 min, and 60 min DS. A 1.5 V peak-to-peak sinusoidal wave signal was applied as an excitation signal for less than 0.1 seconds at each frequency point, with an effective current below 0.1 mA, conforming to the IEC-60601-1 International Medical Alarm Standard [173]. The protection circuits ensured that the output voltage remained within a safe range for human subjects. The entire setup is displayed in Figure 2.4(c).

2.2.2 Bioimpedance Measurement of Knee Injuries

After confirming the potential feasibility of the bipolar electrode configuration for knee bioimpedance measurement, we moved on to investigate the impact of knee injuries on

bioimpedance measurements. This study, which received approval from the local ethical committee (approval No. 20210205-36), was conducted at the Sir Run Run Shaw Hospital, affiliated with the Medical College of Zhejiang University, China.

The study participants were recruited from visitors to the Sir Run Run Shaw Hospital and consisted of 45 healthy controls and 45 patients. The researchers confirmed the absence of knee injuries before including them in the healthy control group. In the patient group, each individual had a unilateral knee injury. The injured knees were diagnosed with one of the following conditions according to guidelines: ACL injury, PCL injury, OA, or menisci lesion [174, 175]. Exclusion criteria for the patient group included: 1) inflexible knee movement; 2) unsuitable skin conditions for electrode placement; and 3) noticeable swelling or deformity in the knees.

For each participant in both the patient and control groups, knee bioimpedance measurements were taken using the same setup as in the previous validation study, with measurements conducted at 5 minutes DS. This time point was chosen because the bioimpedance measurements were relatively stable at 5 minutes DS, and it was unlikely to cause skin irritation. The reasons for the “5 minutes DS” will be detailed in the following discussion. During the measurement process, all participants were asked to lie on beds, remaining still with their knees bent at a 90° angle. No discomfort was reported during the measurements.

$$\Delta_{Z_p} = \frac{Z_i - Z_h}{Z_h} \quad (2.1)$$

$$\Delta_{Z_h} = \frac{Z_l - Z_r}{Z_r} \quad (2.2)$$

Since body compositions and structures vary significantly among individuals, comparing the bioimpedance of both knees for the same individual provides more meaningful data.

Therefore, we calculated the relative differences in bioimpedance between the two knees of each subject to analyze the relationship between bioimpedance and injuries. The relative differences were expressed in Equations 2.1 and 2.2, where Δ_{Z_p} and Δ_{Z_h} are the relative differences in bioimpedance between the two knees of patients and healthy controls, and Z_i, Z_h, Z_l, Z_r are the bioimpedances measured from injured, healthy, left, and right knees, respectively. Based on the results from the previous feasibility validation study, a sample would be rejected if Δ_{Z_p} or Δ_{Z_h} was larger than 100% or smaller than -50% at 100 Hz or 1 MHz, indicating a significant difference in the influence of external factors between the two measurements. Consequently, the total valid sample comprised 39 patients and 37 healthy controls.

The differences in gender distribution between the patient and control groups were assessed using the Pearson Chi-square test. The Kolmogorov-Smirnov test was utilized to evaluate the differences in age, weight, height, and body mass index (BMI). In this study, the patient group was not further divided into subgroups based on knee symptoms because the aim is to establish a correlation between bioimpedance and knee injuries as a whole. IBM SPSS Statistics 25.0 software was used to conduct the t-test, which facilitated the comparison of Δ_{Z_p} and Δ_{Z_h} distributions. PCA and support vector machine SVM algorithms were implemented to classify the two groups. The classification outcomes were then assessed using the leave-one-out cross-validation (LOOCV) method.

2.3 Results

2.3.1 Feasibility Study of the Bipolar Electrode Configuration

The bioimpedance measurements taken at different DS intervals revealed that the decrease in the measured bioimpedance values became less significant after 5 mins DS. Figure

2.5 illustrates the reduction percentages of the measured bioimpedance across different DS segments. The reduction percentage is defined as the decrease in bioimpedance measured at a specific DS segment. For instance, the reduction percentage from x min DS to y mins DS is expressed using Equation 2.3, where Z_{xmins} and Z_{ymins} represent the bioimpedances measured at x mins and y mins DS, respectively. The measured bioimpedance decreased by approximately 5% to 10% on average from 1 min DS to 5 mins DS. In contrast, the reduction percentages in the remaining DS segments were within 5% for the frequency range from 46.4 kHz to 215 kHz, which exhibited near-zero reduction percentages with relatively small standard deviations. These results suggest that the measured bioimpedances are likely to be relatively stable when DS reaches 5 mins. Additionally, the bioimpedances measured at 464 kHz and 1 MHz appeared to be unrelated to the DS. The reduction percentages at 464 kHz and 1 MHz exhibited notably large standard deviations (20%) across all DS segments, while their averages fluctuated around zero.

$$ReductionPercentage_{x\sim ymins} = 100\% \times \frac{Z_{xmins} - Z_{ymins}}{Z_{xmins}} \quad (2.3)$$

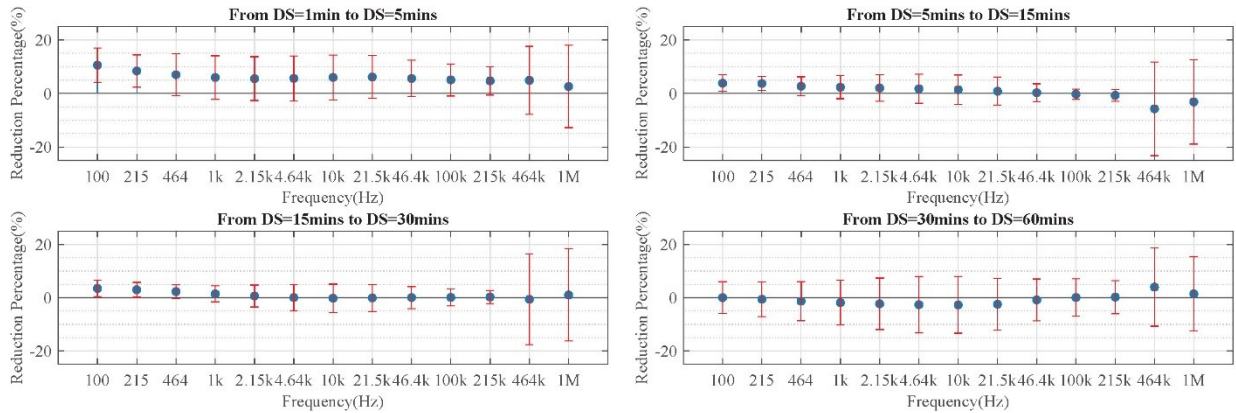


Figure 2.5 The mean and standard deviation of bioimpedance reduction percentages across various DS segments over a frequency range of 100 Hz to 1 MHz (reproduced from [166]).

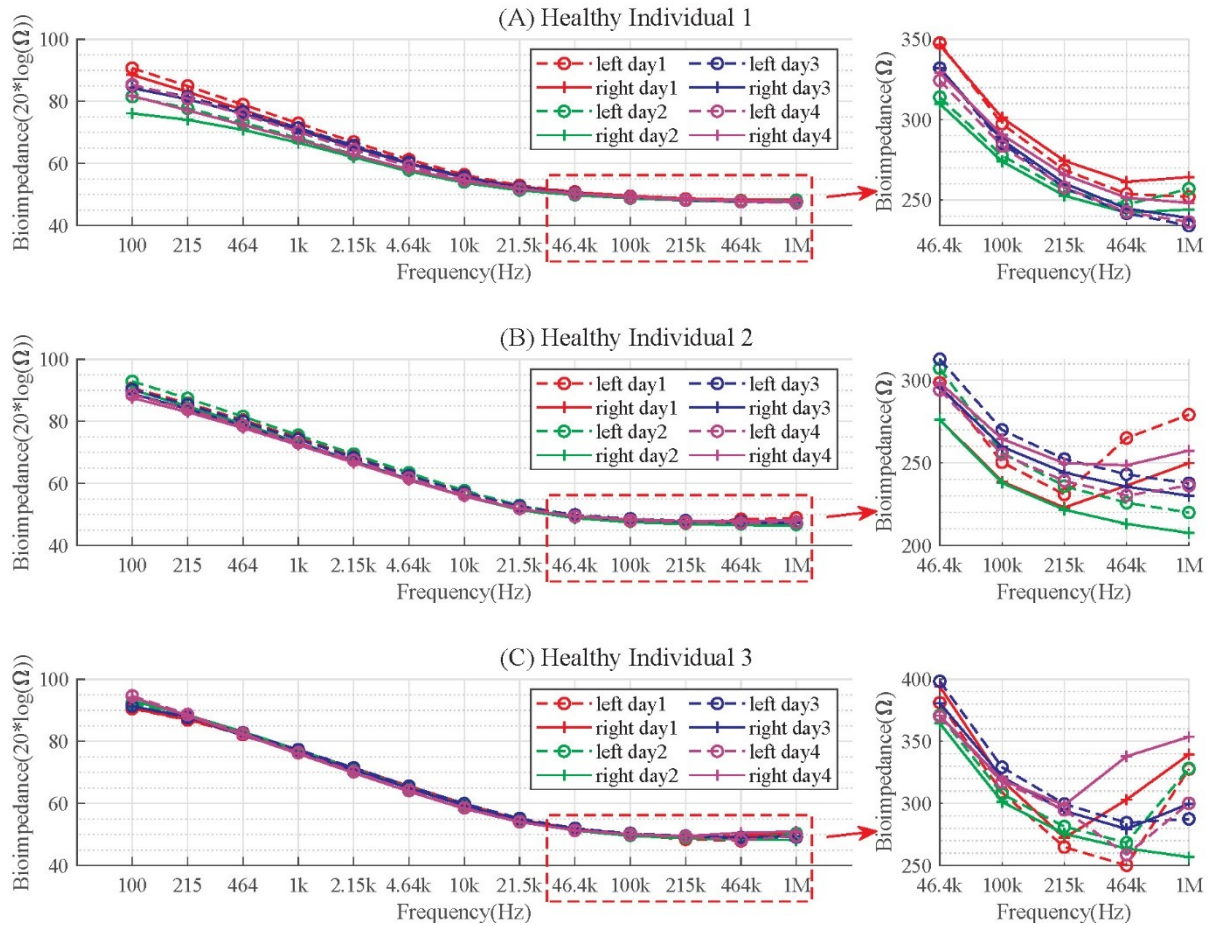


Figure 2.6 Bioimpedance measurements of left and right knees for three healthy individuals taken at 5-minute DS on four consecutive days, presented across a frequency range of 100 Hz to 1 MHz. (reproduced from [166]).

Similar observations can also be found from the bioimpedances of the knees of three healthy individuals measured at 5 min DS over four days, as depicted in Figure 2.6. The eight sets of bioimpedance data measured for the same individual varied considerably in the low-frequency range. For instance, for healthy individual 1, the bioimpedance of the left knee measured on day 1 was approximately five times that of the right knee measured on day 2 at 100 Hz. However, such variations were considerably smaller in the mid-to-high frequency range. In the frequency range from 46.4 kHz to 215 kHz, although the bioimpedance of the same subject

fluctuated up or down by up to 50 Ω across different days, most of the differences in the bioimpedance of the two knees of the same individual measured on the same day were less than 10 Ω . Furthermore, the bioimpedances in some datasets became irregular and tended to increase from 215 kHz to 1 MHz, which would only occur when the inductive reactance dominates the overall bioimpedance. This finding highlights the need for careful consideration of frequency ranges and external factors when analyzing bioimpedance data.

2.3.2 Bioimpedance Measurement of Knee Injuries

Table II Anthropometric characteristics of the patient group and the control group

	Patient Group n=45	Control Group n=37	Asymptotic Significance ^a
	Means (SD)	Means (SD)	
Age (years)	48.56 (17.46)	44.24 (14.61)	0.311
Height (cm)	166.43 (8.88)	168.81 (8.83)	0.395
Weight (kg)	64.93 (11.61)	68.67 (13.78)	0.384
BMI (kg/m ²)	23.44 (3.94)	23.91 (2.94)	0.445
Sex(male/female)	22/23	24/13	0.147

^aAsymptotic significances of age, height, weight, and BMI were calculated using the Kolmogorov-Smirnov test; The asymptotic significance of sex was calculated using the Pearson Chi-square test.

Table II shows the basic anthropometric characteristics of the patient group and the control group, including age, height, weight, BMI, and sex ratio. The Kolmogorov-Smirnov test and the Pearson Chi-square test results suggest that there is no significant difference observed in the anthropometric characteristics between the two groups.

The t-test results for Δ_{z_p} and Δ_{z_h} at various frequencies are presented in Table III. Figure 2.7 illustrates the distribution of Δ_{z_p} and Δ_{z_h} against frequency using boxplots. Samples were excluded if any data was missing or if the measured bioimpedance of one knee was more than twice that of the other at frequencies below 10 kHz or above 464 kHz. The reasons for this

exclusion will be explained in the discussion section. The remaining valid samples for analysis included 37 healthy controls and 39 patients.

Table III T-test results of Δ_{z_p} and Δ_{z_h} at different frequencies

Frequency	Patient Group n=39 Means(SD)	Control Group n=37 Means(SD)	t-test for Equality of Means (Equal variances not assumed)				Levene's Test for Equality of Variances Sig.
			Sig. (2- tailed)	Mean Diff	95% CI Lower Upper		
1 MHz	-6.17%(16.23%)	1.37%(13.23%)	0.0231	-7.54%	-14.01%	-1.06%	0.620
464 kHz	-4.67%(13.30%)	2.17%(12.87%)	0.0208	-6.84%	-12.62%	-1.07%	0.770
215 kHz	-5.51%(6.92%)	-0.55%(6.49%)	0.0013	-4.96%	-7.92%	-2.01%	0.630
100 kHz	-4.86%(6.30%)	-0.22%(4.66%)	0.0003	-4.64%	-7.05%	-2.22%	0.072
46.4 kHz	-3.92%(7.20%)	0.32%(4.64%)	0.0019	-4.24%	-6.86%	-1.61%	0.028
21.5 kHz	-2.50%(9.12%)	0.92%(6.18%)	0.0474	-3.42%	-6.80%	-0.04%	0.110
10 kHz	-1.11%(10.88%)	1.33%(7.58%)	0.2366	-2.44%	-6.51%	1.63%	0.125
4.64 kHz	-0.55%(11.91%)	1.50%(8.36%)	0.3644	-2.05%	-6.52%	2.42%	0.136
2.15 kHz	-0.16%(12.64%)	1.47%(8.91%)	0.4949	-1.64%	-6.39%	3.11%	0.135
1 kHz	0.02%(13.52%)	1.25%(9.59%)	0.6319	-1.23%	-6.32%	3.86%	0.127
464 Hz	0.25%(14.84%)	0.91%(10.69%)	0.8175	-0.65%	-6.28%	4.97%	0.133
215 Hz	0.44%(16.76%)	0.52%(12.64%)	0.9821	-0.07%	-6.54%	6.40%	0.186
100 Hz	0.54%(19.96%)	0.10%(16.29%)	0.9118	0.044%	-7.52%	8.41%	0.352

The most noteworthy findings are the statistically significant differences between Δ_{z_p} and Δ_{z_h} at 46.4 kHz, 100 kHz, and 215 kHz, where the p-values are approximately 0.001. At these three frequencies, the average Δ_{z_p} is around 5%, while the average Δ_{z_h} is close to zero. Therefore, 46.4 kHz, 100 kHz, and 215 kHz are selected as significant frequency sampling points (SFSPs) in the subsequent discussion. In contrast, there is no statistically significant difference at frequencies from 100 Hz to 10 kHz, where both Δ_{z_p} and Δ_{z_h} have mean values near zero. Moreover, the statistical significance between the two groups increases as the frequency rises from 100 Hz to 100 kHz but decreases as the frequency further increases from 100 kHz to 1 MHz. Additionally, the standard deviations for the patient group are larger than those of the

control group at all frequencies, with relatively large values observed at frequencies ≤ 10 kHz and ≥ 464 kHz. The tests for equality of variances suggest that the variances for the two groups may not be equal at 46.4 kHz.

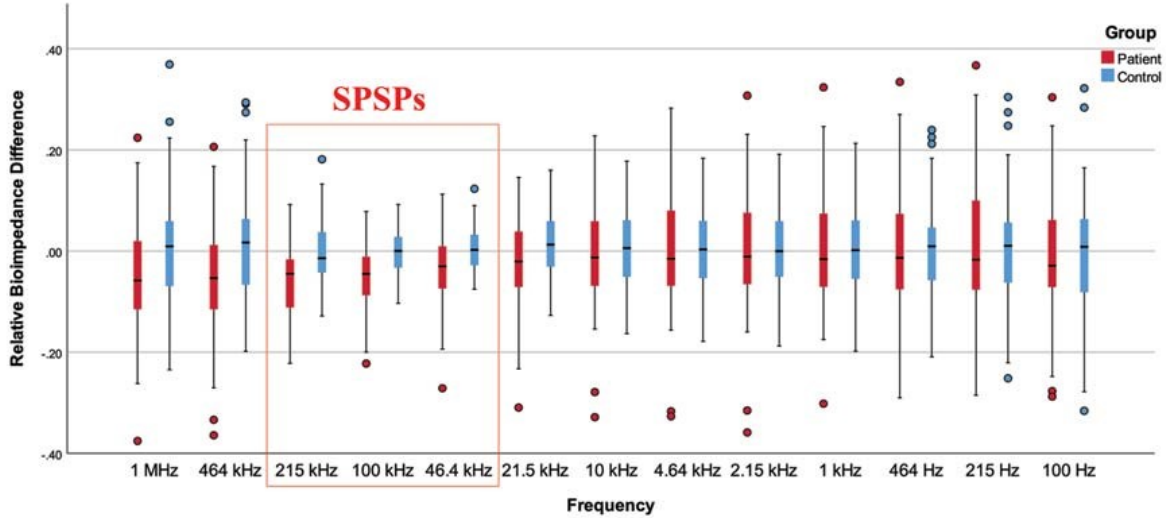


Figure 2.7 Box plots of the relative bioimpedance differences Δ_{Z_p} and Δ_{Z_h} at all frequency nodes, where the abbreviation SFSP(s) denotes significant frequency sampling point(s) (reproduced from [166]).

Δ_{Z_p} and Δ_{Z_h} at the three SFSPs were utilized as features in the machine learning process. Using PCA, two principal components (PCs) were derived from the 3-dimensional features. Subsequently, the SVM classified the patient and healthy control groups based on the two PCs. Figure 2.8 presents the visualized results of the PCA and the SVM predictor trained with all 76 valid samples. In the LOOCV used to evaluate the SVM classification results, 34 out of 39 patients and 27 out of 37 healthy controls were accurately classified. As a result, the SVM classification achieved a detection sensitivity of 87.18% and a specificity of 72.97%.

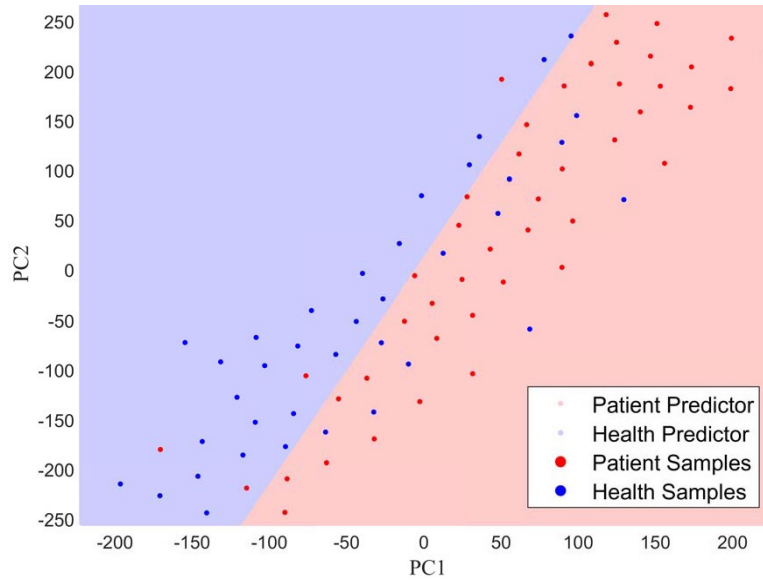


Figure 2.8 Principal components of the patient and control groups' SFSPs generated by PCA, along with the predictor created using SVM in the 2D plane (reproduced from [166]).

2.4 Discussion

2.4.1 Implications from the Feasibility Study of Bipolar Electrode Configuration

Based on the experiment results, we propose a simplified four-element equivalent circuit to present the influence of primary external factors on measured bioimpedance, as depicted in Figure 2.9(a). An increase in the duration of skin preparation, i.e. DS, would reduce both the resistive component (R_{esp}) and the capacitive component (C_{es}) by facilitating tighter contact between the electrode gel and the skin cuticle. However, this effect on bioimpedance measurements at high-frequency over 10 kHz will level off after 5 minutes of DS. The substantial decrease in bioimpedance over time, eventually plateauing, can be attributed to a more stable and closer contact between the electrode gel and the skin.

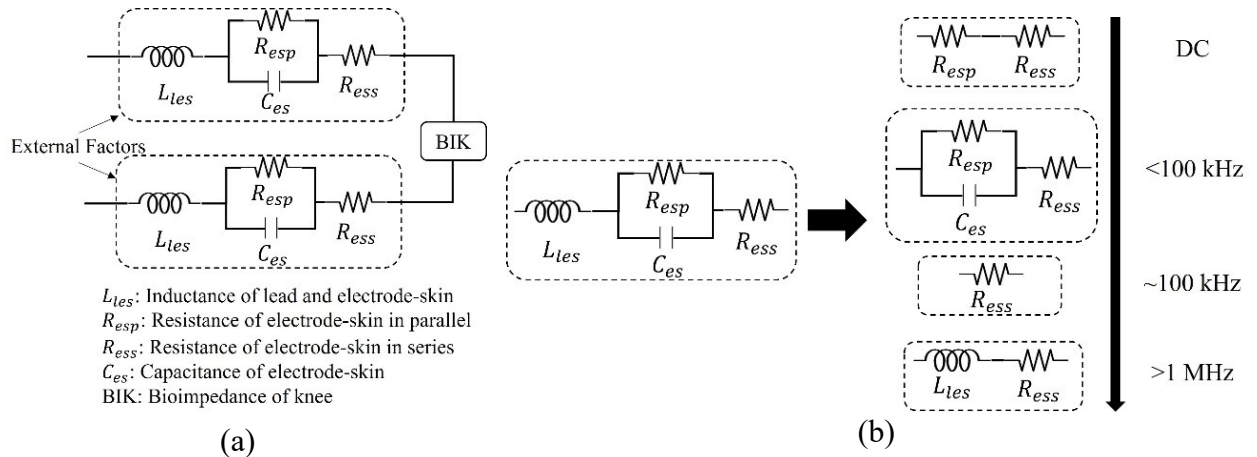


Figure 2.9 Equivalent circuit model in bioimpedance measurement: (a) Equivalent circuit model, and (b) Evolution of primary equivalent circuit elements representing external factors across a frequency range from low (DC) to high (>1 MHz). Both were reproduced from [166].

At approximately 100 kHz, C_{es} can be roughly equal to short-circuit, effectively minimizing the overall impact of electrode-skin impedance. Consequently, bioimpedance measurements at around 100 kHz exhibited minimal variation across different days or DS durations. Nevertheless, the inductance of leads and electrode-skin impedance can not be ignored when the frequency approaches the MHz level [137]. This could potentially explain the occasional higher measured bioimpedance at 1 MHz compared to 464 kHz, and the irregular bioimpedance values at 464 kHz and 1 MHz with increasing DS.

Building upon the two-resistor model proposed by Searle and Kirup [176], this model further elucidates the effects of skin-electrode in the high-frequency range. The simplified models in Figure 2.9(b) provide a concise representation of how the effective components of external factors vary with frequency. This model implies that variations caused by external factors can be minimized at around 100 kHz with DS durations longer than 5 minutes. Moreover, the model suggests that impedance measurements at low (< 10 kHz) and high (> 400 kHz)

frequencies could indicate whether external factor influences are consistent between measurements, offering a method for identifying and rejecting invalid samples.

During data analysis, the relative differences in bioimpedance between the two knees of each individual were calculated to investigate the relationship between bioimpedance and injuries, also known as self-contrast. To further enhance the significance of self-contrast, it is important to ensure that the influences of external factors are similar in the bioimpedance measurements of the same individual's two knees. As a result, samples were discarded if the measured bioimpedance of one knee exceeded twice the value of the other knee at low (< 10 kHz) and high (> 400 kHz) frequencies.

In summary, this study presents an extended model that explains for the influence of primary external factors on measured bioimpedance, suggesting that variations caused by these factors can be minimized at around 100 kHz with DS durations greater than 5 minutes. The model also provides a method for determining the consistency of external factor influences between measurements, which can help identify and remove invalid data. This approach is valuable in enhancing the significance of self-contrast when investigating the relationship between bioimpedance and injuries.

2.4.2 Detection of Knee Injuries Based on the Bioimpedance

The self-contrast results obtained from the patient group and the healthy control group align with the theoretical predictions about the impact of knee injuries on bioimpedance. Common knee injuries, such as OA, ligament ruptures, and meniscal lesions, typically involve the accumulation of effusion and damage to soft or hard tissues. The presence of effusion facilitates a conductive path for electrical current, while tissue damage decreases resistance

[159]. These tissue-level alterations within the knee can be reflected in changes to its electrical properties.

In the data analysis, the bioimpedance of the injured knee was found to be approximately 5% lower than that of the healthy knee in the patient group at the selected SFSPs. Since the knees of the same individual share the same genetics and grow under identical conditions, the healthy knee can be considered a healthy duplicate of the injured knee. Meanwhile, the relative bioimpedance differences in the healthy control group were close to zero for all sampling frequencies. Therefore, the Δ_{Z_h} values approaching zero suggest that the 5% bioimpedance reduction observed in the Δ_{Z_p} was primarily due to knee injuries. These findings also support the conclusions drawn from the feasibility study.

The bioimpedances measured at the three SFSPs demonstrated relatively small variances, corresponding to the frequency range that minimizes the influence of external factors in the proposed model. Additionally, it is notable that the variance in the patient group was greater than that in the control group. For the control group, the two healthy knees of the same individual were anatomically similar, indicating that their intrinsic bioimpedances should be nearly identical. Thus, the variance of Δ_{Z_h} primarily resulted from external factors. In contrast, the measured bioimpedances of the patient group were influenced by internal factors as well, including the severity and types of knee injuries. Consequently, the variances of Δ_{Z_p} were larger than those of Δ_{Z_h} at all frequencies.

The knee injury classifier exhibited a sensitivity of 87.18%, but its specificity was only 72.97%. Although the distributions of the two groups' PCs were distinguishable in the 2D plane, the significant overlap of the two clusters made separating the groups challenging. This overlap

was attributed to the considerable variance resulting from external factors. The means of Δ_p were almost equal to the standard deviations of Δ_{z_h} at the SFSPs, meaning that the average reduction in bioimpedance due to knee injuries was comparable to the measured bioimpedance error resulting from external factors. To achieve better sensitivity and specificity, future work should aim to further minimize the influence of external factors.

Despite these challenges, bioimpedance measurement remains a promising technique for early diagnosis of knee injuries and real-time monitoring of postoperative rehabilitation due to its low cost, portability, and accessibility. For instance, Jiang *et al.* developed a portable system capable of completing bioimpedance measurements from 100 Hz to 500 kHz within one second with an error of less than 2.5%, at a total cost of only \$45 [177]. In addition to low-cost bioimpedance measurement systems, several research groups have tried to create reusable electrodes made from materials such as metal, carbonized rubber, or textiles [178-181]. These reusable electrodes do not require electrolytes or adhesives, thus avoiding skin irritation problems associated with adhesive electrodes [182]. With the support of affordable portable bioimpedance measurement systems and reusable non-stick electrodes, bioimpedance measurement technology is expected to become more cost-effective and convenient in the future. Moreover, integrating this technology into wearable devices could enable the real-time collection of bioimpedance data from the knee, which could then be transmitted to physicians for further consultation and analysis.

2.5 Conclusion

In this study, we evaluated the feasibility of using the bipolar electrode configuration for knee bioimpedance measurements and explored the relationship between bioimpedance and knee injuries. Our feasibility study demonstrated that measurement errors caused by external factors

could be minimized at approximately 100 kHz with a > 5 min DS, while bioimpedance measurements at other frequencies may reveal the consistency of external factor influences among measurements. The self-contrast results revealed that knee injuries contribute to a 5% decrease in bioimpedance on average. Utilizing PCA and SVM for the binary classification of samples based on knee bioimpedance at the SFSPs, the classifier achieved a sensitivity of 87.18%. In conclusion, our findings suggest that the portable and cost-effective bioimpedance measurement technique holds promise for the early detection and ongoing monitoring of knee injuries, paving the way for future research and development in this area.

3. Electrochemical Impedance Spectroscopy Based Point-of-care Biomarker Detection: A Case Study on SARS-CoV-2 Detection

The content of this chapter has been published in in *Biosensors and Bioelectronics*: X 13 (2023): 100301 as "A portable, low-cost and high-throughput electrochemical impedance spectroscopy device for point-of-care biomarker detection" by Xuanjie Ye, Tianxiang Jiang, Yuhao Ma, Daniel To, Shuren Wang, and Jie Chen.

3.1 Introduction

In recent years, with the improvement of people's living standards, the demand for personalized healthcare has been growing, and the COVID-19 pandemic has further promoted this trend [183]. Conventional diagnostic techniques, which often require the use of complex instruments and skilled professionals, present challenges in meeting this growing demand. As such, POC diagnostics have become the preferred solution for personalized healthcare as it eliminates the need for specialized laboratory personnel and facilities while providing accessible diagnostic services [3]. To effectively implement POC diagnostics, it is crucial to develop low-cost, portable devices that offer rapid, accurate, and efficient detection or analysis of biomarkers [3, 184, 185]. Over the past few years, many research groups have focused on creating miniaturized bioanalytical devices for POC applications [186-189]. These devices have the potential to revolutionize healthcare delivery through early detection, monitoring, and management of various diseases, thereby improving patient outcomes and reducing the overall burden on the healthcare system.

The lab-on-chip (LOC) technique has become one of the most effective and practical approaches to achieving miniaturized POC devices [190]. Since the 1990s, advancements in

electrical engineering and integrated circuits (ICs) have provided the foundation for the LOC technique. LOC biosensors, which have advantages in rapid response times, portability, automation, high throughput, minimal reagent usage, and low-cost fabrication, have found widespread use in various biomedical research applications [190]. Utilizing micro- and nanofabrication techniques, IDE has emerged as a promising electrochemical biosensing LOC platform, offering enhanced sensing capabilities due to their microscale features [191]. Electrodes fabricated from biocompatible materials, such as gold, allow for surface characteristics that facilitate the detection of bacteria through the immobilization of targeted antibodies [192]. Moreover, the incorporation of nanoparticles enables label-free methods for concentrating and immobilizing biomolecules, further expanding the utility of these devices [193].

In recent years, research on the optimization of electrode geometry design has received increasing attention. The signal-to-noise ratio (SNR), which quantifies the strength of a signal relative to background noise, can be improved by fine-tuning the gap between the electrodes to fit specific bacterial sizes [194]. Another approach to improve the efficiency and impedance sensitivity of these biosensors involves manipulating the ratio between electrode width and gap size [195, 196]. Despite these advances, a limitation of current systems is that accurate impedance measurements typically rely on relatively bulky, expensive commercial instruments with complex interfaces. However, the continued development of electronic miniaturization offers a potential solution to make impedance-based biosensors portable and enable on-site POC detection. Therefore, IDE-based biosensors hold significant promise in both commercial and research applications, providing real-time, automated, and high-throughput testing at low cost [197-199]. By addressing the existing limitations and continuing to refine these LOC platforms,

researchers can achieve their full potential in revolutionizing personalized healthcare and diagnostics [200].

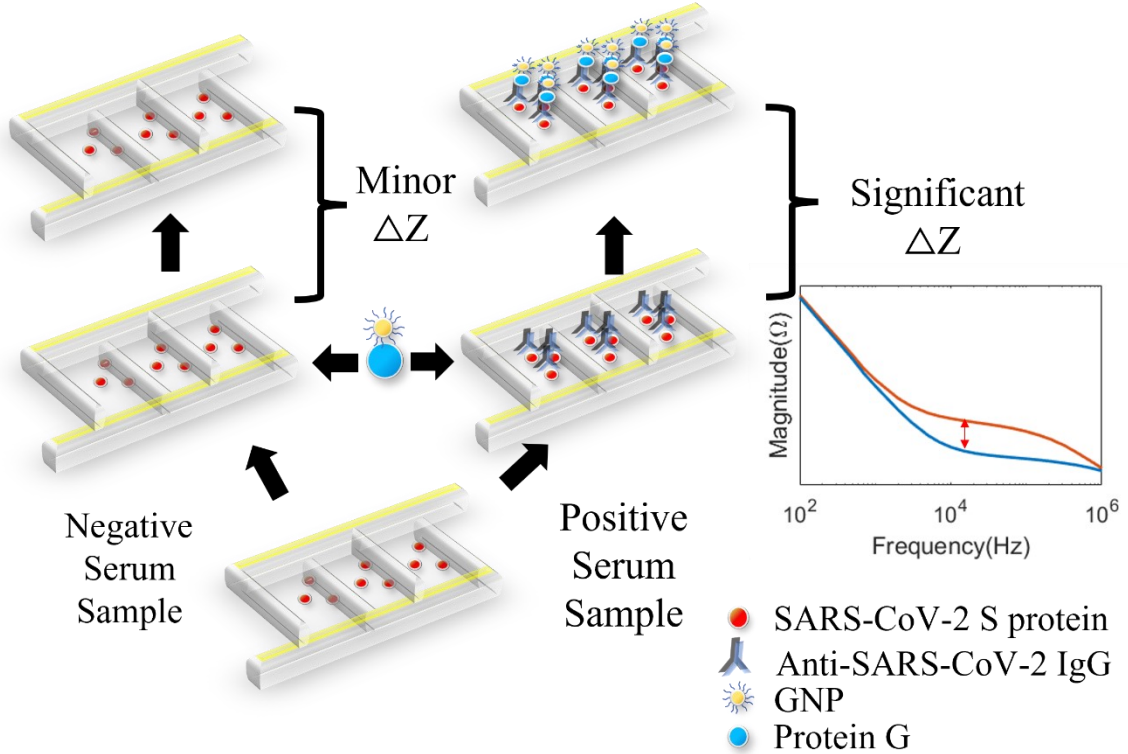


Figure 3.1 Overall representation of the proposed EIS-based method for biomarker detection utilizing an IDE chip (reproduced from [201]).

In this study, we proposed an EIS-based method for biomarker detection utilizing an IDE chip. This approach is specifically designed to fulfill the portability requirements of POC biomarker detection. The overall representation of this method, which highlights the key materials and processes involved, is illustrated in Figure 3.1. The IDE chip is a critical component of this approach, consisting of two distinct microelectrode array strips with an interdigitated structure that functions as the biosensor for detecting bioanalytics. The geometry of these IDE chips, which includes the dimensions of the electrode width and gap, significantly

affects their performance [194, 202]. To optimize the performance of the IDE chips, our study carefully selected an electrode width of 4 μm and an electrode gap of 5 μm based on our experimental test results. This configuration balances various factors such as yield, process, voltage, temperature (PVT) variation, and sensitivity to ensure good performance over a range of conditions. When developing the impedance measurement circuit design, we paid special attention to the amplitude of the excitation signal. By controlling the amplitude to a relatively low level of 10 mV, the electrodes can be protected from electrical breakdown, and it also minimizes thermal effects on the biosamples as well as maintains impedance linearity. This careful control of the excitation signal amplitude is essential to maintain the accuracy and reliability of the detection [203].

We chose SARS-CoV-2 detection as a case study to evaluate the effectiveness of this EIS-based biomarker detection method. Detecting the presence of anti-SARS-CoV-2 IgG in serum samples is a crucial step in identifying individuals who may have been exposed to the virus. This choice allows us to evaluate the performance of the proposed method in a real-world demand case. In the SARS-CoV-2 detection experiments, we employed gold nanoparticles (GNPs) conjugated with protein G (GNP-G) as secondary antibody probes. Here, the role of the GNPs is to enhance the influence of biomolecules on the dielectric properties of IDEs, thereby increasing the sensitivity of the detection method [204]. Our experimental results demonstrated statistical significance at 10 kHz ($p = 7 \times 10^{-6}$), suggesting that the EIS-based method using IDE chips holds promise for POC biomarker detection in a variety of applications. At 10 kHz, the impedance magnitude alteration caused by the GNP-G of the positive groups ranged from 11% to 55%, while that of the negative groups ranged from 2% to 8%. These results further highlight the effectiveness and sensitivity of the proposed method.

3.2 Materials and Methods

3.2.1 Detection Principles

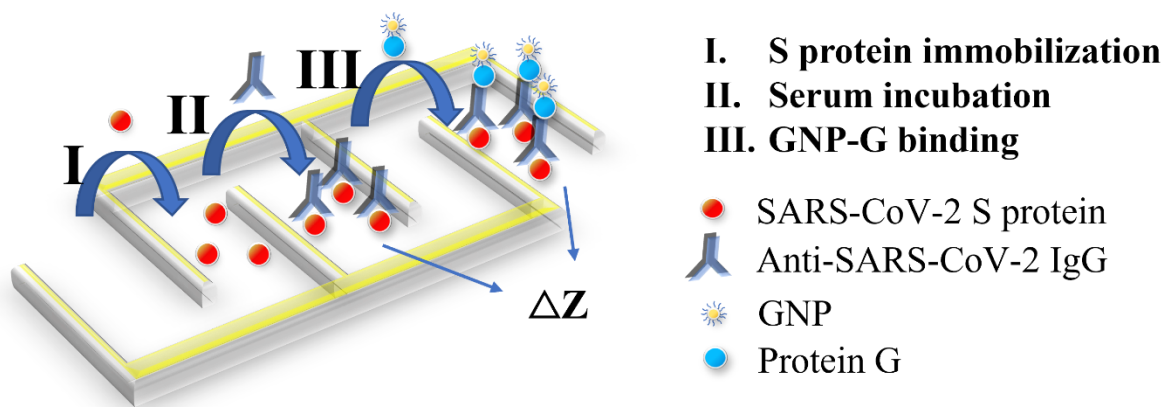


Figure 3.2 The mechanism of anti-SARS-CoV-2 IgG detection in serum samples using the IDE chip (reproduced from [201]).

The fundamental principle of detecting anti-SARS-CoV-2 IgG in serum using the IDE chip is to use GNP-G as the secondary antibody probe, resulting in changes in the impedance properties of the IDE chip, as illustrated in Figure 3.2. Initially, SARS-CoV-2 S proteins are immobilized onto the IDE chip using surface chemistry techniques. Subsequently, each well of the IDE chip is incubated with a 4 μL serum sample, diluted tenfold with 0.2% polyvinyl alcohol (PVA) in PBS, for 1 hour at 37°C to introduce anti-SARS-CoV-2 IgG antibodies. After serum incubation, the IDE chip is washed three times with 0.05% PBST (PBS containing 0.05% Tween-20). The IDE chip is then incubated with a GNP-G solution in PBS for 1 hour at room temperature in the dark to facilitate conjugation between GNP-G and IgG antibodies. After the GNP-G incubation, the IDE chip is rinsed three times with Milli-Q water. EIS measurements are performed before and after GNP-G incubation, with the IDE wells immersed in 60 μL of PBS (10 $\mu\text{M/L}$, pH 7.4) during the EIS process. For positive serum samples, the impedance of the

IDE is altered by the presence of GNP-G. In contrast, for negative serum samples, the impedance of the IDE remains unchanged since neither IgG nor GNP-G is introduced to the surface.

3.2.2 Materials

Trisodium citrate dihydrate, gold (III) chloride trihydrate solution, 10× phosphate-buffered saline (PBS, pH 7.4), 2-Morpholinoethanesulfonic acid monohydrate (MES), (3-Aminopropyl) triethoxysilane (APTES), Polyethylene glycol (PEG) 2-mercapto ethyl ether acetic acid (Mn 1000), N-(3-(dimethylamino)propyl)-N'-ethyl carbodiimide hydrochloride (EDC), and N-Hydroxysuccinimide (98% NHS) were obtained from Sigma-Aldrich. Polyvinyl alcohol, 98-99% hydrolyzed, was sourced from Alfa Aesar. The S protein was supplied by the National Centre for Foreign Animal Disease, Canadian Food Inspection Agency (Winnipeg, MB, Canada). Recombinant protein G was procured from ThermoFisher Scientific (catalog number 101201). The Public Health Laboratory (Alberta Precision Laboratories, Edmonton, AB, Canada) provided the positive and negative serum samples of anti-SARS-CoV-2 antibodies used in this study.

3.2.3 IDE Chip Design and Manufacture

The IDE biosensor used in this study features eight individual sensing regions, all sharing a common ground connection, as depicted in Figure 3.3. Each sensing region measures 3.3 mm × 3.3 mm, and electrodes within the region share identical dimensions. In our design, the electrodes have a width of 4 μm and a gap of 5 μm. This narrow separation between electrode pairs was chosen to enhance detection accuracy, as demonstrated in sensitivity simulations with varied electrode dimensions, which have been detailed in previous studies [205]. Considering the need to strike a balance between yield and fabrication costs, we adopted the lift-off technique to create the IDE sensor. The electrodes were composed of a Cr/Au bilayer with a thickness of

10/60 nm. A 10 nm Cr layer served as an adhesion layer between the glass substrate and the Au layer, while the 60-nm Au layer contributed to a higher yield during the fabrication process. This carefully considered design ensured a balance between precision and cost-effectiveness, enhancing the overall performance of the IDE biosensor.

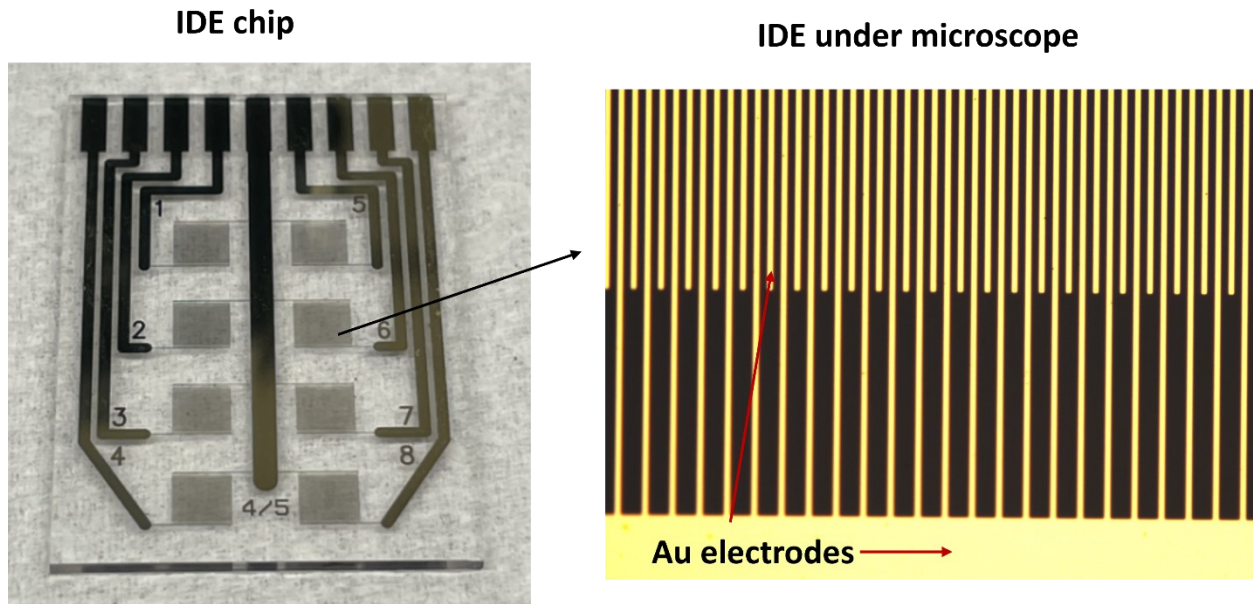


Figure 3.3 IDE biosensor and its micrograph (reproduced from [201]).

The fabrication process of the IDE biosensor is explained as follows. First, the Borofloat glass wafer underwent a thorough cleaning process using piranha solution to eliminate organic particles and other impurities. Following this, a single layer of HDMS was deposited to boost adhesion between the wafer surface and the photoresist. Subsequently, a bilayer photoresist composed of LOR 5B and AZ 1512 was spin-coated onto the wafer's surface. Next, the photoresist was exposed to UV light through a photomask at an intensity of 100 mJ/cm². The AZ 1512 photoresist was initially developed using a 1:1 AZ developer solution, followed by the development of LOR 5B photoresist in a 1:1 mixture of MF-319 developer and water. A Cr/Au bilayer was then deposited via e-beam evaporation. The metals, along with the photoresist, were

removed and left to soak in a PG remover solution overnight. Excess metals were subsequently rinsed off with acetone, isopropyl alcohol (IPA), and water. An additional layer of AZ 1512 photoresist was spin-coated onto the wafer's surface prior to the dicing process. Finally, acetone, IPA, and water were employed to strip the remaining photoresist, yielding a clean, precisely fabricated IDE sensor.

3.2.4 Surface Functionalization of S Protein

The IDE chips underwent a thorough cleaning process in acetone, isopropanol, and Milli-Q water using sonication to eliminate organic residues. Following this, an oxygen descum was performed for further cleaning using the Trion Phantom Reactive Ion Etching (RIE) System (setting parameters: 98% O₂, 150 mT pressure, 150 W RF, 120 seconds). The IDE electrode surface was then incubated in APTES for two minutes, after which the APTES was washed off by immersing the chip in ethanol and applying sonication. A Polydimethylsiloxane (PDMS) cover was subsequently bonded to the IDE chip's surface to delineate each unit under the buffer. After that, the SARS-CoV-2 S protein in a 1× PBS solution (0.1 mg/ml, pH 7.4) was incubated in the EDC/NHS solution (4 mg EDC and 22 mg NHS in 1 ml of 10 mM MES buffer) for 15 minutes. The S protein solution was then added to each well and incubated for 1 hour at 37°C. The wells were subsequently washed with 2% PBST and 1× PBS solution and incubated in a 0.2% PVA solution (PBS, pH 7.4) at room temperature overnight.

3.2.5 Formation of GNP

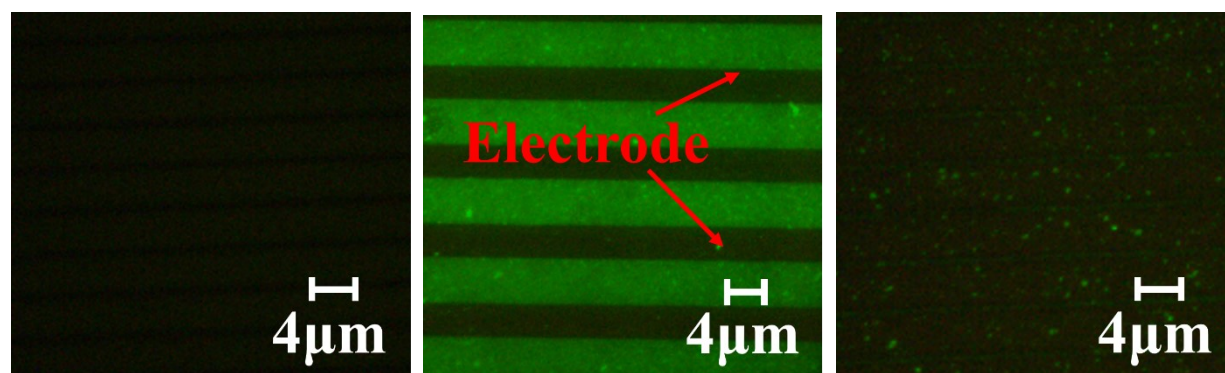
A 50 ml solution containing 1 mM gold (III) chloride trihydrate was prepared in a three-neck round-bottom flask, which was equipped with a magnetic stirrer and a condenser column. The solution was heated to its boiling point with an oil bath. Subsequently, 5 ml of 38.8 mM trisodium citrate dihydrate was introduced through an alternate neck of the round-bottom flask.

Once the solution changed to a dark wine-red color, reflux and stirring were sustained for an additional 15 minutes. After this period, the flask was removed from the oil bath and allowed to return to room temperature, with stirring persisting throughout the cooling process. Finally, the solution was filtered using a 0.45 μm syringe filter and stored at 4°C in darkness.

3.2.6 Surface Characterization of GNP

A 5 ml PEG solution was prepared by combining 0.605 μM PEG methyl ether thiol (Mn 1000) and 0.605 μM MUA. This PEG solution was added dropwise to 5 ml of 13.3 nM GNP solution, followed by overnight stirring to facilitate the functionalization of GNPs. The solution was then centrifuged at 13,000 g and 4°C for 20 minutes, with the resulting pellet resuspended in Milli-Q water. This centrifugation and resuspension process was repeated until an optical density of 50 was achieved, which was measured using the Evolution 60S UV-Visible Spectrophotometer (Thermo Fisher Scientific, MA, United States). An EDC/NHS solution was prepared by dissolving 30 mg EDC and 36 mg NHS in 1 ml of 10 mM MES buffer. Subsequently, the GNP solution and the EDC/NHS solution were mixed at a 1:1 ratio and incubated for 30 minutes at room temperature. Following incubation, the mixture was centrifuged at 13,000 g for 1 hour at 4°C to obtain the concentrated GNP solution. Next, 40 μL of 1 mg/ml protein G solution was mixed with the GNP solution under sonication. Then, the resulting mixture was incubated on a shaker at room temperature for 3 hours. The solution was then vortexed with 1 ml of 0.05% PBST and centrifuged at 13,000 g and 4°C for 1 hour. After removing the supernatant, the pellet was resuspended in 200 μL of 1 \times PBS. The prepared GNP-G solution should be stored at 4°C in darkness.

3.2.7 Verification of IgG Antibody Interaction with the SARS-CoV-2 Spike Protein



(a)

(b)

(c)

Figure 3.4 Fluorescence microscopy images of IDE chips: (a) control without serum exposure, (b) incubated with SARS-CoV-2 positive serum sample, and (c) incubated with SARS-CoV-2 negative serum sample (reproduced from [201]).

In the preliminary experiments, fluorescent-labeled secondary antibodies targeting anti-SARS-CoV-2 IgG (Alexa-anti-IgG) were utilized to verify the specific binding between IgG and the S protein. Following S protein immobilization, the IDE chips were incubated with the fluorophore-labeled secondary antibodies under three conditions: without serum exposure, with a positive serum sample, and with a negative serum sample, and the results were illustrated in Figure 3.4. Fluorescence images were captured using the ChemiDoc MP Imaging System. Without serum exposure, the fluorophore-labeled secondary antibodies did not exhibit specific binding, resulting in negligible fluorescence detection on the chip. However, upon incubation with the positive serum sample, specific binding to the fluorophore-labeled secondary antibodies could be observed throughout the gaps between the electrodes. Conversely, the IDE chip exposed to the negative serum sample displayed only a few instances of nonspecific binding and minimal fluorescence detection. These findings substantiate that the S protein immobilized on

the IDE chip can selectively interact with the anti-SARS-CoV-2 IgG present in the positive serum sample.

3.3 Results and Discussion

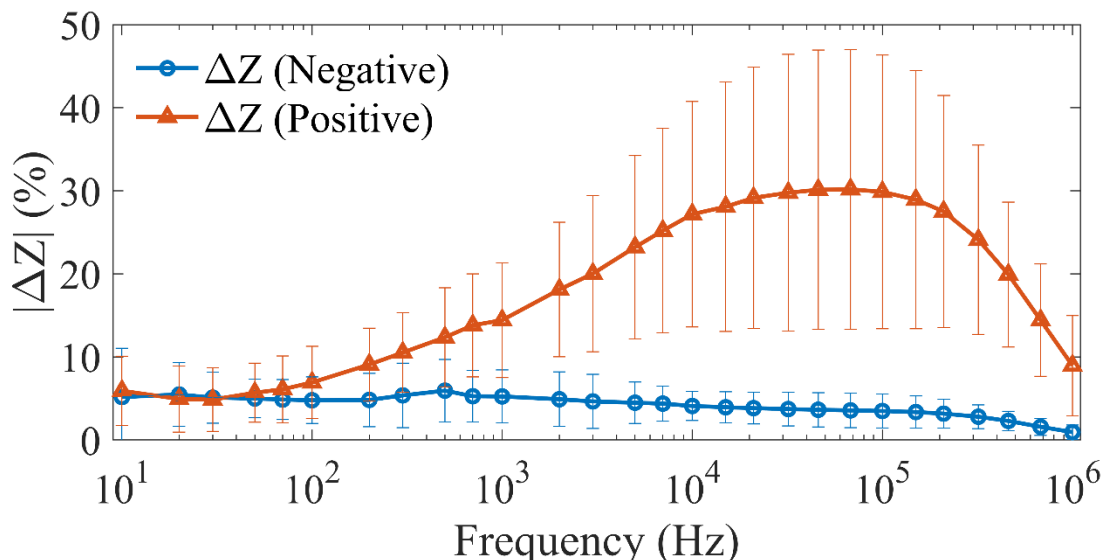


Figure 3.5 $|\Delta Z|$ between serum incubation and GNP binding steps for positive and negative samples across a frequency range of 10 Hz to 1 MHz (N = 12) (reproduced from [201]).

EIS was employed as a method for the analysis of both serum incubation and GNP-G binding steps in 12 positive and 12 negative samples. The efficiency evaluation of the IDE biosensor in detecting the presence of anti-SARS-CoV-2 IgG antibodies is based on the comparison of the relative differences in impedance (ΔZ) between these two values. The result is illustrated in Figure 3.5, where the statistical significance can be observed across a frequency range from 1 kHz to 1 MHz, with the highest level of statistical significance at 10 kHz ($p = 7 \times 10^{-6}$). At this specific frequency point, $|\Delta Z|$ of the positive group varies considerably, ranging from 11% to 55%. In contrast, the negative group exhibits a much narrower range from 2% to 8%. The positive and negative samples can be separated by employing a $|\Delta Z|$ cut-off value of

10%. These findings are in line with the theoretical expectation that the use of GNPs can effectively amplify the changes in dielectric properties caused by the presence of biosamples [205].

The observed high statistical significance can be partly attributed to the small standard deviation of the negative group (1.7%). This is due to the fact that variations in impedance change within different positive tests are inevitable, given the variations happen in the steps of immobilization of S protein, incubation of serum samples, and GNP-G binding. Conversely, the variance within the negative sample group primarily arises from minor reagent residues on the IDE chip during serum incubation and GNP-G binding. Similar results have been observed in other research studies as well [206]. However, our study obtained better results compared to previous work by employing IDE chips with an electrode width of 4 μm and an electrode spacing of 5 μm . By adopting a relatively larger electrode spacing, the impact of PVT variation on the IDE chip differences can be effectively mitigated. Although this may result in a slight reduction in the sensitivity of the IDE chip, the decreased difference among IDE chips leads to a smaller standard deviation within the negative group, making the positive and negative groups more distinguishable. Furthermore, the larger electrode spacing leads to a higher IDE chip yield, which can contribute to cost reductions. This balance between sensitivity and cost efficiency demonstrates the potential of the proposed device in providing a reliable and affordable means of distinguishing between positive and negative samples, making it a valuable alternative to the field of POC diagnostics.

The impedance values in the low-frequency range (10 to 30 Hz) can be utilized to validate the reliability of the data. For both positive and negative groups, the relative impedance differences ($|\Delta Z|$) range from 0 to 12%. These minor changes do not apply to IDE chips that may

have been contaminated during the serum incubation or GNP-G binding process. In certain cases, samples exhibited significant $|\Delta Z|$ values across the entire frequency range, and upon inspection, their corresponding IDE wells displayed signs of contamination or damage. As a result, these samples were deemed unreliable and subsequently excluded from the data analysis. The reliability of the data was validated by carefully assessing the impedance values in the low-frequency range and excluding potentially unreliable samples from the study. This rigorous approach to data validation ensures that the results obtained are reliable and representative, contributing to the overall robustness of the research findings.

3.4 Conclusion

In this study, we presented an EIS-based method for biomarker detection utilizing IDE biosensors, which demonstrated excellent capability in detecting anti-SARS-CoV-2 IgG in serum samples. This EIS-based detection method offers several advantages including rapid response, high sensitivity, and minimal sample requirements. The experiment results presented high statistical significance in the impedance change at 10 kHz ($p = 7 \times 10^{-6}$) for anti-SARS-CoV-2 IgG antibody detection. At this frequency, the relative impedance differences ($|\Delta Z|$) between the positive and negative groups were distinct ($27.2\% \pm 13.6\%$ for the positive group versus $4.1\% \pm 1.7\%$ for the negative group), indicating a clear separation between the two groups. The EIS-based anti-SARS-CoV-2 IgG antibody detection method on the 8-well IDE chip requires only 4 μL of serum and can be completed in two hours. Moreover, the IDE biosensor platform offers the potential for multiplexing, enabling the simultaneous detection of multiple biomarkers in an assay, which could improve the throughput and utility of diagnostic tests. Furthermore, this detection approach also holds the potential to be applicable for the detection of other biomarkers

by synthesizing corresponding antibody conjugates GNPs. This versatility promises to make the technology a rapid and effective diagnostic tool for a variety of diseases and conditions.

4. A Portable and Low-cost Electrochemical Impedance Spectroscopy System for Point-of-care Testing

The content of this chapter has been published in in *Biosensors and Bioelectronics*: X 13 (2023): 100301 as "A portable, low-cost and high-throughput electrochemical impedance spectroscopy device for point-of-care biomarker detection" by Xuanjie Ye, Tianxiang Jiang, Yuhao Ma, Daniel To, Shuren Wang, and Jie Chen.

4.1 Introduction

In recent years, the measurement of bioimpedance through impedance spectroscopy, also known as EIS, has been widely applied in evaluating biological samples, identifying and tracking physiological conditions, and promoting new developments in biomedical applications [207, 208]. Biological tissues demonstrate frequency-dependent characteristics because cell membranes exhibit a capacitive quality [209]. Low-frequency currents (below 1 kHz) can only go through ECF since they cannot penetrate the cell membranes, while high-frequency currents (exceeding 1MHz) pass through both ECF and ICF.

The bioimpedance measurement at a range of frequencies yields impedance spectrum data, which reveals insights into biological tissue states or processes [210, 211]. EIS has become particularly popular in the biomedical research area due to its relative immunity to interference, detailed process information, rapid response, and dependable outcomes [212]. Biological tissues can be treated as being equivalent to electronic components, and most functional abnormalities in human organs or changes in cellular activity can be represented as shifts in the electrical properties of these tissues [213-215]. Analysis of impedance spectroscopy data can extract important physiological and pathological functional details from biological tissues [216].

Practical applications of this technology include the detection of inflammation and dysplasia in Barrett's esophagus within the upper gastrointestinal tract [217], as well as a diagnostic instrument for identifying and monitoring mucosal damage resulting from ischemia in critical diseases [218]. With EIS, researchers and medical professionals can access a lot of information that aids in the diagnosis, monitoring, and understanding of various physiological and pathological conditions.

The bioimpedance measurement of biological tissue requires applying a broad frequency band of excitation signals and minimizing the impact of noise on the measurement results [219]. This necessitates a high degree of accuracy in the measuring device. Impedance analyzers, traditional EIS detection devices, measure the impedance of test subjects over a broad frequency range. The primary advantages of these analyzers are a wide frequency range and high measurement accuracy. However, their large size and high-cost limit their application in POC testing within the realm of EIS.

To address these limitations, researchers have developed several portable EIS devices. Recichmuth *et al.*, for example, developed a non-invasive, wearable bioimpedance measurement device specifically for monitoring bladder filling [220]. Additionally, ImpediMed SFB7, a portable and high-precision EIS system developed by ImpediMed Limited (Australia), is currently commercially available and has been successfully implemented in the biomedical field [221]. Ferreira *et al.* created an EIS system based on AD5933, which achieves continuous measurements in the 0-100 kHz range with an error of less than 1% [222]. Li *et al.* designed an electrical auto-balanced bridge EIS device that exhibited an error of less than 2% within the 10 kHz - 10 MHz frequency range [223]. Ruiz-Vargas *et al.* designed an EIS device based on Red-Pitaya, featuring an error of less than 2% in the 10 Hz - 1 MHz frequency range [224]. These

portable devices demonstrate excellent performance in terms of both frequency range and accuracy, making them valuable tools for EIS in a variety of POC applications.

In this study, we present a miniaturized EIS device specifically designed to fulfill the portability requirements of POC diagnostic devices, and it shows excellent performance in terms of precision, accuracy, and measurement speed. A notable feature of our design is that the excitation signal amplitude is controlled to a low level of 10 mV, which serves multiple purposes, including safeguarding the electrodes, minimizing potential thermal effects on the biosamples, and preserving the impedance linearity throughout the measurement process [203, 225]. To balance the performance of our device, we employed two different types of excitation waveforms for the different frequency ranges. For the frequency range below 1 kHz, we utilized multi-tone signals, which significantly accelerates the measurement process. On the other hand, for higher frequencies, single-tone sinewaves are implemented to guarantee precision and reliability [25]. Our proposed system demonstrated excellent performance within the critical frequency range of 1 kHz to 1 MHz, exhibiting an average magnitude accuracy error of 0.30%. Despite achieving this level of accuracy, our EIS device maintains its miniaturization and portability, which make it suitable for POC applications. Moreover, scanning 28 frequency points in a quasi-logarithmic distribution from 10 Hz to 1 MHz required only 0.46 seconds. The combination of speed, accuracy, and portability offered by our miniaturized EIS device makes it a promising solution for a wide range of EIS applications in various healthcare POC settings.

4.2 Hardware and Algorithm Design

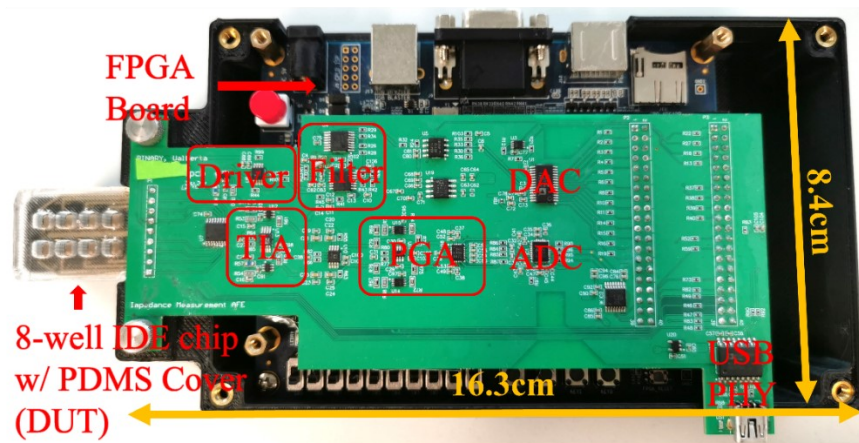
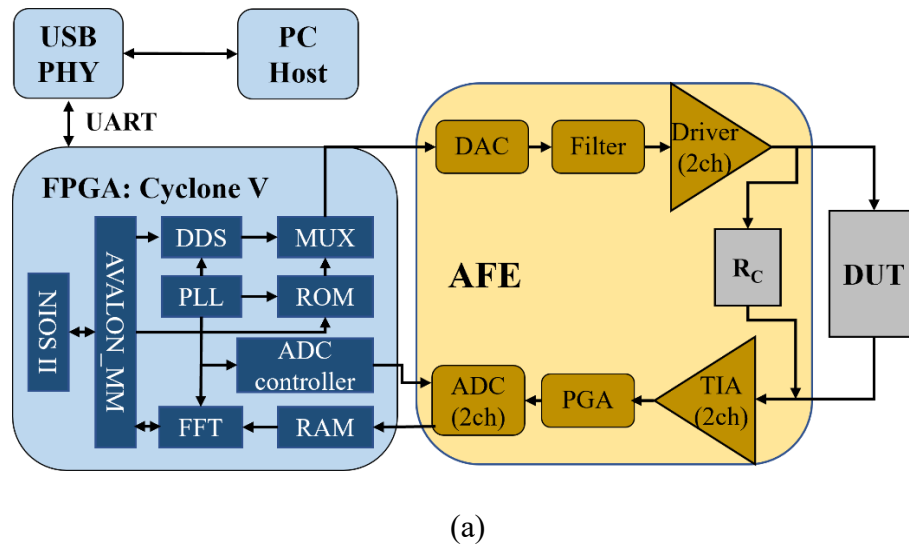


Figure 4.1 (a) Comprehensive circuit block diagram of the EIS system. (b) Prototype of the proposed EIS system. Both were reproduced from [201].

The proposed portable EIS system consists of two major components: a Field-Programmable Gate Array (FPGA) module and an Analog Front-End (AFE) circuit. The system employs the IDE chip, as presented in Chapter 3, as the device under test (DUT). The FPGA module is responsible for the management of the digital signals within the EIS system, with its

primary functions including digital signal input and output, computation, and communication. The AFE circuit generates excitation signals based on the output digital signals derived from the FPGA module and collects feedback signals from the DUT. The comprehensive circuit block diagram of the proposed system is illustrated in Figure 4.1(a), and the actual prototype is depicted in Figure 4.1(b). The total cost of the entire system can be effectively controlled, remaining below US \$100 when produced in volume.

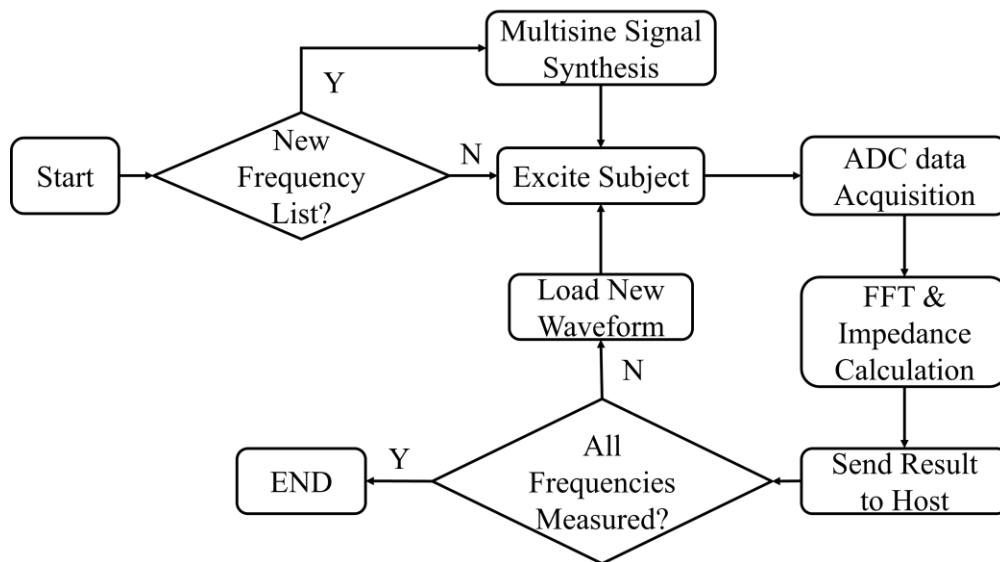


Figure 4.2 Flow chart of the impedance measurement process (reproduced from [201]).

To enhance the efficiency of the impedance measurement process, the proposed system employs multi-tone signals in the low-frequency range (below 1 kHz) to excite the samples. This approach enables the simultaneous measurement of multiple frequency points within a single excitation, accelerating the procedure. On the contrary, in the high-frequency range (above 1 kHz), the measurement speed using single-tone sinewaves is not slow, so there is no need to sacrifice SNR in exchange for faster measurement speeds. Furthermore, the FPGA chip handles all computations, requiring the host to only transmit measurement instructions and receive

impedance results. This approach significantly reduces the time needed for transferring large volumes of recorded data to the host. A flow chart illustrating the complete measurement process can be found in Figure 4.2.

4.2.1 Analog Front-End Circuit Design

The basic method for measuring complex bioimpedance involves applying a specifically designed signal with one or multiple frequency components to the DUT. Subsequently, the electrical current's magnitude and phase through the sample, as well as the voltage across it, are measured. The proposed system employs the potentiostat protocol, which keeps the excitation voltage across the subject constant [226].

The digital-to-analog converter (DAC) chip AD9742, controlled by digital signals from the FPGA module, generates the excitation signals. To ensure linearity and to protect the biological samples, the excitation signal is limited to 10 mV [227]. The excitation signal passes through a second-order low-pass Butterworth filter to eliminate high-frequency noise, primarily the DAC's clock signal interference noise (22.528 MHz). Afterward, the signal is applied to the calibration resistance and the DUT using two identical drivers built with a dual op-amp (OPA2353).

The proposed EIS system uses an automatic balance bridge circuit topology to maintain the potentiostat structure. Traditional potentiostat circuit topology employs an electrometer module to sense the DUT's potential, with the voltage signal fed back to the control amplifier, as shown in Figure 4.3(a). Additionally, the DUT's current signal is converted into a voltage signal using a precision resistor R_m , and the signal is sensed using an amplifier. In contrast, the automatic balance bridge method has a simpler topology, as shown in Figure 4.3(b). A

transimpedance amplifier (TIA) converts the current through the DUT into a voltage signal for current signal sensing. One DUT port is fixed to the ground due to the virtual ground effect, ensuring the potential automatically equals the excitation signal. Therefore, the proposed portable EIS system uses the automatic balance bridge method to reduce the circuit area. The dual high-speed, ultra-low bias current op-amp chip LTC6269 forms the 2-channel TIA, with its fA-level bias current feature ensuring precise current flow through the DUT and feedback resistor R_m , improving impedance measurement accuracy. Two precision resistors (200 Ω and 10 k Ω) function as R_m to transform different current levels, selected by a low on-resistance single pole double throw (SPDT) analog switch ADG849.

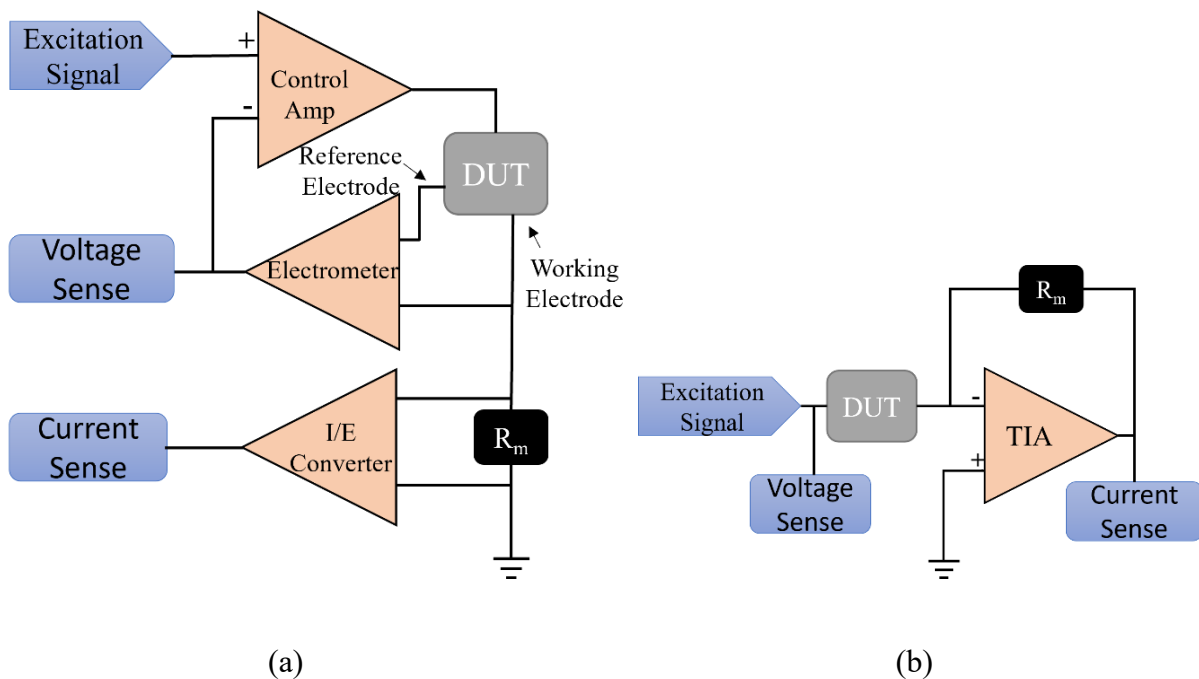


Figure 4.3 (a) Block diagram of traditional potentiostat topology (b) Block diagram of automatic balance bridge topology (reproduced from [201]).

The TIA transforms the current signal into a voltage signal, which is then adjusted by an amplifier before being digitized by the analog-to-digital converter (ADC). The current flowing

through the DUT is relatively low, typically from nA to uA levels, due to the excitation signal's 10 mV low amplitude. Consequently, the output voltage range can be adjusted from 0.1 mV to 20 mV in most cases. The TIA's output voltage is adjusted by programmable-gain amplifiers (PGA) to fully utilize the ADC's input range and reduce quantization noise. The low-noise, high-speed dual 16-bit successive approximation register (SAR) ADC chip LTC2323-16 is employed in the proposed system, allowing a frequency range of up to 2.5 MHz, exceeding our target maximum frequency of 1 MHz. To speed up impedance measurement, the current signals through the calibration resistor R_c and the DUT are sensed simultaneously. To diminish the influence of parasitic capacitance and resistance, two symmetrical signal paths are constructed on the printed circuit board (PCB).

4.2.2 Digital Circuit Design

The FPGA module handles all digital circuit functions within the system, including clock signal generation, signal acquisition, signal processing, computation, and communication. To prevent clock mismatches, the clock signals of the DAC and ADC are derived from the same phase-locked loop (PLL) module on the FPGA. This synchronization, combined with carefully designed excitation signals and signal acquisition length, assures that the signal stored in the RAM consists of one or several complete periods of the periodic excitation signal. In this way, the system can effectively eliminate spectrum leakage without window functions. This approach enhances the accuracy of the signal's magnitude and phase calculations, which are performed using the Fast Fourier Transform (FFT) [228].

The FPGA circuit module utilized in the system is the P0192 Cyclone FPGA development board (Terasic Technologies, Taiwan), which incorporates the Cyclone V 5CEBA4F23C7N as its core chip. Within the FPGA, the PLL module generates a 180.224-MHz

master clock, which is subsequently divided into different clocks for other modules. The master clock is divided by 8 to create a 22.528-MHz clock for both the direct digital synthesis (DDS) module and the DAC chip. The DDS module, designed using the Numerically Controlled Oscillator (NCO) IP of Altera Corporation, generates single-tone sine wave signals across various frequencies. The 22.528-MHz clock is chosen to control the DDS module, ensuring optimal SNR for high-frequency signals (above 1 MHz) and adequate resolution. Next, the ADC controller module generates the ADC signal acquisition control signal based on the master clock (180.224 MHz). A complete 16-bit digital signal can be collected every 44 clock cycles, resulting in an ADC sampling frequency (f_s) of 4.096 Msps. Lastly, the FFT module, which utilizes the FFT core function provided by Altera Corporation, directly adopts the master clock to guarantee data processing speed. The real-part input of the FFT module comprises the digital signal acquired by the ADC, while the imaginary part input is set to zero. The transform length is configured to $N = 4096$, establishing a fundamental frequency of $f_0 = f_s/N = 4.096 \text{ MHz}/4096 = 1 \text{ kHz}$. Utilizing the output data from the FFT module, the NIOS II – a synthesized 32-bit embedded processor supplied by Altera Corporation – calculates the complex impedance using Equations (4.1)-(4.4).

$$|X[k]| = \sqrt{\text{Re}X^2[k] + \text{Im}X^2[k]} \quad (4.1)$$

$$\theta[k] = \arctan\left(\frac{\text{Im}X[k]}{\text{Re}X[k]}\right) \quad (4.2)$$

$$|Z_{DUT}[k]| = \frac{|X_c[k]|}{|X_{DUT}[k]|} \cdot R_c \quad (4.3)$$

$$\theta_{DUT}[k] = \theta_{R_c} + \theta_{X_c} - \theta_{X_{DUT}} = \theta_{X_c} - \theta_{X_{DUT}} \quad (4.4)$$

The index [k] denotes the value at the frequency point of k kHz. $\text{Re}X$ and $\text{Im}X$ represent the real and imaginary components of the signal, as outputted from the FFT module, respectively. $|X|$ and θ correspond to the magnitude and phase of the signal, respectively. $|X_c|$ and $|X_{\text{DUT}}|$ signify the magnitudes of the current signals flowing through the calibration resistor R_c and the DUT, respectively. $|Z_{\text{DUT}}|$ and R_c represent the magnitude of the DUT's impedance and the resistance of the calibration resistor R_c , respectively. θ_{DUT} , θ_{X_c} , and $\theta_{X_{\text{DUT}}}$ are the phases of the DUT's impedance and the current signals flowing through R_c and DUT, respectively. θ_{R_c} refers to the phase of the calibration resistor R_c , which is assumed to be zero.

The transform length of $N = 4096$ and the sampling frequency $f_s = 4.096$ MHz yield the lowest measurement frequency point of 1 kHz. To assess the complex impedance within the frequency range below 1 kHz, the system necessitates either a longer transform length or a reduced sampling frequency. The latter is more feasible, as it only requires modifying the clock frequency of the ADC controller. On the other hand, merely changing the sampling frequency would underutilize the high-speed capabilities of the ADC. Consequently, the proposed system incorporates a data averaging module to decrease the sampling frequency, simultaneously enhancing the SNR of the acquired signal. By averaging the results of N consecutive samples from the ADC as a single sampling data point, the sampling frequency can be reduced by a factor of N . This adjustment shifts the lowest measurement frequency point to $1/N$ kHz. Concurrently, the SNR of the signal acquisition improves by $10 \cdot \log_{10}(N)$ dB.

4.2.3 Excitation Signal Design

In most cases, EIS measurement employs single-tone sine wave signals as the excitation source due to their high SNR, which ensures accurate measurement results. However, this approach can lead to a lengthy measurement duration for a complete EIS since only one

frequency can be assessed at a single excitation. When evaluating impedance at low frequencies, such as at the Hz or even mHz level, the exceptionally long time required for a full EIS may be impractical in certain situations, particularly for dynamic biological monitor systems. As a result, wide bandwidth excitation signals have been adopted to reduce EIS measurement time. These signals possess spectral densities that encompass multiple frequency points or span entire frequency ranges. Commonly utilized wide bandwidth signals in EIS systems include multi-tone signals [229, 230], chirp signals [177, 231], sinc signals [232, 233], rectangular pulses [234], and Gaussian functions [235], which facilitate more efficient impedance measurements.

In the proposed EIS system, broadband signals are employed for measurements in the low-frequency range (below 1 kHz) to accelerate the measurement speed. Complex impedance evaluations at low frequencies can be time-consuming, as the system needs to acquire one or several complete sine waves. Using broadband signals for excitation effectively reduces the measurement duration required since multiple frequencies can be measured with a single excitation. Additionally, the low SNR issue associated with broadband signals can be alleviated by the SNR improvement offered by the data averaging module. For the high-frequency range (above 1 kHz), measurement speed is naturally faster, rendering the use of broadband signals unnecessary. Consequently, the excitation signals for the proposed system comprise broadband signals in the low-frequency range (below 1 kHz) and single-tone signals in the high-frequency range (above 1 kHz). This approach ensures efficient and accurate impedance assessments across board frequency ranges.

The multi-tone signal is chosen as the broadband excitation signal in the low-frequency range due to its efficient energy utilization at the desired frequency points. A multi-tone signal is the sum of multiple sine waves at varying frequencies, providing high flexibility in shaping the

target spectrum. However, without careful phase arrangement for each frequency component, a multi-tone signal may exhibit a high crest factor (CF), which represents the peak to root mean square (RMS) ratio, as expressed in Equation (4.5). In the proposed EIS system, the excitation signal's peak value is limited to ± 10 mV to maintain the bioimpedance linearity of the biological samples. Given this peak value constraint, the excitation signal should have a minimal CF to maximize excitation energy and SNR. Consequently, the phases of the frequency components must be appropriately arranged to minimize the CF of the multi-tone excitation signal, enhancing the measurement accuracy.

$$CF = \frac{\max_{0 \leq t \leq T} |x(t)|}{\sqrt{\frac{1}{T} \int_0^T |x(t)|^2 dt}} \quad (4.5)$$

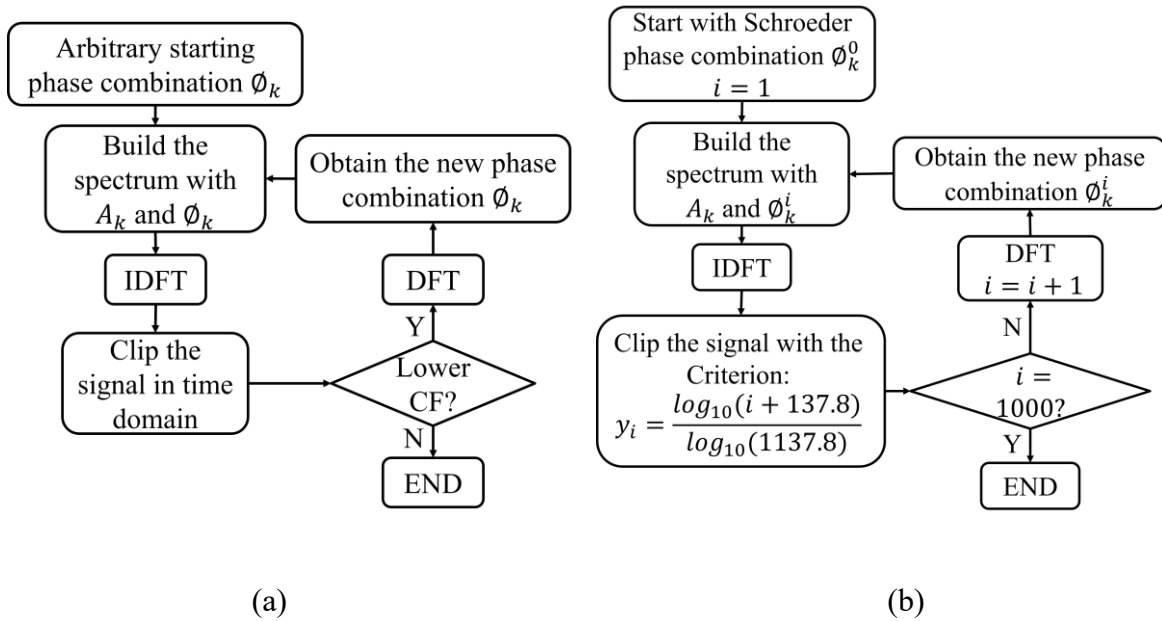


Figure 4.4 (a) Time-frequency domain swapping algorithm (b) Time-frequency domain swapping algorithm revised by Yang *et al.*

The minimization of CF remains an open mathematical problem [236], with various solutions proposed by researchers. Schroeder, in 1970, introduced the first analytical solution, determining the initial phases using a straightforward formula, as demonstrated in Equation (4.6) [237], where φ_n and p_l are the phase of the n th harmonic and its relative power to the l th harmonic of the prescribed power spectrum, respectively. Although this method is simple and easy to implement, its results are typically suboptimal and only marginally better than random selection. Van Der Ouderra *et al.* proposed an iterative time-frequency domain swapping (TFDS) algorithm to tackle the CF minimization problem [236, 238]. The algorithm starts with the desired amplitude spectrum a_k and a random phase combination φ_k , constructing the initial multi-tone signal using the inverse discrete Fourier transform (IDFT). The time-domain multi-tone signal is then clipped according to a specific criterion (75-95%), and a new phase combination φ_k is calculated using the discrete Fourier transform (DFT) with the clipped signal. This process repeats until the CF no longer decreases, as illustrated in Figure 4.4(a). The TFDS performance primarily depends on the clipping criterion selection, balancing convergence speed and optimization performance. Several studies have suggested methods for choosing the clipping criterion to expedite convergence and achieve minimized CF, with Yang *et al.*'s approach being one of the most efficient, as shown in Figure 4.4(b) [239]. Another efficient iterative algorithm employs the nonlinear Chebyshev approximation method (NCAM), proposed by Guillaume *et al.* [240]. In recent years, optimization algorithms have advanced and gained widespread application. Researchers have applied swarm intelligence algorithms such as the genetic algorithm (GA) [241] and the artificial bee colony (ABC) algorithm [242] to optimize CF. Although these swarm intelligence algorithms require more computational resources, their results have potential to surpass those of previous analytic methods and iterative algorithms.

$$\varphi_n = \varphi_1 - 2\pi \sum_{l=1}^{n-1} (n-l)p_l \quad n = 1, 2, \dots, N. \quad (4.6)$$

In the proposed system, the multi-tone signal is synthesized using the FPGA firmware and stored in the RAM for later use. The stored multi-tone signal data frame has a length of 4096, equal to the length of the sampled data frame, and a width of 14-bit, matching the width of the DAC. This results in a total on-chip memory usage of 7 kb. It is commonly believed that a higher update rate, achieved through a longer single frame length, can enhance the spurious-free dynamic range (SFDR) performance of the signal. However, our preliminary tests had shown that a multi-tone signal data frame length exceeding 4096 does not further improve measurement precision, so the length is set to 4096 to conserve memory resources.

Additionally, the same stored multi-tone signal can be output at different clock frequencies to adjust the excitation signal's spectrum. In the proposed system, impedance is measured with multi-tone signals once per decade frequency range. This allows the same stored multi-tone signal to be used repeatedly for excitation in the 10 Hz to 100 Hz and 100 Hz to 1000 Hz ranges by simply adjusting the output clock frequency by 10 times. Moreover, the stored multi-tone signal is expected to have a minimal CF to enhance the excitation signal's SNR. To achieve this, various methods were employed to synthesize the multi-tone signal on a computer, including the revised TFDS algorithm, NCAM, and some popular swarm intelligence algorithms. This approach facilitates an exploration of the most suitable algorithm for CF minimization.

4.3 Results and Discussion

4.3.1 Multi-tone Signal Synthesis

Two types of spectra were prepared to evaluate the performance of various CF minimization algorithms: (1) an equidistant and flat spectrum with a frequency list of (1, 2, 3, 4, 5, 6, 7, 8, 9), and (2) a quasi-logarithmic and flat spectrum with a frequency list of (1, 2, 3, 5, 7), where "1" represents the fundamental frequency. Due to inherent constraints in FFT-based measurements, achieving a true logarithmic spectrum is unattainable, as only integer multiples of the fundamental frequency can be computed. The CF minimization algorithms chosen for comparative analysis included the NCAM [240], Ojarand's Method [243], revised TFDS [239], Particle Swarm Optimization (PSO) [244], GA [241], ABC algorithm [242], and Bacterial Foraging Optimization (BFO) [245]. The BFO algorithms have not been previously employed in the context of CF minimization.

The two spectra were synthesized utilizing these algorithms within the Matlab R2020a software environment on a personal computer (CPU: AMD Ryzen 7 1700; GPU: NVIDIA GeForce GTX 1070). Each algorithm repeated 100 iterations, and their optimal results, mean results, least favorable results, and average time consumption are documented in Table IV. This comparative evaluation enables the determination of the most suitable algorithm for CF minimization in the proposed system.

The CF optimization results for both spectrums demonstrate that the revised TFDS method outperforms other algorithms in terms of optimization efficiency and time consumption. While the PSO algorithm exhibited superior optimization results in both spectral optimization experiments, the differences in outcomes were marginal compared to the revised TFDS (1.5665 vs. 1.5685 for the 5-frequency spectrum and 1.3976 vs. 1.3986 for the 9-frequency spectrum).

Furthermore, the optimization efficacy of the PSO algorithm is heavily reliant on random seeds, leading to an average optimization result inferior to that of the revised TFDS. The revised TFDS algorithm consistently achieves excellent optimization results, closely approximating the optimal results obtained from other algorithms, in a relatively short time frame (approximately 0.15 seconds). Moreover, the revised TFDS algorithm offers the extra advantage of reusing the FFT module on the FPGA, further accelerating the algorithm's execution speed. During testing, the FPGA completed the entire revised TFDS algorithm process in 0.132 seconds. This performance renders the revised TFDS algorithm a suitable choice for CF minimization in the proposed system.

Table IV Crest Factor Optimization Results Using Various Algorithms

5 Frequencies				
Algorithm	Best	Avg	Worst	Time (sec)
Ojarand	1.6395	1.6395	1.6395	0.3928
NCAM	1.5685	1.6026	1.7273	0.0443
Revised TFDS	1.5685	1.5685	1.5685	0.1441
PSO	1.5665	1.6006	1.6984	1.021
GA	1.5672	1.6269	1.758	1.1035
ABC	1.576	1.6108	1.6369	6.6386
BFO	1.6519	1.6815	1.7171	5.8682
9 Frequencies				
Algorithm	Best	Avg	Worst	Time (sec)
Ojarand	1.5467	1.5467	1.5467	0.8847
NCAM	1.4001	1.4748	1.5924	0.5258
Revised TFDS	1.3986	1.3986	1.3986	0.1506
PSO	1.3976	1.5229	1.7102	4.6366
GA	1.4083	1.5161	1.6325	8.899
ABC	1.4747	1.6182	1.6760	9.4156
BFO	1.6113	1.8656	2.2022	8.5665

4.3.2 Measurement Performance Evaluation

The EIS system was intended to be developed for use with the IDE chip described in Section 3.2.3. In practical applications, the impedance of the IDE chip loaded with biosamples spans from 200 Ω to 200 k Ω in the 10 Hz to 1 MHz frequency range. The 1 kHz to 1 MHz segment is of particular interest, corresponding to an impedance range of about 100 Ω to 3 k Ω . Impedance values outside this range are generally employed to assess whether the IDE chip is damaged or contaminated, thus they do not require high accuracy.

In order to evaluate the system's accuracy and precision across the 10 Hz to 1 MHz range, nine pure resistors varying from 100 Ω to 500 k Ω were employed. The true magnitude and phase values (Z_t , θ_t) of the resistors were established by averaging ten measurements obtained using the MFIA Impedance Analyzer (Zürich Instruments, Zürich, Switzerland). These true values were then compared to the average values from 200 measurements taken with the proposed EIS system. Equations (4.7) through (4.10) depict the evaluation of accuracy and precision for both magnitude and phase, with e_a and e_p representing the errors in terms of accuracy and precision, $\sigma_{Z_{200}}$ and $\overline{Z_{200}}$ denoting the standard deviation and average value of 200 measurement magnitude results, and $\sigma_{\theta_{200}}$ and $\overline{\theta_{200}}$ denoting the standard deviation and average value of 200 measurement phase results, respectively.

$$e_a(Mag) = \frac{|\overline{Z_{200}} - Z_t|}{Z_t} \times 100\% \quad (4.7)$$

$$e_p(Mag) = \frac{\sigma_{Z_{200}}}{\overline{Z_{200}}} \times 100\% \quad (4.8)$$

$$e_a(Pha) = |\overline{\theta_{200}} - \theta_t| \quad (4.9)$$

$$e_p(Pha) = \sigma_{\theta_{200}} \quad (4.10)$$

Table V Evaluation of Accuracy and Precision for the Proposed EIS System Using Resistors.

Magnitude Errors						
Fre(Hz) Res(Ω) ϵ_a ϵ_p	10	100	1 k	10 k	100 k	1 M
91.23	0.418% 0.175%	0.024% 0.216%	0.112% 0.021%	0.299% 0.066%	0.329% 0.022%	0.199% 0.098%
329.78	0.125% 0.037%	0.021% 0.025%	0.111% 0.019%	0.004% 0.006%	0.108% 0.005%	0.217% 0.007%
1001.3	0.402% 0.125%	0.342% 0.117%	0.239% 0.029%	0.228% 0.014%	0.237% 0.012%	0.164% 0.016%
3644.88	0.265% 0.338%	0.158% 0.518%	0.192% 0.088%	0.218% 0.050%	0.417% 0.077%	0.472% 0.067%
11.94 k	0.358% 0.237%	0.232% 0.319%	0.057% 0.105%	0.362% 0.090%	0.593% 0.077%	0.023% 0.079%
36.13 k	0.044% 0.596%	0.179% 0.383%	0.134% 0.177%	0.234% 0.056%	0.300% 0.212%	0.517% 0.0239%
89.32 k	0.329% 0.998%	0.736% 0.924%	0.746% 0.456%	0.538% 0.179%	0.036% 0.481%	0.871% 0.393%
212.26 k	0.628% 1.809%	0.604% 1.941%	0.664% 0.907%	0.435% 0.484%	0.451% 1.130%	1.203% 0.828%
498.83 k	0.409% 3.125%	0.399% 2.620%	0.505% 1.676%	0.209% 0.936%	0.274% 1.609%	2.024% 1.260%
Phase Errors						
Fre(Hz) Res(Ω) ϵ_a ϵ_p	10	100	1 k	10 k	100 k	1 M
91.23	0.095° 0.024°	0.011° 0.012°	0.019° 0.008°	0.032° 0.004°	0.160° 0.004°	0.262° 0.007°
329.78	0.103° 0.032°	0.014° 0.012°	0.014° 0.012°	0.136° 0.005°	0.490° 0.006°	0.001° 0.007°

1001.3	0.104° 0.096°	0.018° 0.134°	0.016° 0.027°	0.093° 0.018°	0.475° 0.012°	0.333° 0.014°
3644.88	0.085° 0.331°	0.067° 0.588°	0.033° 0.072°	0.254° 0.044°	0.334° 0.075°	0.384° 0.089°
11.94 k	0.117° 0.156°	0.161° 0.197°	0.042° 0.044°	0.047° 0.024°	0.323° 0.101°	0.057° 0.065°
36.13 k	0.151° 0.307°	0.163° 0.221°	0.045° 0.145°	0.059° 0.062°	0.362° 0.234°	0.208° 0.242°
89.32 k	0.141° 0.362°	0.204° 0.435°	0.055° 0.263°	0.126° 0.157°	0.479° 0.462°	1.074° 0.279°
212.26 k	0.084° 0.468°	0.208° 1.049°	0.096° 0.654°	0.092° 0.252°	0.928° 0.967°	1.800° 0.601°
498.83 k	0.166° 1.283°	0.220° 1.396°	0.295° 1.090°	0.226° 0.746°	0.690° 1.872°	3.241° 1.393°

Table V presents comprehensive accuracy and precision evaluation results with different resistors. By employing a 1% error as the screening standard for instrument accuracy and precision, the available measurement range of the proposed system is 10 Hz to 1 MHz and 100 Ω to 90 k Ω . Furthermore, for the impedance and frequency range of interest (100 Ω to 3 k Ω and 1 kHz to 1 MHz), the errors in terms of accuracy and precision were less than 0.5% and 0.1%, respectively.

In the second phase of the evaluation, an IDE chip loaded with 60 μ L of 10 μ M/L PBS solution was prepared as the subject for measuring impedance. This test aimed to assess the accuracy and precision of the proposed EIS system in comparison to the MFIA Impedance Analyzer. Both the MFIA and the proposed system were used to measure the impedance of the IDE chip in rapid succession, with the MFIA's results being considered as the true values. Here, the measurements using the proposed system were repeated 20 times. The evaluation of the proposed system's accuracy and precision was conducted using Equations (4.7) to (4.10), and the overall results of this comparison are illustrated in Figure 4.5. When plotted on a logarithmic

coordinate system, the impedance measurements obtained from the MFIA and the proposed system exhibited highly similar magnitude and phase curves, indicating a strong consistency between the two sets of results.

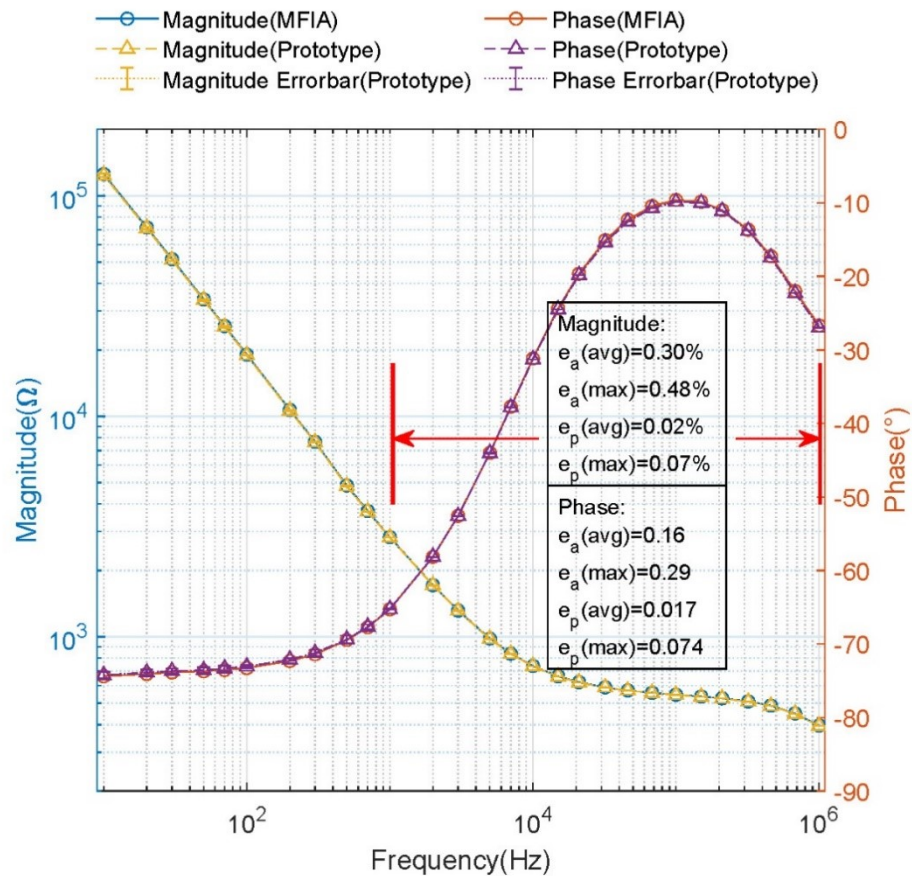


Figure 4.5 Performance Assessment of the Proposed EIS System with an IDE Chip Immersed in PBS Solution (reproduced from [201]).

In the critical frequency range spanning from 1 kHz to 1 MHz, the proposed system demonstrated an average magnitude accuracy error of 0.30%, an average magnitude precision error of 0.02%, an average phase accuracy error of 0.16, and an average phase precision error of 0.017. These results present the system's ability to provide accurate and precise impedance data

within the critical frequency range. Moreover, the proposed system is also rapid in the measurement, requiring just 0.46 seconds to scan 28 frequency points in a quasi-logarithmic distribution that ranged from 10 Hz to 1 MHz. This speed offers a significant advantage in various practical applications where rapid measurements are essential. Table VI presents a comparison of the proposed EIS system's specifications with those of other EIS systems, including those proposed by Jiang et al. [177], Ruiz-Vargas et al. [224], the RedPitaya-based EIS system, and the MFIA Impedance Analyzer.

Table VI Comparison of Specifications

Device	This work	Jiang	Ruiz-Vargas	RedPitaya	MFIA
Measurement speed	1.1 ms	24.2 ms	70 ms	70 ms	20 ms
Measurement error	0.24%	0.30%	0.70%	2%	0.05%
Frequency Range	10 Hz - 2 MHz	100 Hz - 500 kHz	10 Hz - 1 MHz	10 Hz - 1 MHz	1 mHz - 5MHz
Impedance Range	100 Ω - 200 k Ω	10 Ω - 100 k Ω	1 Ω - 10 k Ω	1 Ω - 10 k Ω	0.1 Ω - 10 G Ω
Excitation Amplitude	0.01-3 V	5 V	1 V	1 V	0-3 V
Size	163·84·30 mm ³	116·100·89 mm ³	140·90·30 mm ³	110·60·28 mm ³	283·232·102 mm ³
Weigh	0.25 kg	0.45 kg	N/A	0.1 kg	3.8 kg
Cost in USD	95	45	N/A	400	9000

* The measurement speed and error data are for the measurement of 1 k at 1 kHz.

** The impedance range refers to the valid impedance range with an error < 1%.

4.4 Conclusion

In this study, we developed a portable, low-cost EIS system tailored for POC applications, which exhibits excellent accuracy and precision in biosample measurements. The EIS system ensures both measurement speed and accuracy by implementing low CF multi-tone signal synthesis and data averaging modules at low frequencies (below 1 kHz) while utilizing single-

tone signals at high frequencies (above 1 kHz). Regarding the measurement speed, the system can scan 28 quasi-logarithmically distributed frequency points ranging from 10 Hz to 1 MHz in a mere 0.46 seconds. Moreover, the proposed EIS system supports simultaneous EIS for eight channels of IDE chips, further enhancing measurement efficiency. Within the critical frequency range of 1 kHz to 1 MHz, the system demonstrates an average magnitude accuracy error of 0.30%, an average magnitude precision error of 0.02%, an average phase accuracy error of 0.16, and an average phase precision error of 0.017, all achieved with a low excitation amplitude of 10 mV. This low excitation amplitude offers several advantages, including protection of the electrodes and biosamples, preservation of impedance linearity, and minimization of thermal effects. Given its high precision and biosafety features, the proposed EIS system holds significant potential for widespread use in various biomarker measurement applications.

5. A Low-Intensity Pulsed Ultrasound Interface ASIC Chip for Miniaturized Medical Therapeutic Device Applications

The content of this chapter has been submitted as a manuscript for review to IEEE Transactions on Very Large Scale Integration Systems as "A Low-Intensity Pulsed Ultrasound Interface ASIC Chip for Wearable Medical Therapeutic Device Applications" by Xuanjie Ye, Xiaoxue Jiang, Shuren Wang, and Jie Chen.

5.1 Introduction

With a wide range of applications, including surgical procedures, diagnostics, and therapy, ultrasound technology has played a critical role in the medical field for almost a century [61, 246, 247]. In its early stages, the primary focus of ultrasound centered on the thermal effects of high-intensity ultrasound waves that can selectively elevate the temperature of target tissues. This technique has demonstrated its efficacy in various medical interventions. Recent advances in the field have shifted attention toward low-intensity ultrasound, which operates without generating thermal effects [62, 65, 248]. This innovative approach has paved the way for various therapeutic applications, revolutionizing the medical field. For instance, low-intensity ultrasound has been employed to facilitate the healing of fractures, a technique that significantly promotes the recovery process [62, 79, 249]. Furthermore, this technology has also proven to be a promising assist treatment for cancer therapy [65, 84, 118, 250], offering a non-invasive treatment option that mitigates the adverse side effects often associated with traditional chemotherapy and radiation. Another notable application of low-intensity ultrasound is neuromodulation [63, 251, 252], where it has been utilized to modulate neural activity and alleviate symptoms in patients suffering from neurological disorders. Moreover, low-intensity

ultrasound has shown the potential in promoting peripheral nerve regeneration [64, 253]. Low-intensity ultrasound technology has expanded the scope of medical applications far beyond its original thermal-based therapeutic effect.

LIPUS is a distinctive subset of low-intensity ultrasound technology, characterized by its delivery of ultrasound energy as pulse waves. This unique attribute enables LIPUS to concentrate energy within the pulse, thereby maintaining non-thermal properties while delivering sufficient ultrasound amplitude to the target [254]. Empirical evidence has demonstrated the therapeutic efficacy of LIPUS across various tissues, including knee osteoarthritis [255], tooth root resorption [256], inflammation inhibition [257], and bone fractures [258]. A widely employed LIPUS parameter set, featuring a 1.5 MHz fundamental frequency, 200 μ s pulse width, 1 kHz repetition rate (corresponding to a 20% duty cycle), and a spatial average temporal average (SATA) intensity of 30 mW/cm², has been successfully applied to the fracture healing scenarios [91, 258-260]. The U.S. FDA and the U.K. National Institute for Health and Care Excellence (NICE) have approved these applications for their effectiveness in promoting fracture healing. This LIPUS parameter set has also been utilized for intra-oral dental tissue formation as well as stem cell growth and differentiation [261, 262]. Furthermore, Health Canada approved the Aveo system, an orthodontic treatment device based on LIPUS, in 2016. In summary, LIPUS has emerged as a versatile and powerful tool within the medical field, offering transformative therapeutic potential across diverse applications.

This project endeavors to develop a miniaturized LIPUS interface ASIC chip, designed for a wearable ultrasonic therapy system that can output LIPUS with an average power intensity of 30 mW/cm² or 50 mW/cm² with a duty cycle of 20%. These LIPUS parameters have been widely used in the therapeutic applications [256, 263]. Typically, wearable devices rely on low-

voltage power sources like batteries. However, driving an ultrasound transducer demands a voltage exceeding that of a standard battery or portable DC power supply, necessitating the implementation of a DC-DC boost voltage converter. Considering that the electromechanical conversion efficiency of most ultrasound transducers falls within the range of 30% to 35% [264-266], the DC-DC boost voltage converter must be capable of delivering a continuous power output of 500 mW to support a LIPUS transducer with a 1 cm diameter, a SATA intensity of 30 mW/cm², and a duty cycle of 20%. Inductor-based boost converters can meet these power requirements, but they are bulky and not suitable for miniaturized devices. Furthermore, many ultrasound treatments necessitate MRI guidance for precise application [267-269], rendering inductors incompatible with the MRI environment. Consequently, the proposed system employs a charge pump as an alternative solution, also known as a switched-capacitor DC-DC converter. This alternative approach addresses the challenges of miniaturization while maintaining compatibility with MRI-guided treatments, thereby advancing the development of wearable ultrasonic therapy systems.

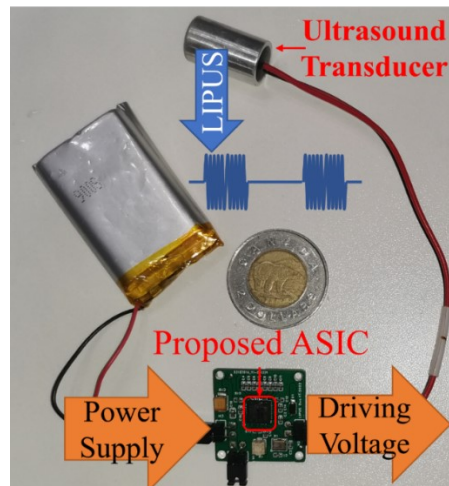


Figure 5.1 Comparison of the Highly Integrated LIPUS System with a Canadian Two-Dollar Coin.

This chapter introduces a novel LIPUS interface chip created for a highly integrated ultrasound driver system, which can be used in portable medical therapy devices. The chip was carefully designed and made using the AMS 0.35- μm High-Voltage Complementary Metal-Oxide-Semiconductor (CMOS) Process Technology (H35B4D3). The proposed chip needs only a small number of passive electronic components to build the peripheral circuit, simplifying the overall system. With a properly designed peripheral circuit, the chip can provide up to 181.5 mW to the ultrasound transducer when powered by a 5-V supply, or 103.3 mW with a 3.7-V power supply. Figure 5.1 shows the proposed ASIC chip, its peripheral circuit, and how it can be included in the ultrasound therapy system.

5.2 System Design

The system architecture for the proposed ASIC chip and its peripheral components is depicted in Figure 5.2. The power supply of the system can accommodate either 3.7 V or 5 V, with the power source connected simultaneously to digital power supplies (DV_{DD}), analog power supplies (AV_{DD}), and power management power supplies (PV_{DD}). The digital circuit block governs all digital signals within the system, primarily for generating suitable clock signals for other modules. These clock signals originate from an off-chip 12-MHz crystal oscillator and an on-chip voltage-controlled oscillator (VCO). The VCO-derived clock signal controls the charge pump, and clock drivers are implemented to enable the clock to drive the large MOSFETs in the charge pump. Consequently, the control voltage V_C can adjust the output high voltage from the charge pump V_{PP} , which in turn powers the transducer driver. The transducer driver consists of two high-voltage NMOSs operating as a half-bridge (HB) driver. These NMOSs occupy large on-chip space to achieve low on-resistances, requiring gate drivers for their large gates. Furthermore, the upper half-bridge driver necessitates a high-voltage level shifter (HVLS) and an

external bootstrap circuit, comprising a capacitor C_{BOOT} and a diode D_{BOOT} , to ensure it remains in normal operation condition when the source voltage increases.

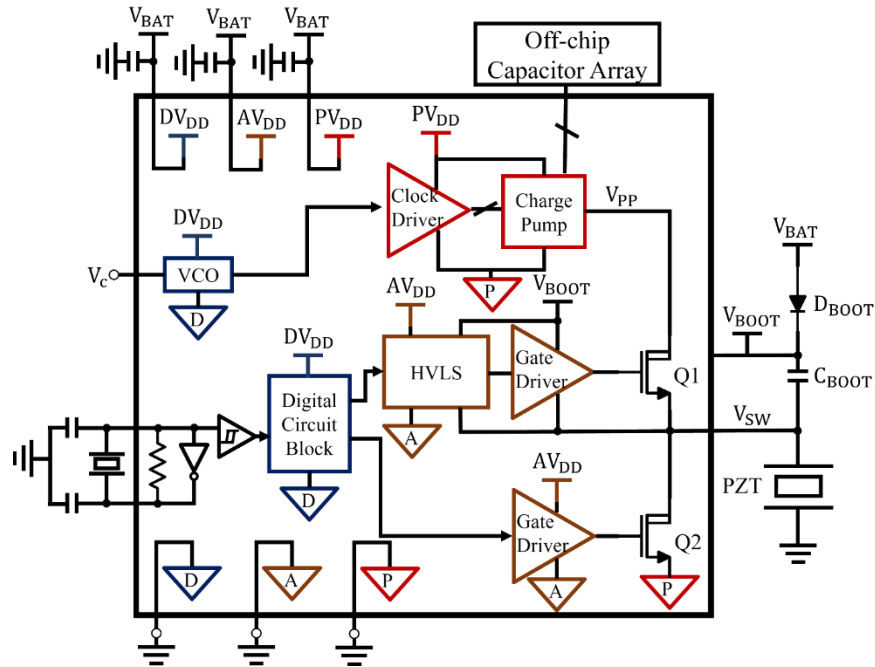
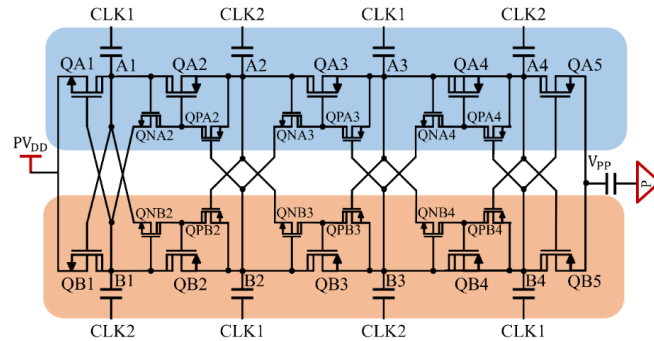


Figure 5.2 Proposed ASIC Chip System Architecture and Associated Peripheral Components.

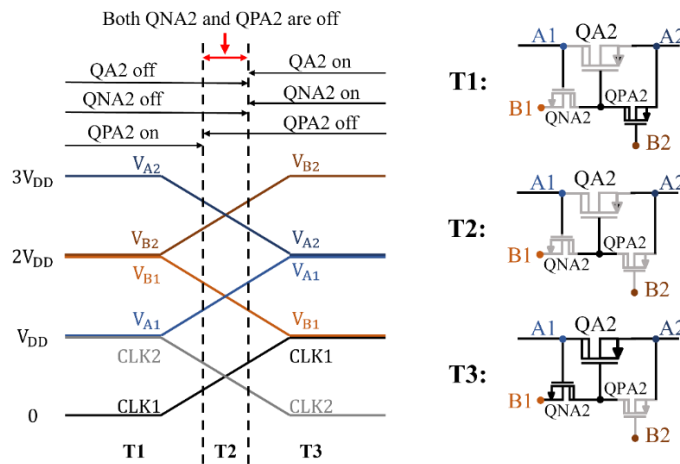
5.2.1 Charge Pump

The proposed LIPUS system requires a DC-DC boost converter to elevate the battery power voltage to a level capable of driving the ultrasound transducer. To address the challenges of miniaturization and MRI compatibility, the charge pump was chosen as the DC-DC boost converter for the system. Figure 5.3(a) demonstrates the design of the 4-stage charge pump, which is based on the CP-1 topology, which was proposed by our research group as described in [270]. High-voltage (HV) devices provided by the AMS 0.35- μm High-Voltage CMOS Process Technology (H35B4D3) were employed in this charge pump topology, allowing the MOSFETs to endure a higher drain-source voltage compared to the standard CMOS process. This feature

enables each stage of the charge pump to be boosted to a higher voltage without the risk of breakdown, requiring only four stages to attain the required driving voltage (approximately 12-20 V). This design ensures a more efficient and compact solution while maintaining compatibility with MRI environments.



(a)



(b)

Figure 5.3 (a) 4-stage charge pump topology. (b) Operation timing of a typical unit CTS MA2.

The 4-stage charge pump consists of two symmetrical branches, each operating with complementary clocks. These branches contain charge transfer switches (CTSs) and gate-control

transistors. Using branch A as an example, QA1, QA2, QA3, QA4, and QA5 serve as CTSs, transferring charges to subsequent stages. QNA2, QPA2, QNA3, QPA3, QNA4, and QPA4 act as gate-control transistors, regulating the conduction of their corresponding CTSs. The two out-of-phase clocks, CLK1 and CLK2, have a high voltage level of PV_{DD} and a low voltage level of the ground. In phase 1, when CLK1 is high and CLK2 is low, QA2, QA4, QB1, QB3, and QB5 turn on, while other CTSs turn off. This leads to charge transfer from A1 to A2, A3 to A4, PV_{DD} to B1, B2 to B3, and B4 to V_{PP} . In phase 2, when CLK1 is low and CLK2 is high, MA1, MA3, MB2, MB4, and MA5 turn on, and the other CTSs turn off. As a consequence, charges move from PV_{DD} to A1, A2 to A3, B1 to B2, B3 to B4, and A4 to V_{PP} . This design efficiently and effectively manages charge transfer in the 4-stage charge pump.

Using QA2 and its gate-control transistors QNA2 and QPA2 as examples, as depicted in Figure 5.3(b), we will introduce the operation of the charge pump. In phase T1, when CLK1 is low and CLK2 is high, QNA2 turns off as $V_{gs}(QNA2) = V_{A1} - V_{B1} = -V_{DD}$, and QPA2 turns on due to $V_{gs}(QPA2) = V_{B2} - V_{A2} = -V_{DD}$. As a result, CTS QA2 is turned off, with its source A2 connected to its gate B2 ($V_{gs}(QA2) = 0$). In the clock transition, CLK1 goes up while CLK2 goes down. When $V_{gs}(QPA2) = V_{B2} - V_{A2} > -V_{th}$, QPA2 is turned off, initiating phase T2. In phase T2, all transistors, including QA2, QNA2, and QPA2, are turned off. At the end of phase T2 and the beginning of phase T3, QNA2 turns on as $V_{gs}(QNA2) = V_{A1} - V_{B1} > V_{th}$. Consequently, QA2 is turned on since $V_{gs}(QA2) = V_{B1} - V_{A2} = -V_{DD}$. This dedicated design eliminates reverse charge flow, as all transistors are turned off during T2. Furthermore, the high-voltage MOSFET transistors employed in this charge pump design need to withstand a maximum drain-source voltage of $2V_{DD}$. The clock driver's power supply should be below 2.5 V or 1.65 V when using standard MOSFETs, which have a lower voltage tolerance of 5 V or 3.3 V. However, by

employing high-voltage MOSFET transistors, a conventional 3.7-V lithium battery or a 5-V USB power supply can power the clock driver. Additionally, this design enables each charge pump stage to boost a higher voltage, thereby reducing the number of required stages.

5.2.2 High Voltage Level Shifter

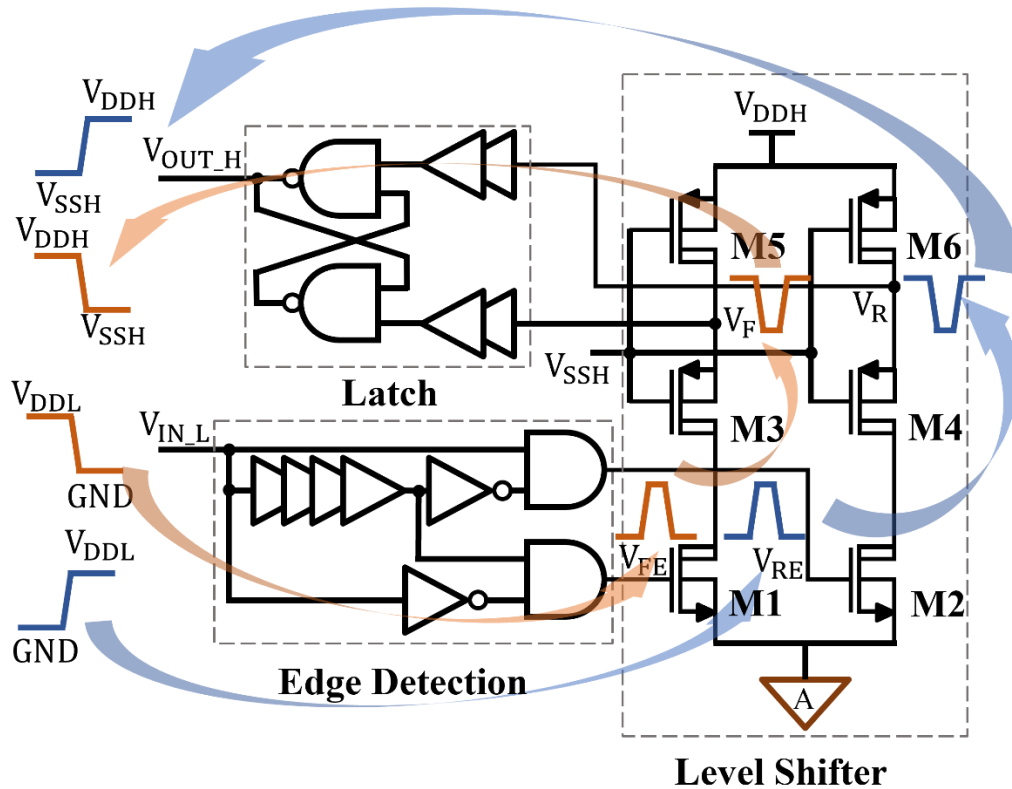


Figure 5.4 Schematic representation of the HVLS and explanation of its functioning.

The HVLS is an essential module in the proposed system, as it enables the high-side NMOS of the HB driver to turn on. The primary function of the HVLS is to convert the logic signals between different voltage domains, with the critical performance indexes being propagation delay and power dissipation. Additionally, the size of the HVLS impacts the overall chip cost and must be considered. Therefore, the pulse-triggering HVLS approach proposed in [271] has been adopted for this system.

Figure 5.4 illustrates the complete circuit diagram of the HVLS, which consists of an edge detection module, a level shifter, and a latch. The edge detection module generates a pulse at either V_{RE} or V_{FE} upon detecting a rising or falling edge in the input signal V_{INL} . The level shifter then inverts and raises the pulse from the low-voltage domain to the high-voltage domain. The resulting notching signal at V_R or V_F alters the latch's state, switching V_{OUTH} between V_{BOOT} (high) and V_{SW} (low) levels. In the steady state, all voltage levels remain stable, since the output is latched.

To illustrate the operation of the level shifter in detail, let us consider the example of a rising edge. As V_{INL} transitions from low to high, a pulse is generated at V_{RE} , while V_{FE} maintains its low voltage level. Consequently, transistors M1, M3, and M5 remain in their current state, whereas the pulse at V_{RE} triggers voltage changes in transistors M2, M4, and M6. The pulse at V_{RE} momentarily turns on M2, causing the drain terminal of M4 to be pulled down to ground level during this short period. Subsequently, V_R is pulled down to $(V_{SW} + V_{th})$, generating a notch at V_R . This notch flips the state of the latch, and V_{OUTH} is subsequently latched at the high voltage level V_{BOOT} .

In the stable state, the voltage levels at V_F and V_R are maintained at V_{BOOT} because transistors M5 and M6 are turned on ($V_{gs} = V_{SW} - V_{BOOT} = -V_{DD}$). Similarly, M3 and M4 are also turned on, while M1 and M2 are turned off since V_{FE} and V_{RE} remain at ground level. As a result, the drain terminals of M3 and M4 are held at V_{BOOT} . When a signal transition occurs at V_{INL} , the signal propagates through the modules to V_{OUTH} .

5.2.3 Voltage-Controlled Oscillator

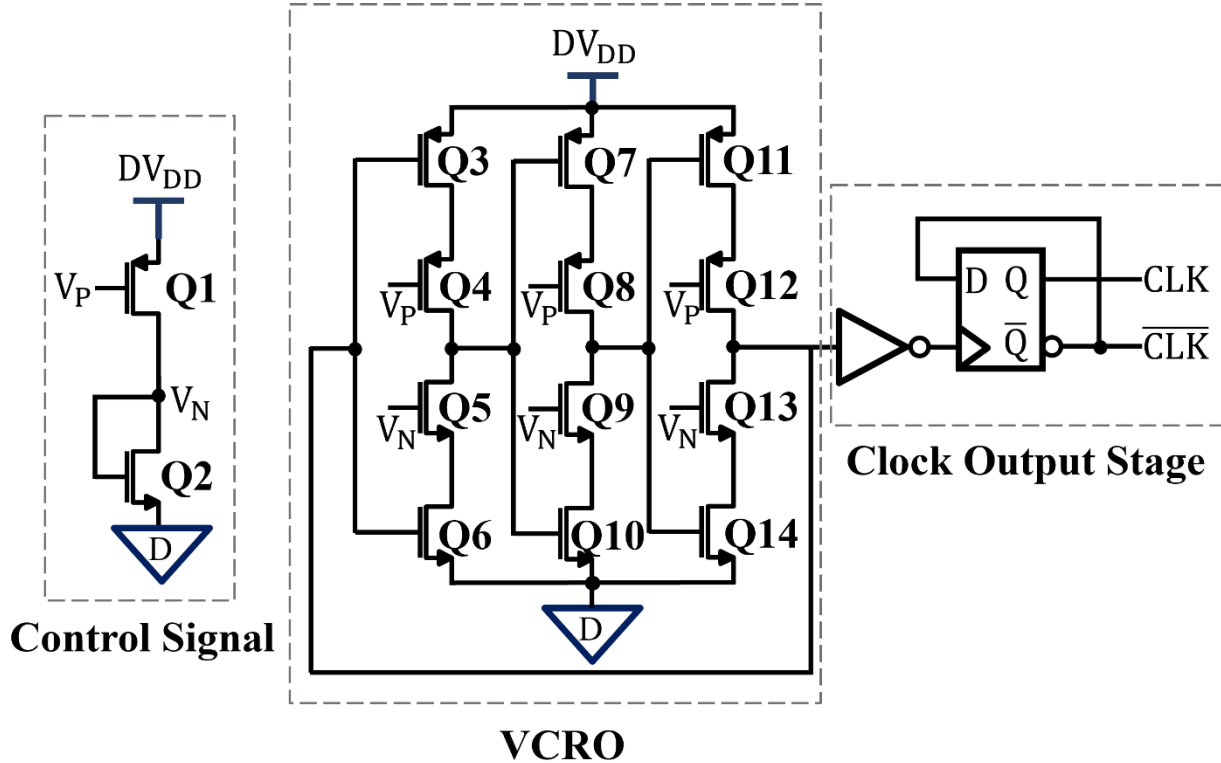


Figure 5.5 Circuit diagram of the 3-stage CSVCRO

A 3-stage current-starved voltage-controlled ring oscillator (CSVCRO) was employed to generate an adjustable-frequency clock for the charge pump module. By permitting the adjustment of the clock frequency, the power output capability of the charge pump can be customized to meet the specific demands of the application. The CSVCRO topology was selected for its low power consumption, extensive frequency range, and high integration capacity [272]. The CSVCRO adjusts frequency by controlling the current used to charge or discharge the load capacitance, which is modulated by the on-resistances of the pull-down and pull-up transistors. Lower on-resistances enable a larger current to charge or discharge the load capacitance, resulting in a higher frequency, and vice versa.

Figure 5.5 illustrates the circuit diagram of the 3-stage CSVCCRO module, which consists of a complementary control signal generator, a CSVCCRO core, and a clock output stage. The complementary control signal generator employs a current mirror topology to ensure similar currents flow through Q1 and Q2. Transistors Q4, Q8, and Q12 restrict the pull-up current flow, while Q5, Q9, and Q13 limit the pull-down current flow. In this manner, the complementary control signal V_N makes the current limiting capacity of Q4, Q8, and Q12 highly similar to that of Q6, Q10, and Q14, which are directly controlled by the input control voltage V_P . The 3-stage CSVCCRO core comprises transistors Q3-Q14, forming three inverters. The current flows of these three inverters are limited by current sources and sinks controlled by V_P and V_N , respectively. The output clock signal is buffered by an inverter and then passed to a flip-flop to produce a precise 50% duty cycle as well as narrow the rising and falling edges of the clock signal, making it a square wave. Simultaneously, an out-of-phase clock signal is generated, which is necessary for the charge pump module.

5.2.4 Half-bridge Driver

The output driver of the system employs an HB topology, which is implemented with two high drain-source breakdown voltage NMOS transistors. NMOS transistors are preferred for the high side of the HB, as they exhibit superior conducting properties and switching speed in comparison to the PMOS transistors of the same size. However, for the high-side NMOS to remain turned on, it requires a gate-source voltage (V_{GS}) that satisfies $V_{GS} = V_G - V_{SW} > V_{th}$, where V_{th} is the threshold voltage. To fulfill this condition, a combination of a bootstrap circuit and an HVLS circuit is utilized to elevate the gate voltage (V_G) of the high-side NMOS to $V_G = V_{BOOT} = V_{SW} + V_{DD}$. The bootstrap circuit ensures that the gate voltage is to generate a voltage

of $V_{BOOT} = V_{SW} + V_{DD}$, while the HVLS circuit is responsible for translating the logic signals between different voltage domains to facilitate the proper functioning of the high-side NMOS.

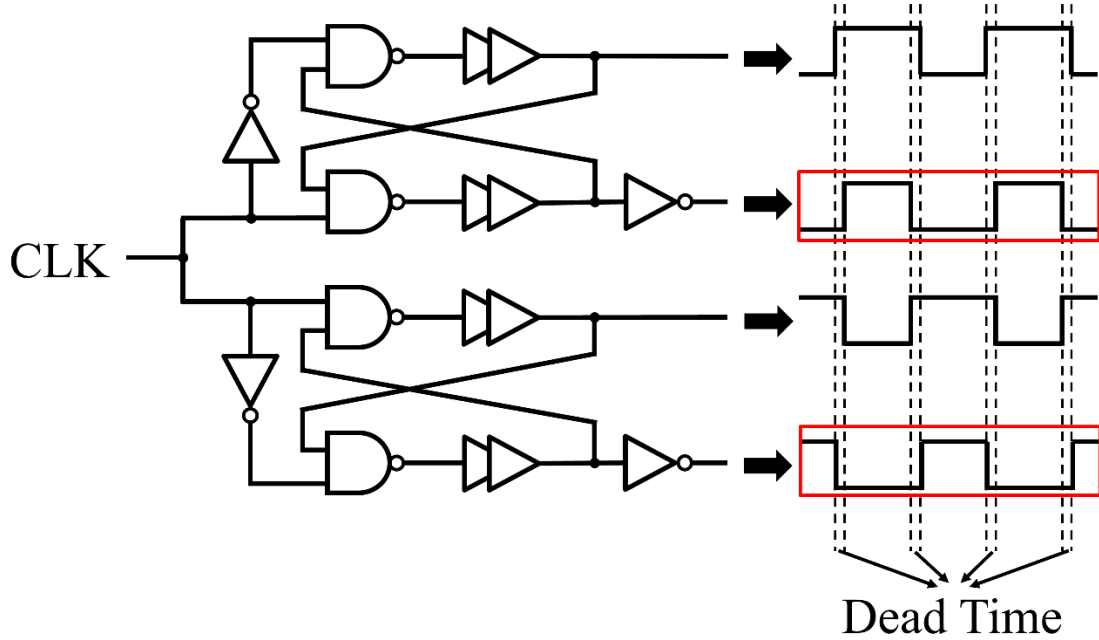


Figure 5.6 Schematic of the dead time generator and its corresponding waveform illustrating the generated timing intervals.

The on-resistance of the output switches is set to 3.1 ohms, based on a careful balance among conduction power loss, switching power loss, and the required chip area. These switches, designed with a large area ($W/L = 10000 \mu\text{m} / 0.5 \mu\text{m}$), introduce two significant challenges. First, the large-area NMOS gate possesses substantial parasitic capacitance, which demands a multi-stage gate driver to facilitate rapid turn-on and turn-off processes. To accomplish this, a series of four cascaded inverters are implemented, with sizes increasing in a geometric progression, ensuring swift and efficient transitions between the on and off states [273]. Second, to avoid the risk of two NMOS transistors turning on concurrently and resulting in a short circuit between VPP and GND, a dead-time generator is incorporated into the design. The circuit

topology and corresponding output waveform of this generator are depicted in Figure 5.6. The dead-time generator introduces a short interval during the turn-on alternation of the two NMOS transistors, allowing both to fully turn off and effectively preventing simultaneous conduction. This design feature ensures the protection of the system from potential short-circuit incidents.

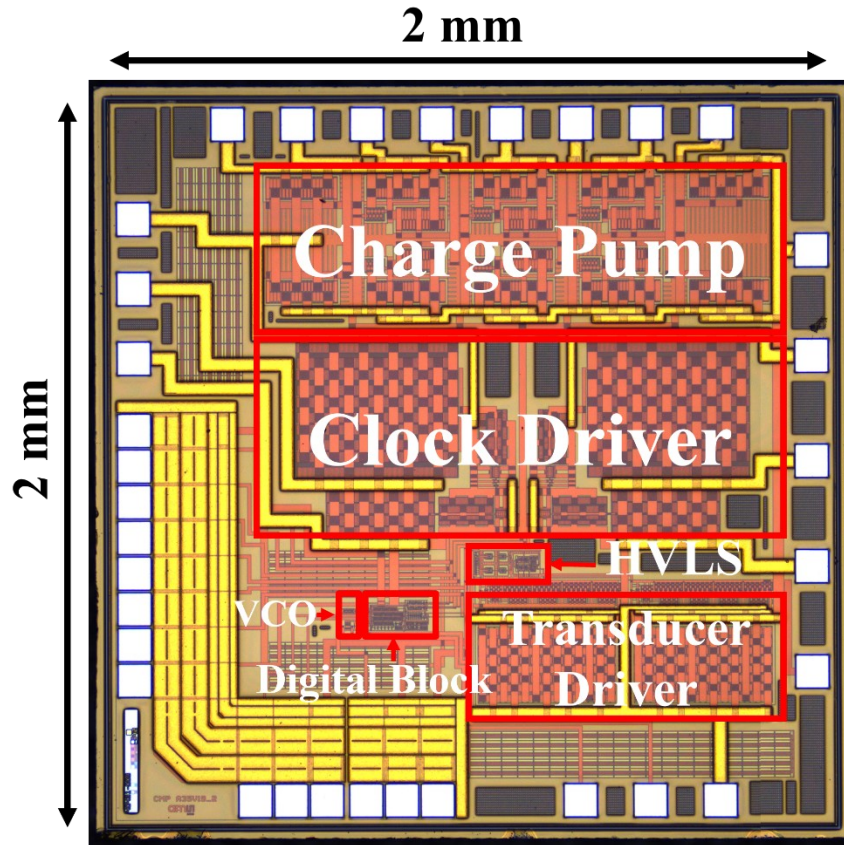


Figure 5.7 Micrograph of the bare die and its brief floor plan

5.3 Results and Discussion

Before tape-out, the proposed ASIC chip was verified in simulation using Cadence IC 6.1.5 Spectre Circuit Simulator (CA, United States) with the AMS 0.35- μm High-Voltage CMOS Process Technology (H35B4D3, HIT-kit v4.10) library. Post-layout simulations were carried out with the power supply configured at the standard lithium battery voltage of 3.7 V or

the USB voltage of 5 V. The bare die and its floor plan, displayed in Figure 5.7, occupy an area of 4 mm², inclusive of pads. The transistor parameters for the proposed design are detailed in Table VII. The capacitor array consists of capacitors with a capacitance value of 4.7 nF in both simulation and the test.

Table VII Transistor parameters of different modules in the system

Transistors in Charge Pump	Type	W/L ($\mu\text{m}/\mu\text{m}$)
QA1, QB1	20 V HVNMOS	2200/0.5
QA2-5, QB2-5	20 V HVPMOS	2700/1
QNA2-4, QNB2-4	20 V HVNMOS	300/0.5
QPA2-4, QPB2-4	20 V HVPMOS	1800/1
Transistors in HVLS	Type	W/L ($\mu\text{m}/\mu\text{m}$)
M1, M2	50 V HVNMOS	10/0.5
M3, M4	50 V HVPMOS	10/1
M5, M6	5 V PMOS	0.5/0.5
Transistors in CSVCRO	Type	W/L ($\mu\text{m}/\mu\text{m}$)
Q1	5 V PMOS	1.2/1
Q2	5 V NMOS	0.6/1
Q3, Q7, Q11	5 V PMOS	6/0.5
Q4, Q8, Q12	5 V PMOS	9/0.5
Q5, Q9, Q13	5 V NMOS	4.5/0.5
Q6, Q10, Q14	5 V NMOS	3/0.5
Transistors in HB	Type	W/L ($\mu\text{m}/\mu\text{m}$)
Q1, Q2	50 V HVNMOS	10000/0.5

5.3.1 Simulation Results

(A) Charge Pump

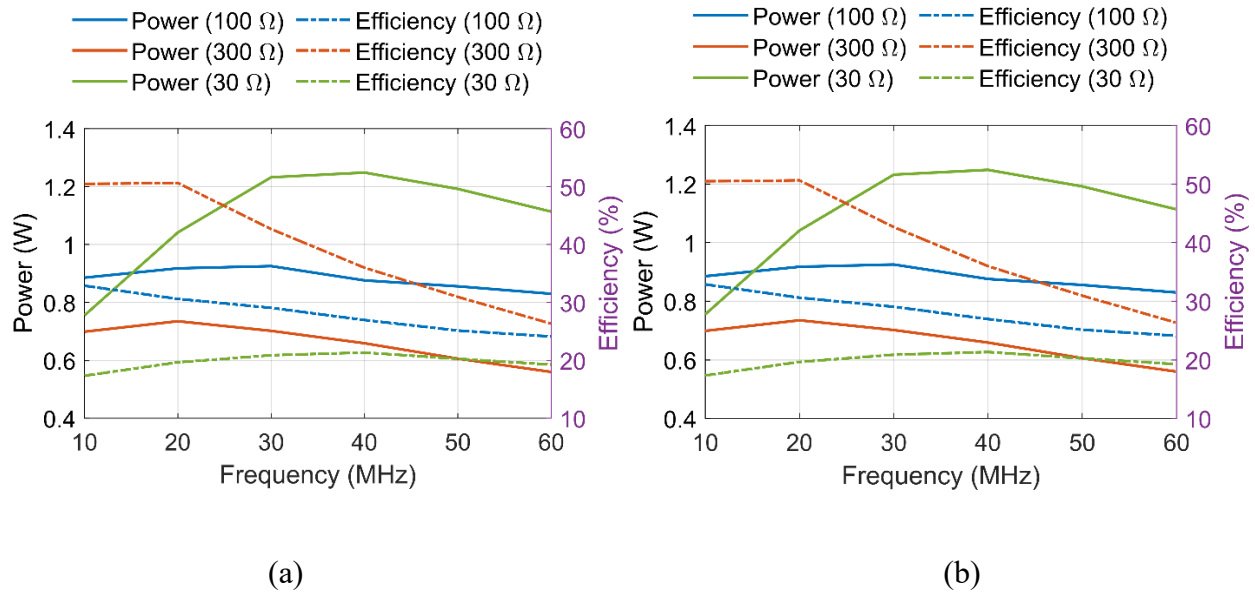


Figure 5.8 Post-layout simulation results of the charge pump under varying loads and clock frequencies: (a) Output power and efficiency comparison; (b) Ripple voltage and startup time comparison.

In order to evaluate the performance of the charge pump module under various continuous current delivery scenarios, simulations were conducted with different resistance loads (30 Ω, 100 Ω, 300 Ω) and frequencies (10-60 MHz). These simulations aimed to provide a deeper understanding of the module's behavior under diverse conditions. The outcomes of the simulations, which include output power, efficiency, ripple voltage, and startup time, are illustrated in Figure 5.8(a) and Figure 5.8(b). Startup time, a critical parameter for the charge pump's performance, is defined as the duration required to achieve 90% of the final output voltage. The results reveal that the power conversion efficiency experiences a decline as the load intensifies. The control frequency plays an important role in power conversion efficiency as well, with the peak efficiency generally observed at or near the frequency corresponding to maximum power generation. Additionally, the optimal control frequency is related to the resistance load, as

increased control frequencies are needed to reach the highest output power under heavier loads. It is also noted that ripple diminishes with the rise in control frequency. The charge pump's startup typically occurs in under 3 μs , taking approximately 1 μs for 30 Ω and 100 Ω loads. This swift startup time demonstrates the charge pump module's ability to quickly respond to varying operational demands.

(B) High Voltage Level Shifter

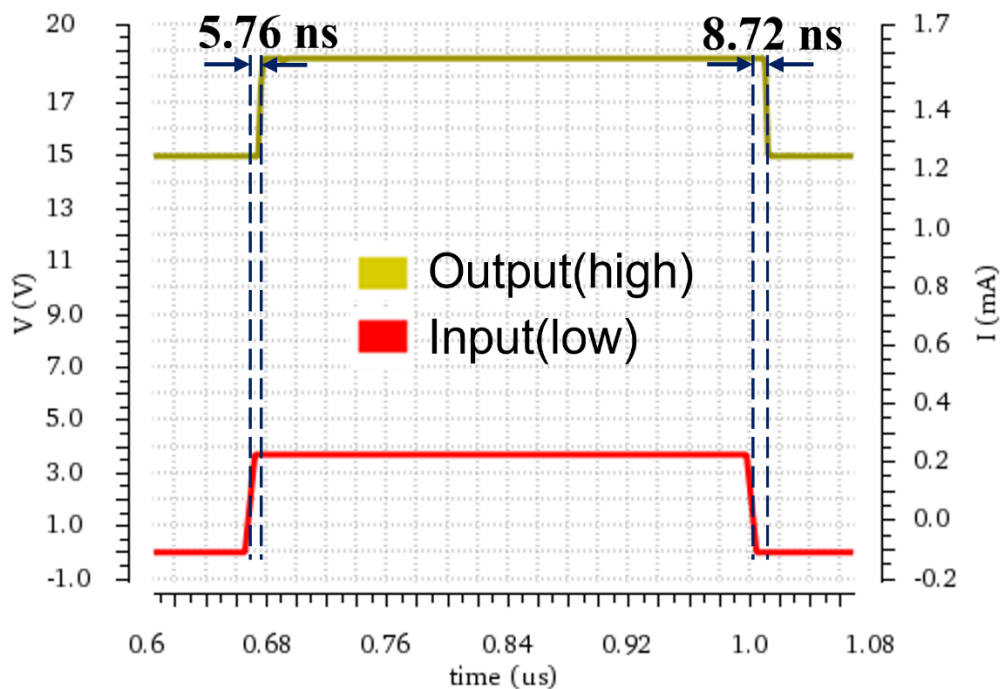


Figure 5.9 Post-layout transient simulation result of the HVLS.

In the post-layout simulation of the HVLS, a 1.5-MHz clock signal was utilized as the input, aligning with the application scenario of driving a 1.5-MHz square wave. The power supply voltages V_{DDL} , V_{DDH} , and V_{SSH} were configured with values of 3.7 V, 18.7 V, and 15 V, respectively. This setup results in a level shift from the low voltage domain (0-3.7 V) to the high voltage domain (15-18.7 V). As illustrated in Figure 5.9, the simulation result showcases

the rising and falling edges of the output waveform. The rising edge displays a delay of 5.76 ns, while the falling edge exhibits a delay of 8.72 ns. When examining the energy consumption, the rising edge necessitates 54.97 pJ, and the falling edge requires 55.22 pJ. As a result, the total power consumption for the HVLS operating with a 1.5-MHz clock signal is 165.3 μ W.

(C) Voltage-Controlled Oscillator

Figure 5.10 shows the post-layout simulation results of the CSVCRO, presenting its frequency-voltage characteristics. The output frequency range of the CSVCRO, corresponding to a control voltage (V_{ctrl}) varying from 0 to 2.6 V, spans between 4.25 MHz and 313.28 MHz. It is important to note that the CSVCRO stop oscillating when the control voltage (V_{ctrl}) surpasses 2.6 V.

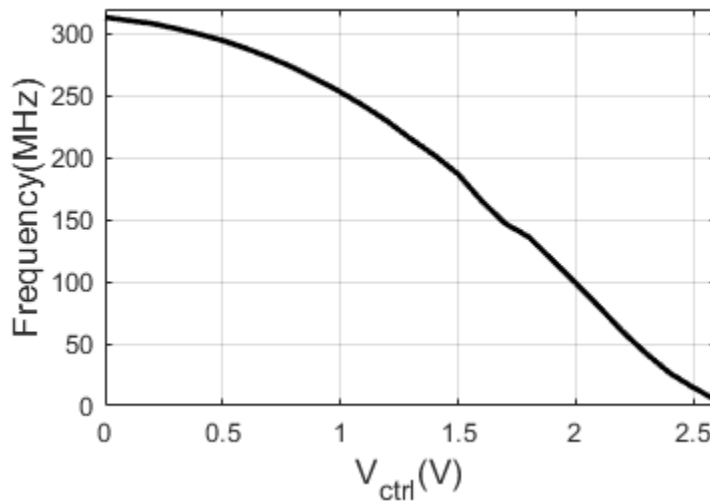


Figure 5.10 Post-layout simulation results illustrating the frequency-voltage characteristics of the CSVCRO.

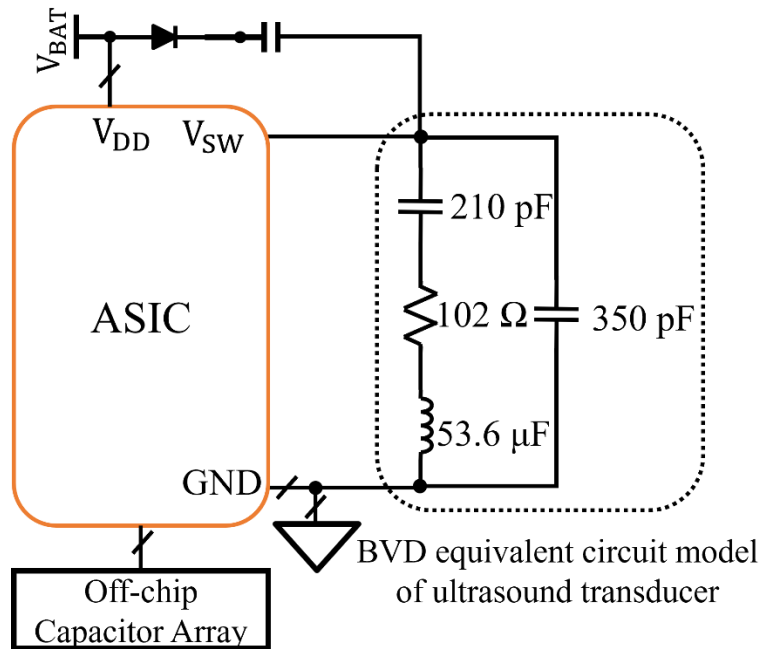
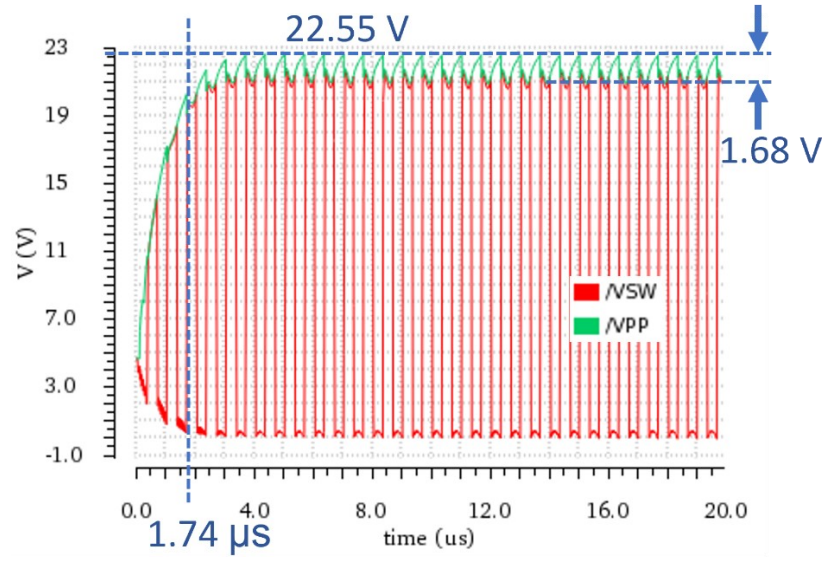


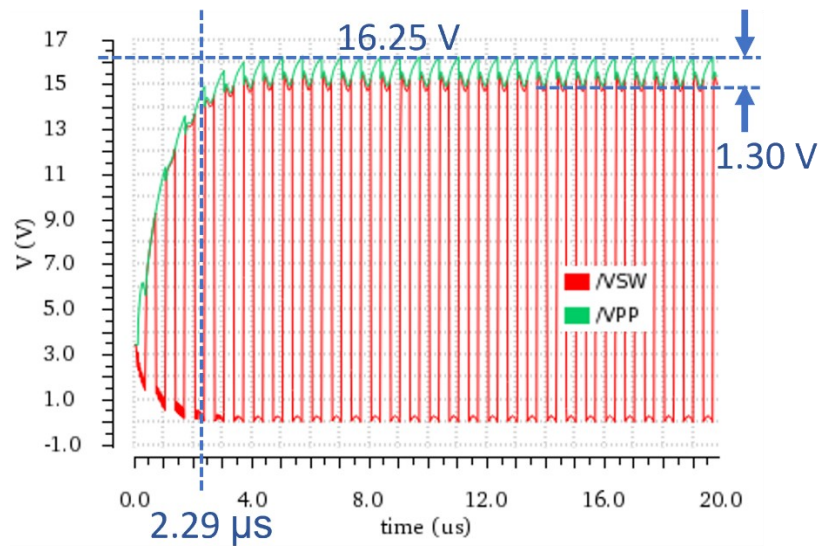
Figure 5.11 The brief schematic of the ASIC chip post-layout simulation.

(D) Top Level

The ultrasound transducer employed in conjunction with the proposed ASIC chip was produced by APC International, Ltd (PA, USA). This customized transducer features an 11-mm diameter and is designed to operate at a single resonant frequency of 1.5 MHz. The APC ultrasound transducer was equivalently represented using a Butterworth-Van Dyke model in the simulation, as shown in Figure 5.11, whose parameters were obtained from impedance fitting. In the simulation, the clock frequency output from the CSVRO for the charge pump module was set at 26.3 MHz. Figure 5.12(a) provides the entire chip post-layout simulation results, illustrating the behavior of V_{PP} and V_{SW} during the chip's startup phase. The charge pump's output voltage reached a maximum of 16.25 V with a 1.3-V ripple, and the startup time was measured at 2.3 μ s. Looking into the V_{PP} and V_{SW} waveforms reveals that the primary cause of the V_{PP} ripple was the in-rush current to the load, instead of the charge pump's controlling clock.



(a)



(b)

Figure 5.12 Post-layout simulation results depicting the output voltage waveforms for the charge pump (VPP) and the HB driver (VSW) with power supplies of (a) 3.7 V and (b) 5 V.

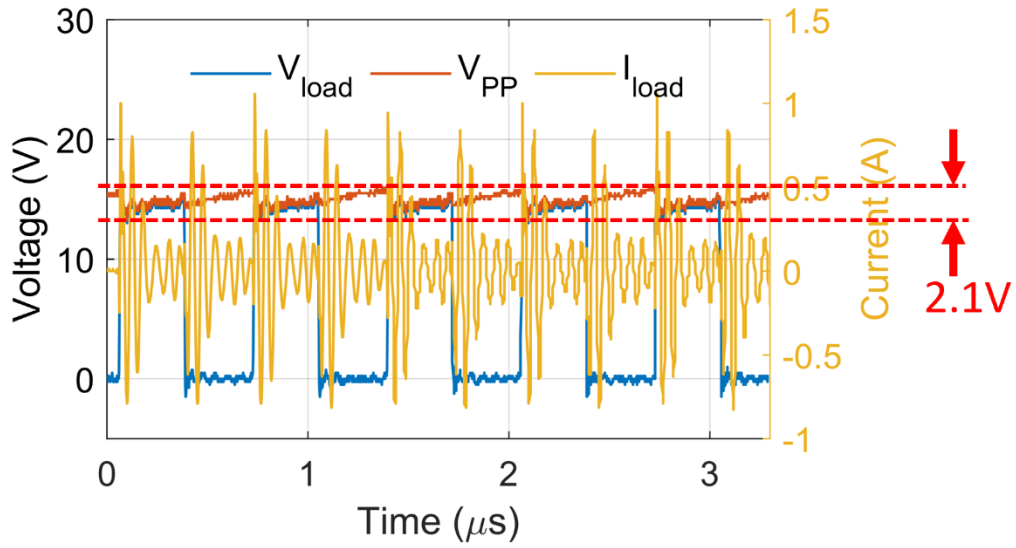
Table VIII presents the full details of the simulation results of the input power, output power, and power efficiency of the different components, including the HB drive, the DC-DC booster converter, and the entire ASIC chip. As the core power management component in the system, the charge pump was capable of delivering 89.2 mW to the load, achieving an energy conversion efficiency of 36.86%. The remaining parts of the ASIC chip, encompassing the digital circuit block, the VCO, the HVLS, and the gate driver, consumed approximately 2 mW in total. To further evaluate the system's performance, the simulation was then repeated using a 5-V power supply, and the resulting output waveform and power conversion efficiency are displayed in Figure 5.12(b) and Table VIII, respectively. Under the 5-V power supply scenario, the charge pump's output voltage reached a maximum of 22.55 V with a 1.68-V ripple, and the startup time was reduced to 1.74 μ s. In this configuration, the charge pump could deliver a power of 165.5 mW to the load, with an energy conversion efficiency of 36.16%.

Table VIII Post-layout simulation performance results.

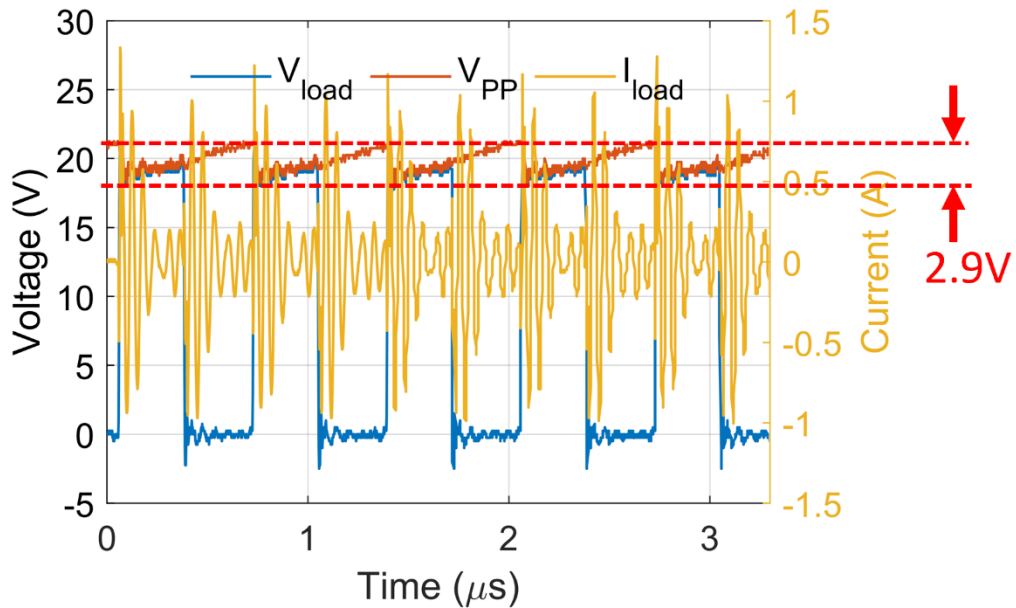
Power	Component	Direction	Power	Efficiency
3.7V	Half-bridge transducer driver	input	89.2	96.97%
		output	86.5	
	DC-DC booster converter	input	241.9	36.87%
		output	89.2	
	Entire ASIC chip	input	243.5	35.52%
		output	86.5	
5V	Component	Direction	Power	Efficiency
	Half-bridge transducer driver	input	170.7	96.95%
		output	165.5	
	DC-DC booster converter	input	454.8	37.53%
		output	170.7	
	Entire ASIC chip	input	457.7	36.16%
output		165.5		

5.3.2 Test Results

After receiving the chip from the manufacturer, we developed the corresponding peripheral circuit and conducted tests. All capacitors in the capacitor array of the peripheral circuit were 4.7-nF X5R capacitors. For testing purposes, we employed a PZT transducer manufactured by APC International, Ltd (PA, USA), characterized by a single resonance frequency of 1.5 MHz and a radiating surface area of 0.95 cm². We used an MFIA Impedance Analyzer (Zurich Instruments, Zürich, Switzerland) to measure the impedance of the PZT transducer, obtaining a result of $96.2 \Omega \angle -25.33^\circ$ at 1.5 MHz. To record output waveforms, we utilized the Oscilloscope Tektronix TBS 2000, measuring the voltage on the load (V_{load}), the output voltage of the charge pump (V_{PP}), and the current on the load (I_{load}). A precision DC power supply, Keithley 2231A-30-3 (Keithley Instruments, OH, USA), was employed to power the system, which can provide power dissipation data on its front panel. To measure the current on the load, we inserted a 0.5- Ω series resistor on the ground side of the transducer and measured the voltage across it. Figure 5.13(a) displays the waveforms measured with a 3.7 V power supply, while Figure 5.13(b) shows the waveforms measured with a 5 V power supply. During the testing process, the controlling voltage was adjusted to achieve optimal conditions. We measured the ultrasound power output of the transducer using the ultrasound power meter UPM-DT-1000PA (OHMIC Instruments, MO, USA).

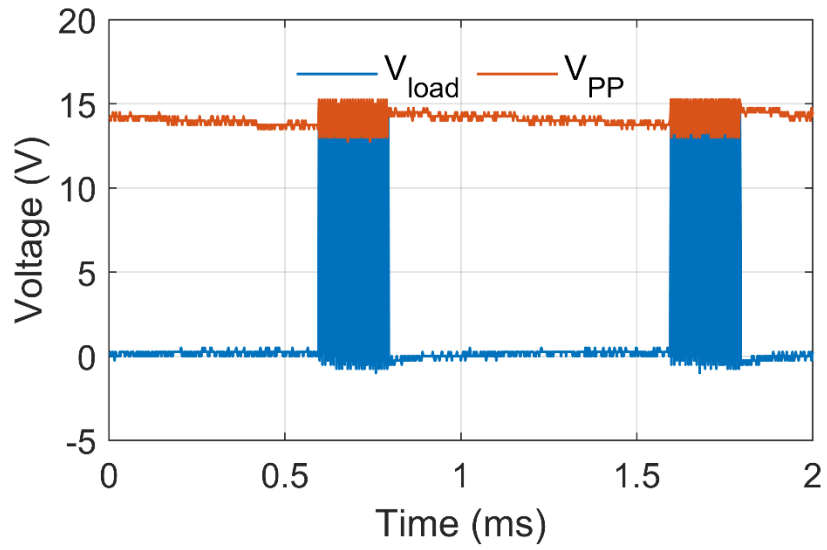


(a)

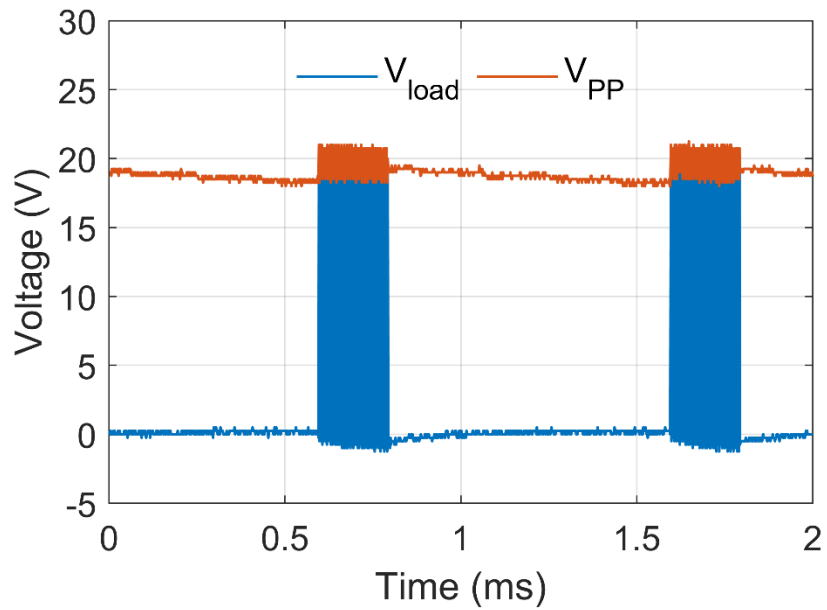


(b)

Figure 5.13 Microsecond-scale waveforms depicting the voltage on the load (V_{load}), the output voltage of the charge pump (V_{PP}), and the current on the load (I_{load}) using power supplies of (a) 3.7 V and (b) 5 V.



(a)



(b)

Figure 5.14 Millisecond-scale waveforms depicting the voltage on the load (V_{load}), the output voltage of the charge pump (V_{PP}), and the current on the load (I_{load}) using power supplies of (a) 3.7 V and (b) 5 V.

Figure 5.13 (a) and Figure 5.13(b) illustrate that when the load voltage (V_{load}) rose, the output voltage of the charge pump (V_{PP}) underwent a prompt decline. This event can be attributed to the significant charge transfer from V_{PP} 's energy storage capacitor to the load when switch Q1 was closed. At other moments, due to the capacitive attributes of the ultrasound transducer, the load acted as an open circuit for DC voltage, enabling the charge pump to reestablish V_{PP} to its prior value. The detected ripple in V_{PP} was primarily a consequence of this rapid drop and the recovery process, which was in agreement with the simulated outcomes. The documented ripple measures 2.1 V for a power supply of 3.7 V and 2.9 V for a power supply of 5 V. Moreover, the impedance mismatch gave rise to conspicuous ringing in both V_{load} and I_{load} . However, the ultrasound transducer's singular resonant frequency property ensures it was less affected by such irregularities. Figure 5.14(a) and Figure 5.14(b) show the V_{PP} and V_{load} waveforms in a millisecond range, explicitly revealing the chip's pulsating operation mode with a 20% duty cycle and a 1 kHz pulse repetition frequency. During the 80% idle phase, the charge pump was deactivated to preserve source energy. It can be also found that V_{PP} declined slowly in the idle phase due to the leakage current in the idle state.

Table IX Comprehensive overview of the system performance for the proposed LIPUS chip.

Power Supply	3.7 V	5 V
Input power of the chip	361.9	655
Output power to the load (mW)	103.3	181.5
Power efficiency of the chip	28.54%	27.71%
Output ultrasound Power (mW)	30	51
Output ultrasound Power intensity (mW/cm ²)	31.6	53.7

Table IX provides a comprehensive summary of the power conversion performance for the proposed LIPUS system. Although the ASIC has a power conversion efficiency of only 27-

29%, it remains capable of powering the ultrasound transducer. As a result, the transducer produces 28 mW or 49 mW of ultrasound power when supplied with 3.7 V or 5 V, respectively, corresponding to an ultrasound power intensity of 29.5 mW/cm² or 51.6 mW/cm². A significant advantage of this LIPUS system is its absence of inductors, making it well-suited for MRI settings.

5.3.3 Discussion

When combined with a suitably designed peripheral circuit and a specialized ultrasound transducer, the proposed ASIC chip can provide an average ultrasound power intensity of 29.5 mW/cm² or 51.6 mW/cm². These levels correspond to a fundamental frequency of 1.5 MHz, a pulse repetition frequency of 1 kHz, and a duty cycle of 20% using a power supply of either 3.7 V or 5 V. This range of power intensities and frequency parameters are applicable to a wide array of treatments and is compatible with MRI environments.

Recent research has shown that LIPUS devices with comparable frequency settings and average power intensities are effective in various therapeutic applications. For example, LIPUS with an average power intensity of 30 mW/cm² has proven to significantly speed up orthodontic treatment and minimize tooth root resorption caused by orthodontic procedures [256, 263]. The same parameter setting has also been found to enhance fracture healing and encourage osteogenic activity surrounding implants [274, 275]. Furthermore, other research groups have verified the effectiveness of LIPUS with an average power intensity of 50 mW/cm² in promoting the growth of bone marrow mesenchymal stem cells [276, 277].

Table X offers a comparison between the proposed ASIC chip's performance and that of other recent studies [271, 278, 279], which utilize charge pumps to achieve relatively high output

power demands (above the mW range). Typically, charge pumps are designed for μA -range current loads [280]. Although [278] displays superior power conversion efficiency, the proposed work can deliver higher output power (181.5 mW vs 49.5 mmW). When compared to [271], the proposed work exhibits both improved power conversion efficiency and increased output power capacity. In addition, the proposed work integrates a digital control block for ultrasound signal generation, necessitating only a few passive electronic components to create an ultrasound driver system. This integration greatly contributes to the miniaturization of LIPUS driver systems, making them more portable and easier to deploy in various clinical settings.

Table X Comparison with other similar state-of-art works ICs.

Work	This work	[271]	[279]	[278]
Technology	0.35 μm HVCMOS	0.18 μm HVCMOS	0.35 μm HVCMOS	0.25 μm BCD
Supply Voltage	5 V	3.7 V	3.7 V	3 V
Number of stages	4	4	36	4
Output Voltage	21.5 V	14 V	120 V	9.3 V
Frequency	10-60 MHz	20 MHz	10 MHz	N/A
Pumping Capacitor	off-chip 4.7 nF	on-chip 132 pF	on-chip N/A	on-chip 100pF
Power efficiency	27.30%	17%	12.60%	41% @ 49.5 mW
Output Power	181.5 mW	72 mW	13.7 mW	49.5 mW
Die area	2.0 \times 2.0 mm ²	N/A	3.9 \times 5.6 mm ²	2.01 \times 1.12 mm ²

The proposed ASIC has a limitation in that fluctuations in supply voltage and temperature may cause changes in the frequency of the VCO, which can subsequently affect the operation of the charge pump. To guarantee stable performance, it is recommended that the ASIC be powered by a consistent power supply, such as a USB port. If a lithium battery is employed as the power source, a low-dropout (LDO) regulator is required to stabilize the voltage. To address the issue of temperature changes, a thermal sink can be installed on the chip to

maintain temperature stability during operation. Additionally, the QFN36 package is used in the chip design to address potential thermal issues. With these solutions in place, experimental testing has demonstrated stable performance.

5.4 Conclusion

This study presents a LIPUS interface chip specifically designed for portable medical therapy devices, addressing the growing demand for compact and accessible therapeutic solutions. The ASIC chip integrates a charge pump, a transducer HB driver, a VCO, an HVLS, and a digital circuit block, paving the way for a highly integrated LIPUS system. The chip was fabricated using the advanced AMS 0.35- μm High-Voltage CMOS Process Technology (H35B4D3), which enables the integration of high-voltage components and digital circuitry on a single chip. This feature significantly reduces the overall size and complexity of the system. Additionally, only a small number of passive electronic components are needed to assemble a complete LIPUS driver system, rendering it an economical and portable solution.

Experimental evaluations demonstrate that the chip can deliver an output of 181.5 mW (103.3 mW) with a power supply of 5 V (3.7 V) and achieves a power conversion efficiency of approximately 28%. Given this power output capability, the LIPUS driver system can generate a SATA of 29.5 mW/cm² or 51.6 mW/cm² (fundamental frequency 1.5 MHz, pulse repetition frequency 1 kHz, duty cycle 20%) when powered by 3.7 V or 5 V, respectively. Such ultrasonic power intensities have extensive applicability across various therapeutic contexts, including bone fracture healing, orthodontic treatments, and stimulation of stem cell proliferation.

A key advantage of the proposed chip is its inductor-free design, making it compatible with MRI environments. This compatibility expands the potential applications of the LIPUS

system as it can be safely used in conjunction with MRI for diagnostic and therapeutic purposes. This compact, affordable, and wearable LIPUS device offers a competitive edge over existing commercial LIPUS devices, which are often bulky and expensive. The miniaturized design not only enhances patient comfort but should also facilitate the widespread adoption of LIPUS therapy in various medical settings, from hospitals to home-based treatments.

6. Exploring the Potential of Low-Intensity Pulsed Ultrasound for Neural Cell Growth Promotion and Nervous System Regeneration: An In-vitro Study

The content of this chapter has been submitted as a manuscript for review to Nature Mental Health as " Low-intensity Pulsed Ultrasound Enhances Neurite Growth in Serum-starved Human Neuroblastoma Cells" by Xuanjie Ye, Zitong Wang, Rebekah van Bruggen, Yanbo Zhang, and Jie Chen.

6.1 Introduction

The nervous system, an intricate component of living organisms, is vital for managing a multitude of critical physiological functions such as cognition, sensation, movement, and homeostasis [281]. The importance of this system in our health can never be overstated, and any disorders in the nervous system could pose severe consequences for affected individuals [282-285]. However, the nervous system is also vulnerable. Neurological disorders, including brain and spinal cord injuries, strokes, diseases like Alzheimer's, and nerve injuries, have a significant impact on the quality of life of patients. The prevalence of those neurological disorders also puts substantial pressure on healthcare systems and society [286-292].

As the study of neurological diseases continues to deepen, it is recognized that promoting nerve regeneration and repair is an essential therapeutic approach to restoring lost or damaged neurological function in individuals [293, 294]. Consequently, there is a growing interest in exploring innovative treatments and techniques that could advance neural repair and regeneration. To address this demand, understanding the molecular and cellular mechanisms that determine nerve repair and regeneration is crucial to develop targeted therapeutic strategies

[295]. At present, with the continuous advancement of nervous system biology and related technologies, new treatment methods are emerging. Researchers have looked into a range of potential treatments, including stem cell therapy [296], gene therapy [297], biomaterials [298, 299], and electrical stimulation [300, 301], among others. The effectiveness of these techniques for nerve repair and regeneration has been demonstrated by experimental results. These advances provide patients with the hope for the treatment of neurological diseases.

In recent years, LIPUS has emerged as a non-invasive, safe, and effective physical therapy method, achieving lots of progress in various therapeutic fields [93]. The hypothesized therapeutic principle of LIPUS involves using the mechanical and other non-thermal effects of ultrasound waves to produce biological effects on the intra- and extracellular environment [93]. LIPUS has been proven to promote fracture healing and bone density recovery in the field of bone fracture healing [302]. In the field of tissue repair, LIPUS has also demonstrated favorable therapeutic effects on soft tissue injuries [92], inflammation [303], wound healing [304], cardiovascular diseases [305], and tumor treatment [306], among others.

In addition to these applications, many studies have explored the effects of LIPUS on the nervous system. Among them, most of these studies mainly emphasized the neuromodulatory effect of LIPUS [307]. In addition, many studies have also explored the role of LIPUS in promoting nerve regeneration and repair. Mai Sato *et al.* found that LIPUS can promote the recovery of facial skin sensory loss after inferior alveolar nerve transection, and may become a new therapy for nerve injury [111]. Another study demonstrated that LIPUS at an intensity of 250 mW/cm² significantly improved the rate of axonal regeneration in a rat model with sciatic nerve autografts [112]. On the other hand, Eu-Deum Kim *et al.* explored the combination of LIPUS with transcutaneous electrical nerve stimulation (TENS) for the treatment of painful knee

OA [308]. While both treatments showed improvements in pain and physical function, this study found no significant difference between the combined treatment and TENS alone. Furthermore, the combination of LIPUS and induced pluripotent stem cell-derived neural crest stem cells (iPSCs-NCSCs) has been shown to enhance the regeneration and reconstruction of transected sciatic nerves in rats, providing a cost-effective approach for peripheral nerve regeneration [309]. In another study, the combination of LIPUS and nerve growth factor (NGF) was proven to promote neurite outgrowth, which is a crucial process in neural regeneration [310]. Overall, these findings indicate that LIPUS holds promise as an effective therapy for neural regeneration and repair in various applications.

Although LIPUS has made significant progress in the treatment of neurological diseases, several key issues must be addressed before its clinical application. One of the issues is identifying specific ultrasound parameters such as PRF, UFF, SATA, and duty cycle, which may vary depending on the type of neurological disorder. In addition, the molecular and cellular mechanisms of LIPUS in treating neurological diseases have not been studied in detail, and there are only some hypotheses. Therefore, future studies should aim to determine the optimal ultrasound parameters for different neurological disease models and the mechanisms for LIPUS therapy.

In order to investigate the effects of LIPUS on the nervous system, our research commenced with an *in vitro* study utilizing SK-N-SH cells in a serum-deprived environment as the experimental model. SK-N-SH cells, derived from a human neuroblastoma cell line, serve as a representative model for the nervous system and are extensively employed in related research [311-314]. This study aimed to assess the impact of LIPUS on neural cell growth, as well as to examine its influence on the signaling pathways within neurons, including key proteins such as

the mammalian target of rapamycin (mTOR), extracellular signal-regulated kinase (ERK), Protein kinase B (Akt), and brain-derived neurotrophic factor (BDNF). mTOR is a serine/threonine protein kinase that serves as a central regulator of cell growth, metabolism, and protein synthesis. mTOR signaling plays a crucial role in neural development, synaptic plasticity, and memory formation [315]. ERK is a group of mitogen-activated protein kinases (MAPKs) that regulate various cellular processes, including cell survival, proliferation, and differentiation. ERK signaling is also critical in neuronal plasticity and long-term memory formation [316]. Protein kinase B (PKB), also known as Akt, is a serine/threonine kinase involved in regulating cell survival, growth, and metabolism [317]. Akt signaling is crucial for neuronal development and function, and its dysregulation has been implicated in various neurological disorders. BDNF is a neurotrophin that supports the survival of existing neurons and encourages the growth, differentiation, and synaptic plasticity of new neurons [318]. BDNF has a significant impact on learning, memory, and overall brain function. In addition to the signaling pathways, we also explored various ultrasound parameter settings to identify the optimal conditions for LIPUS treatment. By adjusting these parameters, we were able to investigate the LIPUS mechanism. Overall, our experiments aim to look into these mechanisms, which are crucial for determining the effective and safe application of LIPUS in clinical settings.

6.2 Materials and Methods

6.2.1 LIPUS Exposure System

In our study, the well-on-transducer structure *in vitro* ultrasound therapy approach was adopted, in which the well was strategically placed on a planar transducer and coupled with a gel medium. This configuration is typically favored for ultrasound therapy studies on cells or tissue samples due to its simplicity and user-friendly nature [319]. Acoustic matching was achieved

through the utilization of a gel or water coupling layer, ensuring efficient energy transfer between the transducer and the sample. The entire experimental setup is depicted in Figure 6.1, and the LIPUS stimulation methodology is shown in Figure 6.2. We developed a miniaturized, customizable ultrasound driving device. This device allows for precise adjustment of ultrasound amplitude, UFF, PRF, and duty cycle, enabling rapid and straightforward configuration and delivery of a diverse range of ultrasound parameters.

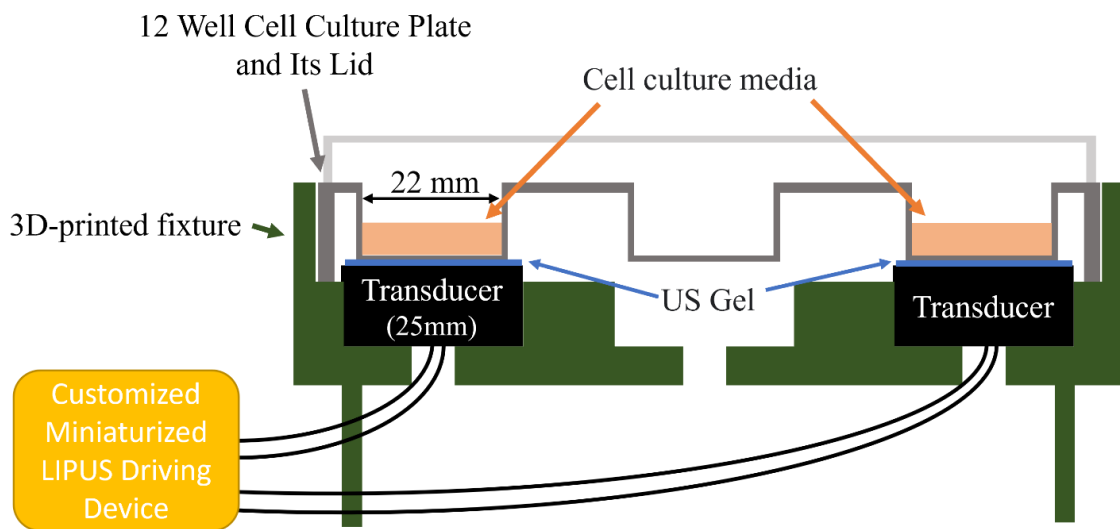


Figure 6.1 Overview of the LIPUS exposure setup.

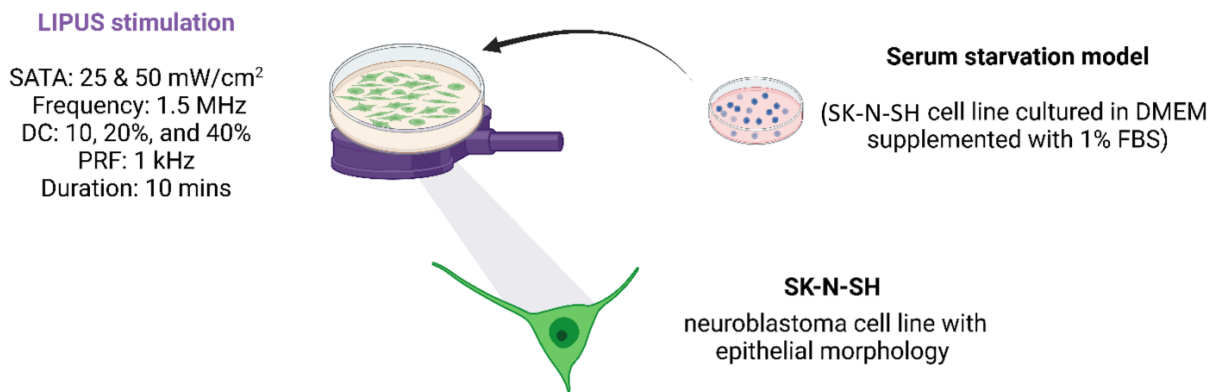


Figure 6.2 LIPUS stimulation methodology (Created with BioRender.com).

In this investigation, the UFF and PRF were constantly maintained at 1.5 MHz and 1 kHz, respectively. The study also aimed to examine the influence of different SATA intensities and duty cycles on cellular responses. To this end, we designed four LIPUS treatment groups with distinct parameter settings: (A) 50 mW/cm², 40%, (B) 25 mW/cm², 20%, (C) 50 mW/cm², 20%, and (D) 25 mW/cm², 10%. Groups A and B shared the same ultrasound intensity, with different duty cycles; similarly, Groups C and D shared the same ultrasound intensity, with different duty cycles. In addition to this, the intensities of groups A and B were 0.707 times that of groups C and D.

Customized ultrasound transducers were designed and fabricated exclusively for this experiment, featuring a UFF of 1.5 MHz and a diameter of 25 mm. The 12-well cell culture plates arranged in a 3x4 grid were employed for the cell culture, with cells seeded in the wells located at the four corners. Each well had a diameter of 22 mm, which was smaller than the ultrasound transducer. This design ensured complete coverage of the entire well, thereby allowing all cells within the well to be exposed to LIPUS. Cells were seeded exclusively at the four corners to facilitate the simultaneous LIPUS treatment of four wells, thereby improving the efficiency of the experiment. The unoccupied central wells served to minimize ultrasound crosstalk between adjacent wells, reducing potential interference effects. Ultrasound gel (Wavelength® MP Blue Multi-Purpose Ultrasound Gel, ON, Canada) was employed to couple the ultrasound transducer and the cell culture plate, ensuring the ultrasound transmission efficiency.

6.2.2 Cell Culture and LIPUS Treatment

In this study, SK-N-SH cells were cultured in Dulbecco's Modified Eagle Medium (DMEM; 319-005-CL, WISENT INC.) supplemented with 10% fetal bovine serum (FBS;

090150, WISENT INC.) in a humidified incubator at 37°C, referred to as complete media. For seeding, the SK-N-SH cell suspension was diluted to a concentration of 10,000 cells/mL, and 1 mL of the cell suspension was added to each well, resulting in an initial cell count of 10,000 per well. After 6 hours, when the majority of the cells had attached to the well bottom, the culture media was removed, and the wells were gently washed three times with FBS-free DMEM. Subsequently, the cells were cultured in low-serum media, comprising DMEM supplemented with 1% FBS, to establish a starvation cell model.

In this experiment, there were six groups: a healthy control group cultured in complete media without LIPUS treatment, a starving-control group cultured in low-serum media without LIPUS treatment, and experimental groups A, B, C, and D cultured in low-serum media and subjected to various LIPUS treatment parameters. For the treatment groups, the first time LIPUS treatment was performed 18 hours after the switch to low-serum media (on day 2), with a 10-minute LIPUS exposure using the described setup. To ensure a more uniform ultrasound distribution, the transducer was rotated 180° after the first 5 minutes of treatment and then continued for the remaining 5 minutes. The 10-minute LIPUS treatment was repeated every 24 hours. Ten minutes after the completion of the fourth LIPUS treatment (on day 5), cell supernatants were collected for cell viability assays, and cells were harvested and lysed with RIPA buffer (25 mM Tris-HCl pH 7.6, 150 mM NaCl, 5 mM EDTA, 1% Triton X-100, 1% sodium deoxycholate, 0.1% SDS) mixed with protease inhibitor (A32963, Thermo Scientific) and phosphate inhibitor (A32957, Thermo Scientific). The lysates were then used for Western blot analysis.

6.2.3 Cell Cytotoxicity Quantification

The LDH-Cytotoxicity Assay Kit II (ab65393) was employed for the measurement of lactate dehydrogenase (LDH) release, a marker of cytotoxicity, in cell culture samples. The kit components included a water-soluble tetrazolium (WST) substrate mix, LDH assay buffer, cell lysis solution, stop solution, and LDH positive control. Additional required materials were a microcentrifuge, pipettes and tips, a colorimetric microplate reader, a 96-well plate, and an orbital shaker.

First, the supernatants were transferred to an optically clear 96-well plate (10 μ L/well). The LDH reaction was then carried out by reconstituting the WST substrate mix in 1.1 mL ddH₂O for 10 minutes and thoroughly mixing. The WST substrate mix was combined with LDH assay buffer to create the LDH reaction mix (for 100 assays: 200 μ L WST substrate mix + 10 mL LDH assay buffer). Next, 100 μ L of the LDH reaction mix was added to each well and mixed well. The plate was incubated at room temperature for approximately 30 minutes. The reaction time can be increased or decreased depending on color development, and the plate can be read at multiple time points until the desired reading is observed (High: OD_{450nm} = 2.0, Low: OD_{450nm} < 0.8). The reaction was stopped with the addition of 10 μ L of stop solution and mixed well. Absorbance was read at 450 nm (440-492 nm filter), with a reference wavelength of 650 nm, using a microplate reader. Cytotoxicity was calculated using the formula: Cytotoxicity (%) = [(Test sample - Low Control) / (High Control - Low Control)] \times 100. This approach allowed for an assessment of cell cytotoxicity in the responses under various conditions, and the results can be used to infer cell viability or proliferation.

6.2.4 Cell Visualization

Immunocytochemistry (ICC), a widely used morphology technique in cell biology, enables the visualization and localization of specific proteins within cultured cells. This method involves the use of primary antibodies that bind to the target protein and fluorescent secondary antibodies that recognize and bind to the primary antibodies. ICC was performed on cultured cells following a standardized protocol. Initially, cells were washed once with phosphate-buffered saline (PBS; 311-010-CL, WISENT INC.) and fixed with 4% paraformaldehyde (PFA; 441244, Sigma-Aldrich) diluted in 1× PBS for 10 minutes at room temperature. Subsequently, cells were washed twice with 1× PBS. Then, the cells were permeabilized with 0.2% Triton X-100 (A16046, Thermo Fisher Scientific) diluted in 1× PBS for 5 minutes at room temperature, and washed three times with 1× PBS. After that, coverslips were transferred to parafilm in a humidifying chamber to prevent drying.

Blocking was performed by adding 100 µL of blocking buffer (6% normal goat serum (ab7481, Abcam) and 0.5% bovine serum albumin (BSA; A2134, Biomatik) in 1x PBS) per coverslip for 1 hour at room temperature. Primary antibodies (Tubulin, 1:500, MAB1637, Sigma-Aldrich) diluted in a 1:1 mixture of blocking buffer and 1× PBS were added and incubated for 2 hours at room temperature or overnight at 4°C. Coverslips were then washed three times for 5 minutes each with 1× PBS, and secondary antibodies (goat anti-mouse (1:1000, A-11032, Invitrogen)) properly diluted in 1× PBS were added, incubating for 1 hour at room temperature. Subsequently, after aspirating the secondary antibodies solution, coverslips were washed three times for 5 minutes each with 1× PBS and mounted in ProLong Gold antifade reagent with DAPI (P36935; Invitrogen). Finally, coverslips need to dry overnight at room

temperature in the darkness before imaging. The ICC imaging was performed using the EVOS M5000 Imaging system (Thermo Fisher Scientific Inc., MA, US).

6.2.5 Western Blot

Western blot analysis was employed to assess the levels of BDNF, ERK1/2, AKT, and mTOR. Protein lysates prepared for enzyme-linked immunosorbent assay (ELISA) analysis were quantified using the Bradford protein assay kit (Bio-Rad), and the absorbance was measured with the FLUOstar Omega Microplate Reader (BMG). Each protein sample of 5 µg was loaded and separated on a 10% SDS-PAGE gel, followed by transfer onto 0.2 µm nitrocellulose membranes (1620112, Bio-Rad). The membranes were blocked in 5% BSA in 1x Tris-buffered saline (TBS) and incubated with primary antibodies overnight. After washing, the membranes were probed with secondary antibodies and visualized using the imaging system. Band images were captured and quantified using Image Studio Lite software (LI-COR Biosciences, Lincoln, NE, Ver 5.2).

To ensure equal loading among samples, membranes were re-probed with glyceraldehyde 3-phosphate dehydrogenase (GAPDH) as a loading control. BDNF band intensities were normalized to the loading control, GAPDH; phosphorylated ERK1/2 (p-ERK1/2) band intensities were normalized to total ERK1/2; phosphorylated AKT (p-AKT) band intensities were normalized to total AKT; phosphorylated mTOR (p-mTOR) band intensities were normalized to total mTOR. The primary antibodies used included rabbit anti-BDNF (1:1000; ab108319, Abcam), rabbit anti-ERK (1:1000; 9102S, Cell Signaling), rabbit anti-p-ERK (1:1000; 4376S, Cell Signaling), rabbit anti-p-Akt (1:1000; 4060S, Cell Signaling), rabbit anti-mTOR (1:1000; 2983S, Cell Signaling), rabbit anti-p-mTOR (1:1000; 5536S, Cell Signaling), mouse anti-Akt (1:1000; 2920S, Cell Signaling), and mouse anti-GAPDH (1:1000; 97166S, Cell Signaling). The secondary antibodies employed were goat anti-rabbit-IR800 (1:10000, 926-

32211, LI-COR Biosciences) and goat anti-mouse-IR680 (1:10000; 926-68070, LI-COR Biosciences).

6.2.6 Statistical Analysis

Statistical analyses of neurite length, soma size, LDH quantification results, and Western blot quantification results were performed using GraphPad Prism software (GraphPad Software, MA, US), version 9.4. Data are presented as means \pm standard errors of the mean (SEM) and were obtained from at least three independent experiments. To compare the complete media, starving-control, and LIPUS-treated groups, a one-way analysis of variance (ANOVA) followed by a post hoc multiple comparison test was employed. The observed power was calculated for each analysis to ensure that the sample size was adequate for supporting the findings. Statistical significance was established at a p-value threshold of < 0.05 , with asterisks indicating significant differences between groups in the following graphs.

6.3 Results and Discussion

6.3.1 Effect of LIPUS on Cell Proliferation in SK-N-SH Cells

Prior to the cell collection on day 5, the supernatants of the cell culture medium were collected for the analysis for LDH release to assess the cytotoxicity levels in the samples. The results of this analysis are presented in Figure 6.3. In this graphical representation, all LDH release values were normalized to the complete media group. It can be observed that the LDH levels in the low-serum environment for groups A, B, C, D, and the starving control group were significantly lower than those in the complete media group, which values only at approximately 0.7. This difference exhibited high statistical significance ($p < 0.0001$). On the other hand, there were no significant differences among groups A, B, C, D, and the starving control group.

Statistical analysis revealed no significant disparities between these groups, suggesting that the low-serum conditions produced similar effects across all starvation conditions.

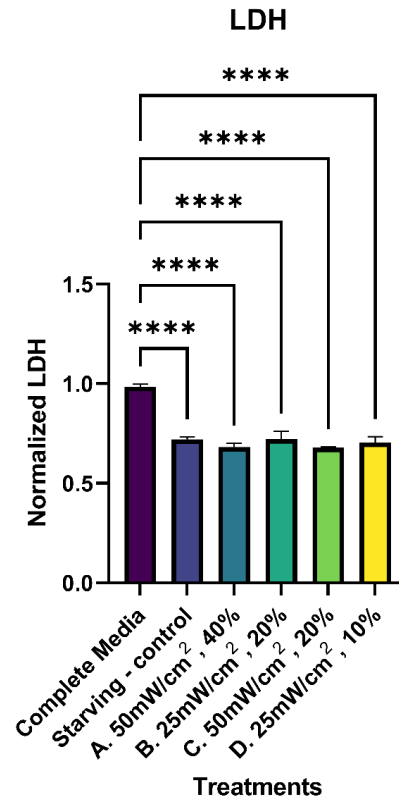


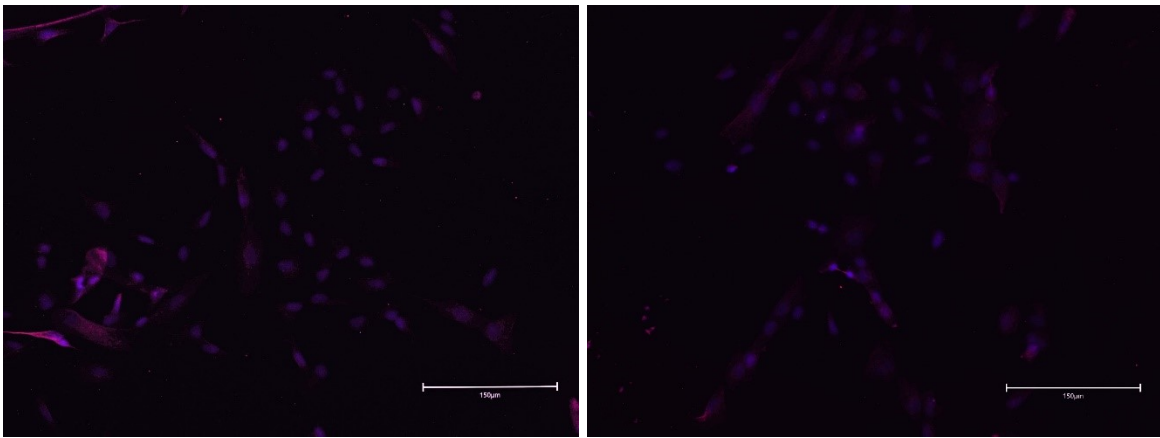
Figure 6.3 LDH result of different groups (N=3). The results were normalized to the complete media group.

Considering that the entire LIPUS treatment process spanned four days without any replacement of the culture medium, it is reasonable to assume that the availability of nutrients was limited for the low-serum culture medium during the experiment. Therefore, these cells in the low-serum culture medium tend to enter a lower metabolic state or show a reduced rate of cell division due to starvation, which eventually leads to lower LDH levels. It can be inferred that the LIPUS-treated groups A, B, C, and D, as well as the starvation control group have all successfully entered the starvation state. Such a phenomenon indicates that the experimental

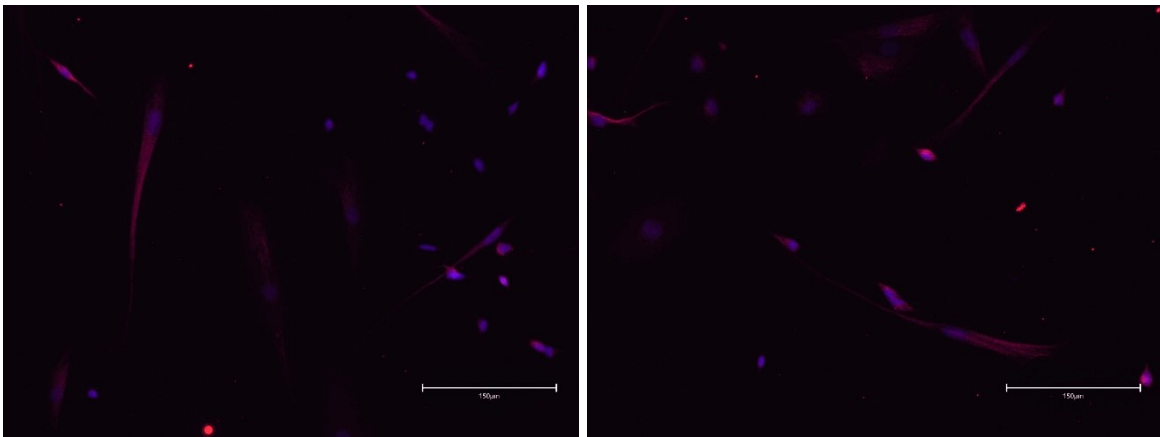
model was established successfully. Furthermore, the analysis of the data revealed that LIPUS did not exhibit any noticeable promoting or inhibitory effects on cell proliferation in these experimental groups.

6.3.2 Effect of LIPUS on Neurite Outgrowth in SK-N-SH Cells

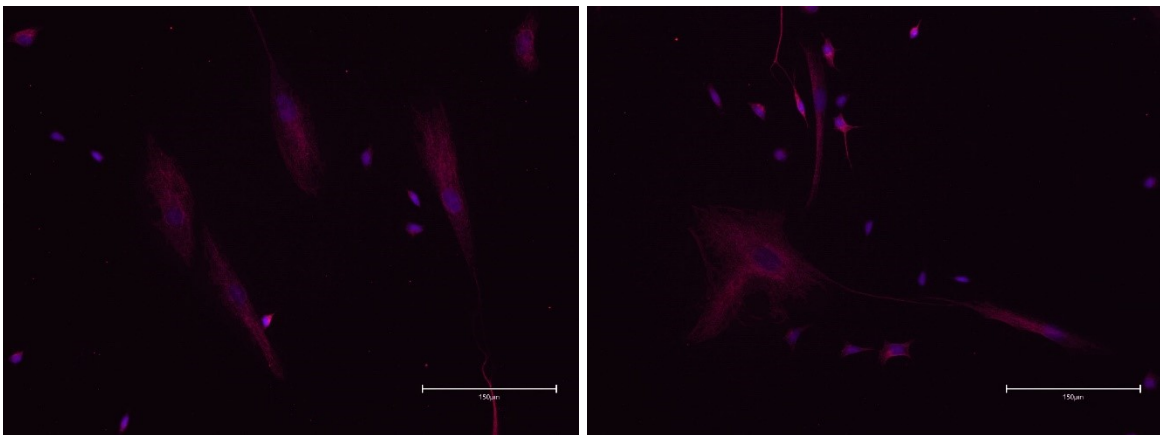
In this study, ICC imaging was used as a morphological analysis tool to study the morphological characteristics of SK-N-SH cells under different treatment conditions. The representative ICC images can be seen in Figure 6.4. Under the starvation conditions, all the Starving-control group and LIPUS-treated groups A, B, C, and D displayed a notable reduction in cell count compared with the complete media group. This feature allows observation of individual cell morphology since the neurites of each cell have sufficient space to grow and develop without excessive interconnections. This clear distinction in the cellular organization provided an ideal setting to examine the impact of the experimental conditions on neurite growth. In contrast, the complete media group exhibited a high cell density, with the majority of cells packed closely together, resulting in extensive interconnections among their neurites. In this environment, the neurites did not require significant elongation to establish functional connections. As such, statistical analysis of neurite length in the complete media group was unnecessary due to the dense cellular arrangement. Focusing on the starvation-condition groups, preliminary observations and analyses revealed that LIPUS-treated groups displayed a relative increase in neurite length when compared to the Starving-control group.



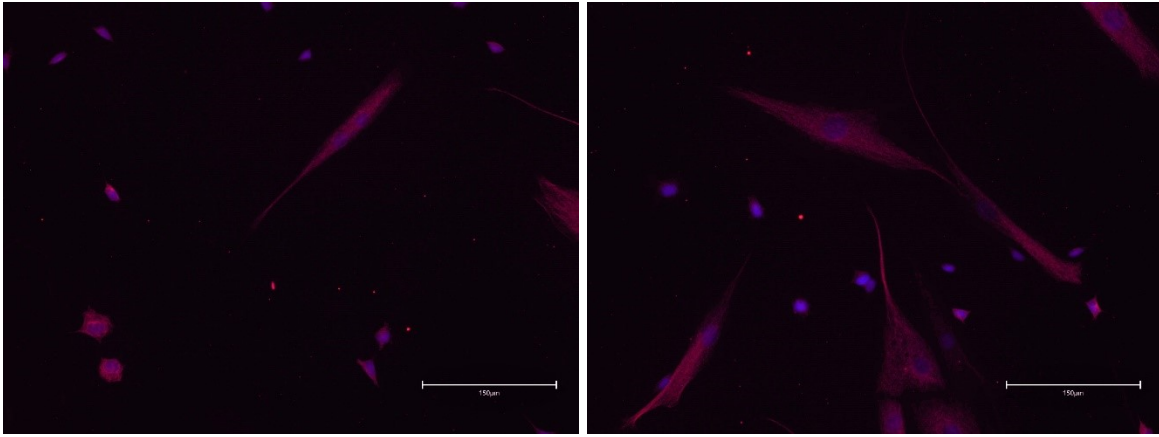
(A) Complete Media



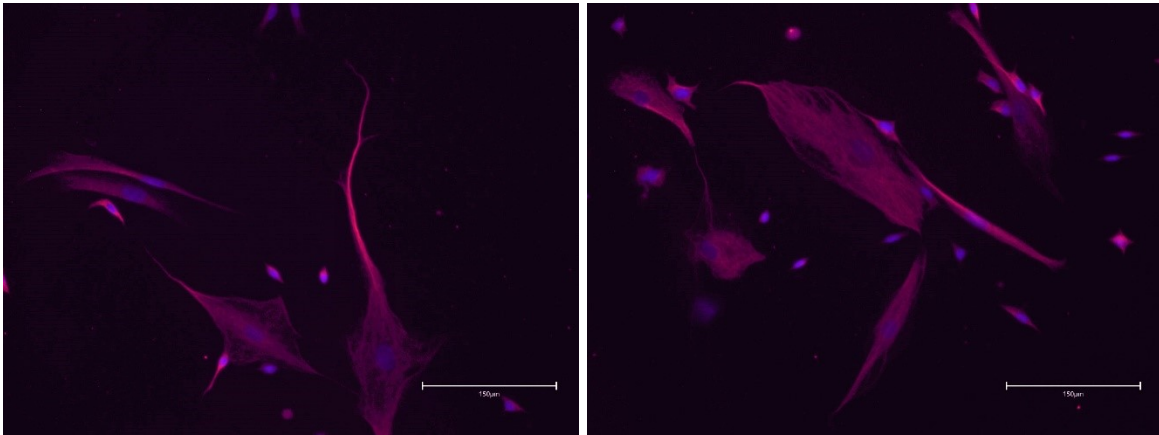
(B) Starving control



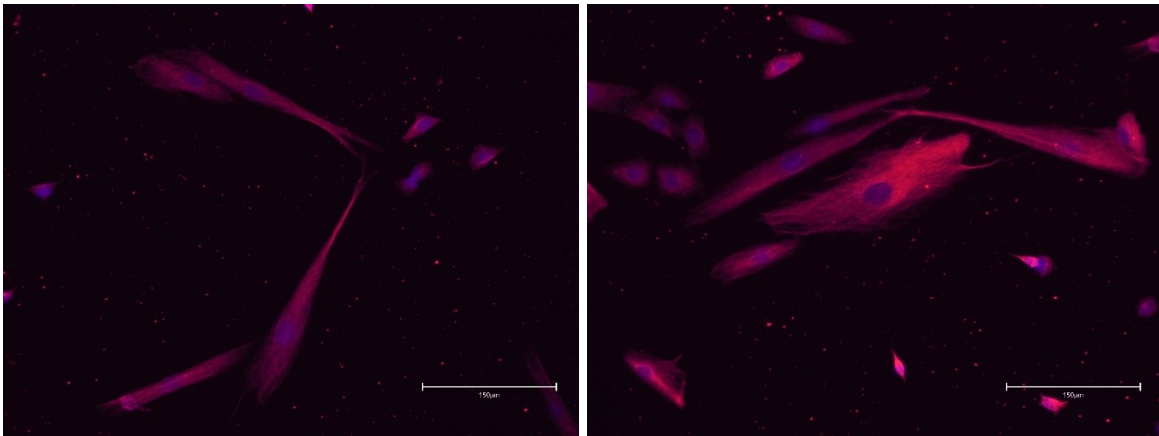
(C) Treatment A 50 mW/cm², 40%



(D) Treatment B 25 mW/cm², 20%



(E) Treatment C 50 mW/cm², 20%



(F) Treatment D 25 mW/cm², 10%

Figure 6.4 Representative ICC images of SK-N-SH cells subjected to different LIPUS treatment conditions: (A) Complete Media; (B) Starving control; (C) Treatment A 50 mW/cm², 40%; (D)

Treatment B 25 mW/cm², 20%; (E) Treatment C 50 mW/cm², 20%; (F) Treatment D 25 mW/cm², 10%.

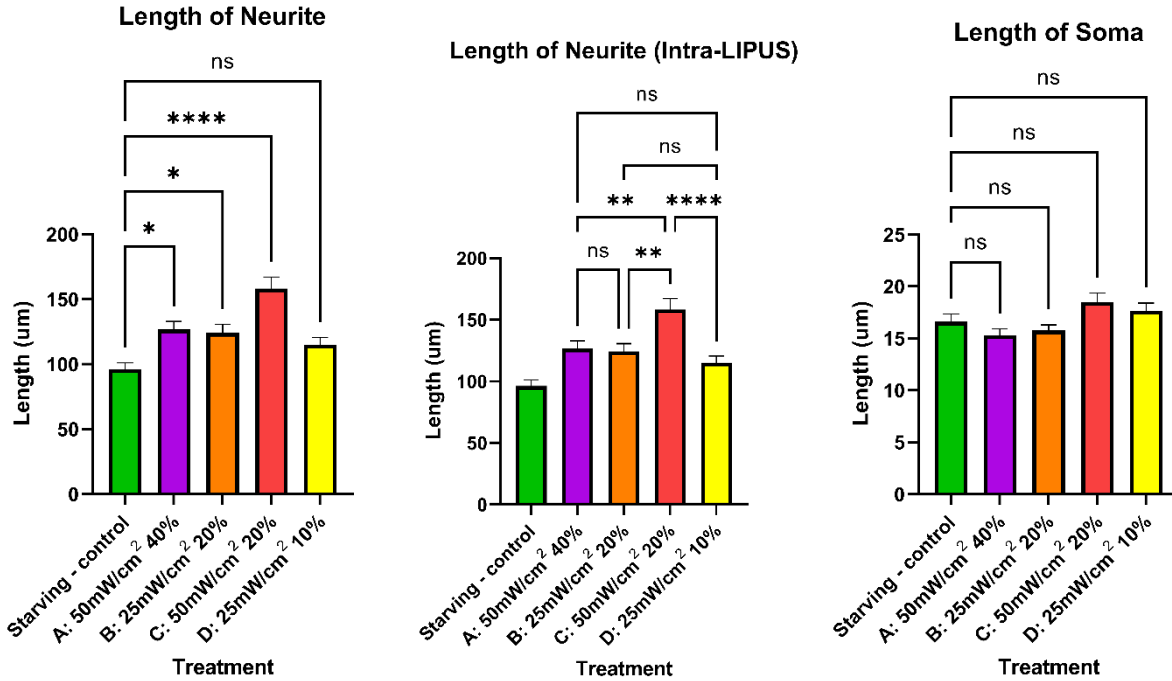


Figure 6.5 Quantified data representing the average neurite length (μm) for different treatment groups (N=90).

Subsequently, we conducted a comprehensive statistical analysis of neurite lengths in the control group and the LIPUS treatment groups under low-serum conditions to investigate the effects of different LIPUS parameter settings on neuronal growth. During the analysis, we only considered the longest neurite of each cell, which is regarded as the axon, since this axonal length is critical for signal transmission and overall neuronal functionality [320]. In addition, we quantified the length of the cell soma. The soma length measurement was taken at the widest point of SK-N-SH cell bodies. On the other hand, for these neurite lengths were less than the diameter of the cell body, they were not considered well-grown neurites. Consequently, we

excluded these cells from our analysis to avoid potential inaccuracies in the assessment of neurite growth. The results of the analysis are presented in Figure 6.5.

Firstly, there was no significant difference in soma length between the treatment groups and the control group. This result is a good indicator that LIPUS treatment does not increase cell volume. An increase in cell volume may be indicative of cellular transformation, which could potentially lead to tumorigenesis. The neurite lengths were as follows: starving-control $96.2 \pm 47.6 \mu\text{m}$, A $126.7 \pm 60.4 \mu\text{m}$, B $124.2 \pm 65.2 \mu\text{m}$, C $158.2 \pm 89.1 \mu\text{m}$, and D $114.9 \pm 55.2 \mu\text{m}$. The A (50 mW/cm², 40%), B (25 mW/cm², 20%), and C (50 mW/cm², 20%) groups exhibited a significant increase in neurite growth compared to the control group. In contrast, there is no statistically significant difference between the D (25 mW/cm², 10%) group and the control group. Notably, the C group exhibited a substantial increase in comparison to the other LIPUS-treated groups, with a highly statistically significant difference compared to the control group ($p < 0.0001$). Comparisons among LIPUS-treated groups A, B, C, and D revealed no significant differences among groups A, B, and D, while group C maintained statistically significant differences compared to the other LIPUS-treated groups. This suggests that the LIPUS parameter setting employed in group C might be the most effective in promoting neurite growth. In conclusion, LIPUS parameter settings A, B, and C all demonstrated a positive effect on neurite growth in cells, with the C group exhibiting the most pronounced effect.

6.3.3 Effect of LIPUS on Signaling Transduction in SK-N-SH Cells

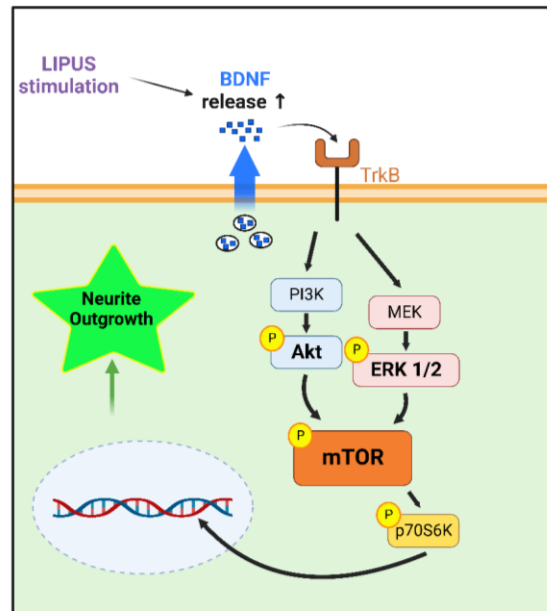
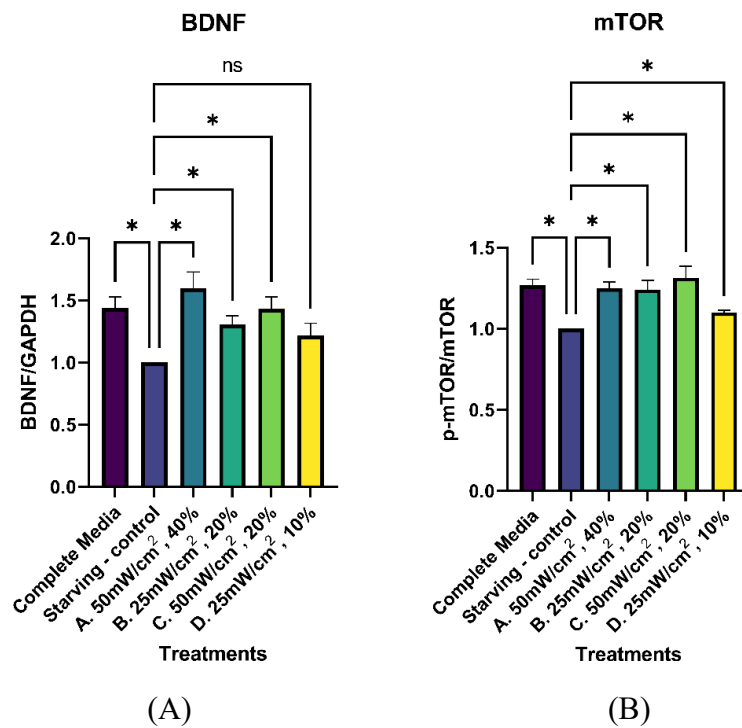


Figure 6.6 Hypothesized signaling pathway under LIPUS stimulation (Created with BioRender.com).



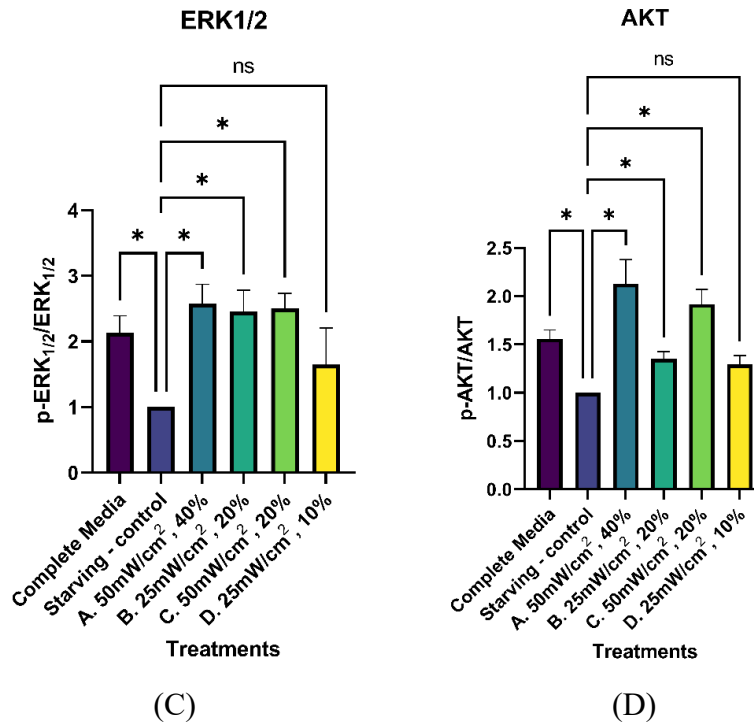


Figure 6.7 Comparison of normalized band intensity of Western Blot among different treatment groups (N=3) : (A) BDNF, (B) mTOR, (C) ERK1/2, (D) Akt.

Numerous studies have highlighted the critical roles of ERK1/2 and Akt signaling pathways in mediating growth factor (e.g., nerve growth factor and BDNF)-induced neuronal growth [310, 321]. Building upon these findings, our study investigated mTOR as a central regulator of cell growth and proposed a hypothesized signaling pathway under LIPUS stimulation, as depicted in Figure 6.6. We also compared the effects of four LIPUS parameter settings on the activation of this signaling pathway. We conducted Western blot analyses to assess BDNF levels, activation of ERK and Akt, and mTOR activation in response to LIPUS treatment, and the results are shown in Figure 6.7 and Figure 6.8.

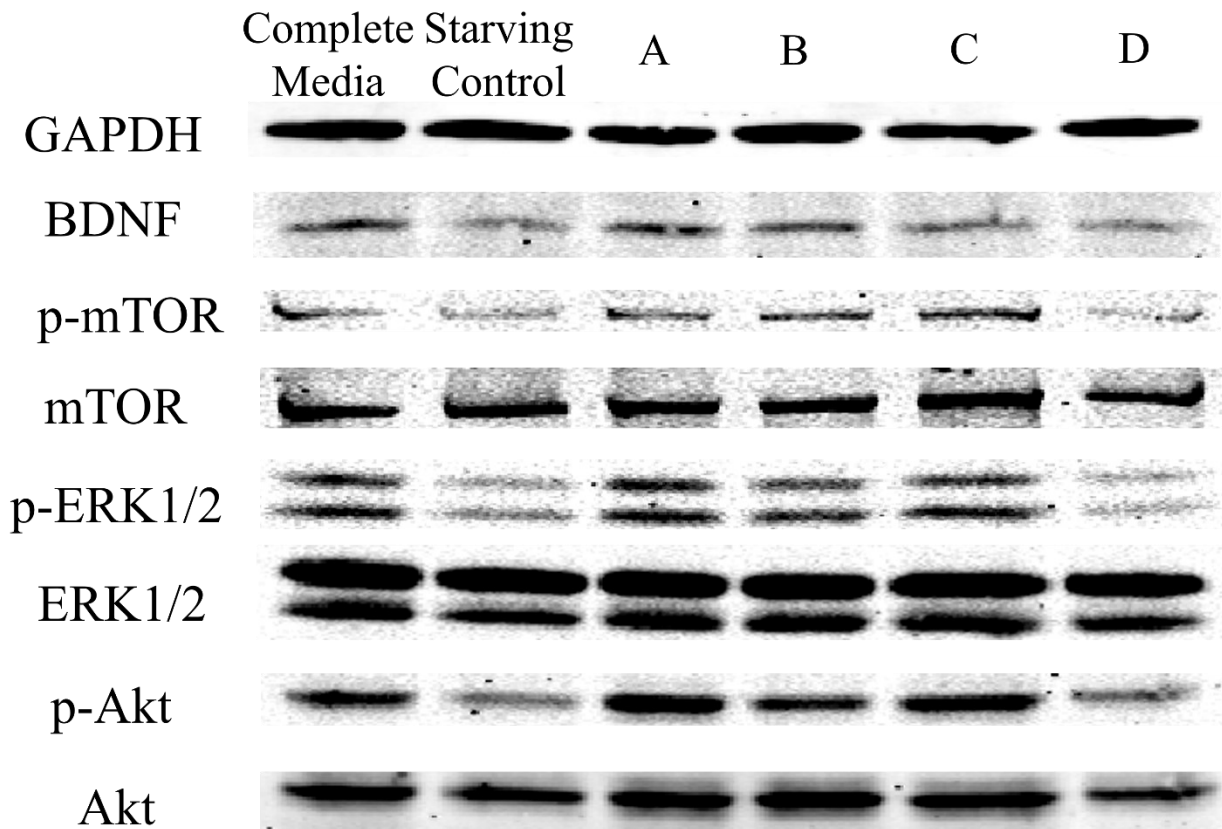


Figure 6.8 Representative Western Blot image illustrating the expression levels of GAPDH, BDNF, p-mTOR, mTOR, p-ERK1/2, ERK1/2, p-Akt, and Akt.

Our results revealed that the starving-control group exhibited significantly lower BDNF levels than the Complete Media group. Conversely, LIPUS treatment led to a significant increase in BDNF levels in treated cells, except for the D group with a 25mW/cm², 10% parameter. The results indicate that all LIPUS parameter settings have the potential to promote BDNF expression except for the D.

To further study the potential effects of LIPUS on downstream signaling components, we investigated its impact on ERK and Akt activation. The Starving-control group displayed a significant decrease in ERK1/2 and Akt activation (phosphorylation percentage) relative to the

Complete Media group. ERK1/2 and Akt activation was significantly enhanced in LIPUS-treated groups A, B, and C. However, the LIPUS-treated group D did not show a significant enhancement in ERK1/2 and Akt activation. These findings suggest that most LIPUS treatment groups effectively enhanced ERK and Akt signaling activation, except for the LIPUS-treated group D. Those results are also in line with statistical analysis results for BDNF.

As mTOR serves as a central regulator that integrates both ERK and Akt signaling pathways downstream under LIPUS stimulation, we next examined the effects of LIPUS on mTOR activation. Again, we observed a significant reduction of mTOR activation (phosphorylation percentage) in the Starving-control group compared to the Complete Media group. In the LIPUS-treated groups, a significant elevation of mTOR activation was detected except for the LIPUS-treated group D. This observation supports our hypothesis that LIPUS treatment may enhance mTOR signaling activation in the starving cell model.

In conclusion, our study provides insights into the regulatory effects of LIPUS on protein signaling pathways in SK-N-SH cells. We demonstrated that LIPUS treatment could effectively promote BDNF expression and enhance the activation of ERK, Akt, and mTOR signaling pathways in most LIPUS-treated groups. The only exception was group D with a 25mW/cm², 10% parameter. By further exploring the intricate interplay between LIPUS parameters and cellular signaling pathways, researchers can optimize LIPUS treatment protocols and develop more effective therapeutic strategies for various neurological conditions.

6.3.4 The Impact of Different LIPUS Parameters

In this study, we investigated the effects of four distinct ultrasound parameter settings on SK-N-SH cells cultured in a low-serum environment to examine the impact of varying these

parameters on cellular response. The four LIPUS-treated groups had different ultrasound parameters based on SATA intensities and duty cycles, including (A) 50 mW/cm², 40%, (B) 25 mW/cm², 20%, (C) 50 mW/cm², 20%, and (D) 25 mW/cm², 10%. Groups A and B had identical ultrasound intensities but varied duty cycles, whereas Groups A and C had identical ultrasound intensities but varied duty cycles. The intensities of Groups A and B were 0.707 times those of LIPUS-treated groups C and D.

Through a comparative analysis of ICC and Western blot studies, we observed that Group C exhibited the most significant therapeutic effects among the four LIPUS treatment groups. In contrast, Group D, which had the same ultrasound amplitude as Group C but had half the duty cycle, demonstrated the least pronounced effects. Although Groups A and C had the same SATA intensity but different duty cycles, resulting in different ultrasound amplitudes, their Western blot results were fairly similar. However, in terms of ICC results, neurite growth in Group C was significantly superior to that in Group A. The majority of previous research has focused on adjusting the SATA intensity of LIPUS while neglecting the modulation of duty cycles. In our treatment comparison, we found that even with the same ultrasound amplitude, differing LIPUS duty cycles produced varying therapeutic outcomes, as evidenced by the differences between LIPUS-treated groups C and D. Moreover, maintaining the same SATA intensity while adjusting the ultrasound amplitude and LIPUS duty cycles could also yield different results, as demonstrated by the disparities between LIPUS-treated groups A and C. Therefore, we speculate that the therapeutic efficacy of LIPUS is influenced by a combination of factors, including the mild thermal effects associated with specific power output and the mechanical vibrations resulting from ultrasound amplitude. The optimization of the duty cycle in conjunction with

SATA intensity and ultrasound amplitude holds significant potential for enhancing treatment outcomes.

Future studies should focus on systematically investigating the effects of different duty cycles, SATA intensities, and ultrasound amplitudes on different cell types and under different experimental conditions. An in-depth understanding of the interplay between these parameters and their respective contributions to the overall treatment effect is critical for developing more effective LIPUS treatment regimens. In addition, it is also necessary to conduct in-depth studies of the molecular and cellular processes governing the observed therapeutic effects. By expanding our knowledge of the underlying mechanisms and interactions among LIPUS parameters, researchers and clinicians will better tailor LIPUS treatments to specific therapeutic needs.

6.4 Conclusion

In this study, we investigated the effects of LIPUS treatment with various parameter settings on SK-N-SH cells cultured in low-serum conditions. The four LIPUS parameter settings encompass A (50 mW/cm², 40%), B (25 mW/cm², 10%), C (50 mW/cm², 20%), D (25 mW/cm², 10%). The ICC results show the stimulated neurite outgrowth in LIPUS-treated cells. The WB results demonstrated that LIPUS treatment successfully promoted BDNF expression, and enhanced the activation of ERK, Akt, and mTOR signaling pathways. Furthermore, the study revealed that the combination of SATA intensity, duty cycle, and ultrasound amplitude played a critical role in determining the therapeutic efficacy of LIPUS. Among the four LIPUS-treated groups, group C displayed the most pronounced effects, with significant enhancements in neurite growth and cellular signaling activation. In contrast, group D showed the least therapeutic impact. These results suggest that the combination of SATA intensity, duty cycle,

and ultrasound amplitude plays a crucial decisive role in the therapeutic effect of LIPUS, which was often overlooked in previous studies.

Our study provides valuable insight into the possible therapeutic use of LIPUS in promoting neuronal growth. From the experimental results at the cellular level, we can see the potential for the development of new therapeutic strategies for neurological diseases. Future research efforts should focus on how different duty cycles, SATA intensities, and ultrasound amplitudes function in various cell types and experimental settings. Furthermore, exploring the specific mechanism of how cells respond to LIPUS treatment is crucial to reveal the inner process of the LIPUS treatment effect. These developments will help researchers and clinicians customize LIPUS treatment strategies according to specific treatment needs, so as to improve patient outcomes with various neurological disorders.

7. Conclusions and Future Work

Overall, this dissertation contributed to the field of portable and wearable biomedical devices, specifically in the domains of bioimpedance and LIPUS technologies. By employing an interdisciplinary approach and scientific research methodologies, this research has addressed the development, optimization, and application of these technologies, demonstrating their potential for the early detection, monitoring, and treatment of various medical conditions. The findings of this thesis pave the way for further innovative solutions and address needs in healthcare.

In the area of bioimpedance, the first study investigated the feasibility of knee bioimpedance measurements using a bipolar electrode configuration and the relationship between bioimpedance and knee injury. This study advances the understanding of the impact of knee injury on bioimpedance. The experimental results demonstrate the potential of bioimpedance, a portable and cost-effective technique, for the early detection and continuous monitoring of knee injuries. By studying frequency selection, external factors, and the application of machine learning classification methods, this study broadens the application scenarios of bioimpedance technology.

The second study on bioimpedance proposed an EIS-based method for biomarker detection and considered the detection of anti-SARS-CoV-2 IgG antibodies in serum samples as a case study. The results demonstrate the capabilities of the EIS-based method, which offers several advantages, including fast response, high sensitivity, and minimal sample requirement. This study provides a basis for the development of rapid and efficient EIS-based diagnostic tools for multiple diseases and conditions, with the potential to be multiplexed and adapted for other biomarkers.

The third study on bioimpedance presented a portable, low-cost EIS system design, specifically engineered for POC applications. The system has demonstrated excellent accuracy and precision in the measurement of biological samples. At the same time, the system has the advantages of fast scanning speed, multi-channel support, and low excitation amplitude, which improves measurement efficiency, precision, and biological safety. The proposed EIS system has great potential to be widely used in various biomarker measurement applications, contributing to the field of POC diagnostics.

In the area of LIPUS technology, the fourth study proposed a LIPUS-interface ASIC chip specifically designed for portable medical devices to meet the growing demand for compact and accessible treatment solutions. The entire ASIC chip integrates multiple components, and it only needs a few passive components to construct a LIPUS driver system. Experimental evaluation proves that its output and power conversion efficiency were sufficient to drive the LIPUS intensities needs in therapeutic scenarios. Furthermore, it is also compatible with the MRI environment, which provides the navigation information required for LIPUS treatment. LIPUS devices based on the proposed ASIC chip can be compact, affordable, and wearable, offering competitive advantages over existing commercial LIPUS devices, improving patient comfort, and facilitating the widespread adoption of LIPUS therapy.

The fifth study investigated the effect of LIPUS treatment on neuronal growth and regeneration of the nervous system, using SK-N-SH cells cultured under low serum conditions as a case study. This study provides valuable insights into the effect of different LIPUS parameters on cellular responses, emphasizing the importance of optimizing LIPUS parameters such as SATA intensity and duty cycle. The results showed that LIPUS treatment could effectively stimulate BDNF expression, activate ERK, Akt, and mTOR pathways, and promote neurite

outgrowth. This study demonstrates the potential therapeutic application of LIPUS in promoting neuronal growth. It also suggests that the LIPUS treatment parameters should be customized according to specific treatment needs.

In summary, the findings, designs, and innovations presented in this dissertation advance the development of portable and wearable biomedical devices, specifically in the areas of bioimpedance and LIPUS technology. These studies have demonstrated the potential of these technologies for biomarker detection, early diagnosis, health management, and treatment to improve patient care and outcomes across a variety of medical conditions and healthcare settings. Based on these research results, future research can continue to explore new applications and technical optimizations of bioimpedance and LIPUS devices to improve the quality, accessibility, and efficiency of healthcare delivery.

Building upon the findings and innovations presented in this dissertation, several avenues for future work are suggested:

1. Further optimization of bioimpedance measurement device: the experimental bioimpedance measurement device can be further optimized in terms of portability. The current equipment can be further optimized with the improved selection of circuit components, and the PCB board-level design can be more compact. On the other hand, redundant circuits can be further removed according to the excitation signal, frequency range, and impedance range required by the application scenarios. These optimizations can make the entire device more portable, and can even be made into a wearable device.
2. Further optimization of LIPUS devices: Further research may focus on the optimization of these devices for specific applications and patient populations. This includes improving the

design, manufacturing, and calibration processes to improve device performance, reliability, and user-friendliness. The development of wearable LIPUS devices can improve patient comfort and convenience while also enabling continuous therapy delivery and real-time monitoring of treatment progress, further expanding the applicability of LIPUS technology in various healthcare settings.

3. Design of dedicated electrodes for bioimpedance measurements: Future research can focus on the design and development of dedicated electrodes for the unique anatomical and physiological characteristics of various parts of the human body. These electrodes need to have more accurate, reliable, and comfortable bioimpedance measurement capabilities to improve detection accuracy. Meanwhile, the development of non-adhesive electrodes helps to achieve long-term impedance monitoring.

4. Develop a more unified and general IDE chip: In order to improve the performance and utility of EIS-based biosensors, future work should try to further study the design of IDE chips. These chips can be optimized for specific biomarker detection applications, further improving the accuracy of diagnostic tests. At the same time, the design of IDE chips should also consider the issue of mass production, so it is necessary to improve the yield rate and reduce costs.

5. Research on the synergy between bioimpedance and LIPUS technology: In this dissertation, there is no synergy between bioimpedance and LIPUS. Bioimpedance technology is a promising detection technique, while LIPUS is a potential treatment technique. The combination of the two is expected to construct a closed loop of treatment and detection. As previously mentioned, future studies could explore the potential benefits of combining bioimpedance and LIPUS techniques in improving diagnostic and therapeutic outcomes. This

interdisciplinary approach could lead to the development of innovative hybrid devices that exploit the strengths of each technology while addressing their limitations.

6. Expanded areas of application: Future work could explore the applicability of bioimpedance and LIPUS technology to a wider range of medical conditions and healthcare settings, including chronic disease management, preventive care, remote patient monitoring, and others.

7. Integration with telemedicine and remote monitoring platforms: With the development of telemedicine and remote patient monitoring, integrating bioimpedance and LIPUS devices with these platforms can provide valuable opportunities to improve patient care and outcomes. This integration could allow healthcare providers to monitor patient progress remotely and capture patient data over time, paving the way to personalized treatment plans and adaptive algorithms. These personalized approaches may optimize treatment outcomes by tailoring device settings and treatment parameters to individual patients. Moreover, data-driven treatment decisions and customization of treatment parameters can lead to more efficient and effective healthcare delivery.

In summary, the research presented in this dissertation has contributed to the advancement of the field of portable and wearable biomedical devices for pre-diagnosis, detection, and treatment. The bioimpedance and LIPUS technologies explored in this work hold promise for improving patient care and outcomes across a wide range of medical conditions and healthcare settings. Building up the findings, designs, and innovations presented in this dissertation, future work can continue to push the boundaries of biomedical devices, ultimately enhancing the quality, accessibility, and efficiency of healthcare delivery for patients.

References

- [1] L. Lu *et al.*, "Wearable health devices in health care: narrative systematic review," *JMIR mHealth and uHealth*, vol. 8, no. 11, p. e18907, 2020.
- [2] H. C. Koydemir and A. Ozcan, "Wearable and implantable sensors for biomedical applications," *Annual Review of Analytical Chemistry*, vol. 11, pp. 127-146, 2018.
- [3] V. Gubala, L. F. Harris, A. J. Ricco, M. X. Tan, and D. E. Williams, "Point of care diagnostics: status and future," *Analytical Chemistry*, vol. 84, no. 2, pp. 487-515, 2012.
- [4] Z. U. Ahmed, M. G. Mortuza, M. J. Uddin, M. H. Kabir, M. Mahiuddin, and M. J. Hoque, "Internet of Things based patient health monitoring system using wearable biomedical device," in *2018 International Conference on Innovation in Engineering and Technology (ICIET)*, 2018: IEEE, pp. 1-5.
- [5] J. Casselman, N. Onopa, and L. Khansa, "Wearable healthcare: Lessons from the past and a peek into the future," *Telematics and Informatics*, vol. 34, no. 7, pp. 1011-1023, 2017.
- [6] A. E. Omer *et al.*, "Low-cost portable microwave sensor for non-invasive monitoring of blood glucose level: Novel design utilizing a four-cell CSRR hexagonal configuration," *Scientific Reports*, vol. 10, no. 1, pp. 1-20, 2020.
- [7] H. Sohrabi *et al.*, "State-of-the-art cancer biomarker detection by portable (Bio) sensing technology: A critical review," *Microchemical Journal*, p. 107248, 2022.
- [8] F. Sun *et al.*, "Ultrasensitive detection of prostate specific antigen using a personal glucose meter based on DNA-mediated immunoreaction," *Analyst*, vol. 144, no. 20, pp. 6019-6024, 2019.

- [9] X. Liu *et al.*, "Point-of-care assay of alkaline phosphatase enzymatic activity using a thermometer or temperature discoloration sticker as readout," *Analytical Chemistry*, vol. 91, no. 12, pp. 7943-7949, 2019.
- [10] S. M. Majd and A. Salimi, "Ultrasensitive flexible FET-type aptasensor for CA 125 cancer marker detection based on carboxylated multiwalled carbon nanotubes immobilized onto reduced graphene oxide film," *Analytica Chimica Acta*, vol. 1000, pp. 273-282, 2018.
- [11] J. Zhou *et al.*, "Portable detection of colorectal cancer SW620 cells by using a personal glucose meter," *Analytical Biochemistry*, vol. 577, pp. 110-116, 2019.
- [12] S. Kim *et al.*, "Label-free surface-enhanced Raman spectroscopy biosensor for on-site breast cancer detection using human tears," *ACS Applied Materials & Interfaces*, vol. 12, no. 7, pp. 7897-7904, 2020.
- [13] T.-H. Tzeng *et al.*, "A portable micro gas chromatography system for lung cancer associated volatile organic compound detection," *IEEE Journal of Solid-State Circuits*, vol. 51, no. 1, pp. 259-272, 2015.
- [14] C.-H. Chuang *et al.*, "Immunosensor for the ultrasensitive and quantitative detection of bladder cancer in point of care testing," *Biosensors and Bioelectronics*, vol. 84, pp. 126-132, 2016.
- [15] S. Raj and K. C. Ray, "A personalized point-of-care platform for real-time ECG monitoring," *IEEE Transactions on Consumer Electronics*, vol. 64, no. 4, pp. 452-460, 2018.

- [16] A. Ibaida and I. Khalil, "Wavelet-based ECG steganography for protecting patient confidential information in point-of-care systems," *IEEE Transactions on Biomedical Engineering*, vol. 60, no. 12, pp. 3322-3330, 2013.
- [17] R. De Michele and M. Furini, "Iot healthcare: Benefits, issues and challenges," in *Proceedings of the 5th EAI International Conference on Smart Objects and Technologies for Social Good*, 2019, pp. 160-164.
- [18] I. Ahmed, E. Balestrieri, and F. Lamonaca, "IoMT-based biomedical measurement systems for healthcare monitoring: A review," *Acta IMEKO*, vol. 10, no. 2, pp. 174-184, 2021.
- [19] J. Zhang, J. Xu, J. Lim, J. K. Nolan, H. Lee, and C. H. Lee, "Wearable glucose monitoring and implantable drug delivery systems for diabetes management," *Advanced Healthcare Materials*, vol. 10, no. 17, p. 2100194, 2021.
- [20] Y. Long, J. Li, F. Yang, J. Wang, and X. Wang, "Wearable and implantable electroceuticals for therapeutic electrostimulations," *Advanced science*, vol. 8, no. 8, p. 2004023, 2021.
- [21] S. Ananthanarayan, M. Sheh, A. Chien, H. Profita, and K. Siek, "Pt Viz: towards a wearable device for visualizing knee rehabilitation exercises," in *Proceedings of the SIGCHI Conference on Human Factors in Computing Systems*, 2013, pp. 1247-1250.
- [22] P. Hinrichs, J. C. Cagle, and J. E. Sanders, "A portable bioimpedance instrument for monitoring residual limb fluid volume in people with transtibial limb loss: a technical note," *Medical Engineering & Physics*, vol. 68, pp. 101-107, 2019.

- [23] J. R. Harvey and Y. Mendelson, "A portable sensor for skin bioimpedance measurements," *International Journal of Sensors and Sensor Networks*, vol. 7, no. 1, pp. 1-8, 2019.
- [24] R. P. Burns, J. Dunning, and M. J. Fu, "A low-cost bioimpedance phase angle monitor for portable electrical surface stimulation burn prevention," *IEEE Transactions on Circuits and Systems II: Express Briefs*, vol. 68, no. 4, pp. 1118-1122, 2020.
- [25] M. Grossi and B. Riccò, "Electrical impedance spectroscopy (EIS) for biological analysis and food characterization: A review," *Journal of Sensors and Sensor Systems*, vol. 6, no. 2, pp. 303-325, 2017.
- [26] O. G. Martinsen and S. Grimnes, *Bioimpedance and Bioelectricity Basics*. Academic press, 2011.
- [27] B. Cornish, "Bioimpedance analysis: scientific background," *Lymphatic Research and Biology*, vol. 4, no. 1, pp. 47-50, 2006.
- [28] D. D. Stupin *et al.*, "Bioimpedance spectroscopy: Basics and applications," *ACS Biomaterials Science & Engineering*, vol. 7, no. 6, pp. 1962-1986, 2021.
- [29] M. Y. Jaffrin and H. Morel, "Body fluid volumes measurements by impedance: A review of bioimpedance spectroscopy (BIS) and bioimpedance analysis (BIA) methods," *Medical Engineering & Physics*, vol. 30, no. 10, pp. 1257-1269, 2008.
- [30] M. D. Van Loan, P. Withers, J. Matthie, and P. L. Mayclin, "Use of bioimpedance spectroscopy to determine extracellular fluid, intracellular fluid, total body water, and fat-free mass," *Human Body Composition: In Vivo Methods, Models, and Assessment*, pp. 67-70, 1993.

- [31] J. Matthie *et al.*, "Analytic assessment of the various bioimpedance methods used to estimate body water," *Journal of Applied Physiology*, vol. 84, no. 5, pp. 1801-1816, 1998.
- [32] A. De Lorenzo, A. Andreoli, J. Matthie, and P. Withers, "Predicting body cell mass with bioimpedance by using theoretical methods: a technological review," *Journal of Applied Physiology*, vol. 82, no. 5, pp. 1542-1558, 1997.
- [33] B. Klösgen, C. Rümenapp, and B. Gleich, "Bioimpedance spectroscopy," *BetaSys: Systems Biology of Regulated Exocytosis in Pancreatic β -Cells*, pp. 241-271, 2011.
- [34] D. El Khaled, N. Castellano, J. Gazquez, R. G. Salvador, and F. Manzano-Agugliaro, "Cleaner quality control system using bioimpedance methods: a review for fruits and vegetables," *Journal of Cleaner Production*, vol. 140, pp. 1749-1762, 2017.
- [35] D. Kamat, A. P. Chavan, and P. Patil, "Bio-impedance measurement system for analysis of skin diseases," *International Journal of Application or Innovation in Engineering & Management*, vol. 3, no. 2, 2014.
- [36] P. Aberg, I. Nicander, J. Hansson, P. Geladi, U. Holmgren, and S. Ollmar, "Skin cancer identification using multifrequency electrical impedance-a potential screening tool," *IEEE Transactions on Biomedical Engineering*, vol. 51, no. 12, pp. 2097-2102, 2004.
- [37] F. Slinde, A. Grönberg, C.-P. Engström, L. Rossander-Hulthén, and S. Larsson, "Body composition by bioelectrical impedance predicts mortality in chronic obstructive pulmonary disease patients," *Respiratory Medicine*, vol. 99, no. 8, pp. 1004-1009, 2005.
- [38] A. Walter-Kroker, A. Kroker, M. Mattiucci-Guehlke, and T. Glaab, "A practical guide to bioelectrical impedance analysis using the example of chronic obstructive pulmonary disease," *Nutrition Journal*, vol. 10, no. 1, pp. 1-8, 2011.

- [39] T. Morimoto *et al.*, "A study of the electrical bio-impedance of tumors," *Journal of Investigative Surgery*, vol. 6, no. 1, pp. 25-32, 1993.
- [40] R. Gonzalez-Landaeta, O. Casas, and R. Pallas-Areny, "Heart rate detection from plantar bioimpedance measurements," *IEEE transactions on Biomedical Engineering*, vol. 55, no. 3, pp. 1163-1167, 2008.
- [41] S. Di Somma, B. De Berardinis, C. Bongiovanni, R. Marino, E. Ferri, and B. Alfei, "Use of BNP and bioimpedance to drive therapy in heart failure patients," *Congestive Heart Failure*, vol. 16, pp. S56-S61, 2010.
- [42] S. Di Somma, F. Vetrone, and A. S. Maisel, "Bioimpedance Vector Analysis (BIVA) for diagnosis and management of acute heart failure," *Current Emergency and Hospital Medicine Reports*, vol. 2, pp. 104-111, 2014.
- [43] S. Mansouri, S. Chabchoub, Y. Alharbi, A. Alshrouf, and J. Nebhen, "A Real - Time Heart Rate Detection Algorithm Based on Peripheral Electrical Bioimpedance," *IEEJ Transactions on Electrical and Electronic Engineering*, vol. 17, no. 7, pp. 1054-1060, 2022.
- [44] H. C. Lukaski, N. Vega Diaz, A. Talluri, and L. Nescolarde, "Classification of hydration in clinical conditions: indirect and direct approaches using bioimpedance," *Nutrients*, vol. 11, no. 4, p. 809, 2019.
- [45] F. Zhu, M. Kuhlmann, P. Kotanko, E. Seibert, E. Leonard, and N. Levin, "A method for the estimation of hydration state during hemodialysis using a calf bioimpedance technique," *Physiological Measurement*, vol. 29, no. 6, p. S503, 2008.

- [46] C. O'brien, A. Young, and M. Sawka, "Bioelectrical impedance to estimate changes in hydration status," *International Journal of Sports Medicine*, vol. 23, no. 05, pp. 361-366, 2002.
- [47] R. A. Oppliger and C. Bartok, "Hydration testing of athletes," *Sports Medicine*, vol. 32, pp. 959-971, 2002.
- [48] M. Y. Jaffrin, "Body composition determination by bioimpedance: an update," *Current Opinion in Clinical Nutrition & Metabolic Care*, vol. 12, no. 5, pp. 482-486, 2009.
- [49] J. R. Matthie, "Bioimpedance measurements of human body composition: critical analysis and outlook," *Expert Review of Medical Devices*, vol. 5, no. 2, pp. 239-261, 2008.
- [50] C. H. Ling *et al.*, "Accuracy of direct segmental multi-frequency bioimpedance analysis in the assessment of total body and segmental body composition in middle-aged adult population," *Clinical Nutrition*, vol. 30, no. 5, pp. 610-615, 2011.
- [51] P. Cotogni, T. Monge, M. Fadda, and A. De Francesco, "Bioelectrical impedance analysis for monitoring cancer patients receiving chemotherapy and home parenteral nutrition," *BMC Cancer*, vol. 18, pp. 1-11, 2018.
- [52] O. Grundmann, S. Yoon, and J. Williams, "The value of bioelectrical impedance analysis and phase angle in the evaluation of malnutrition and quality of life in cancer patients—a comprehensive review," *European Journal of Clinical Nutrition*, vol. 69, no. 12, pp. 1290-1297, 2015.
- [53] Z. Zhang, X. Li, J. Tian, J. Chen, and G. Gao, "A review: Application and research progress of bioimpedance in meat quality inspection," *Journal of Food Process Engineering*, vol. 45, no. 11, p. e14153, 2022.

- [54] T. Ćurić, N. Marušić Radovčić, T. Janči, I. Lacković, and S. Vidaček, "Salt and moisture content determination of fish by bioelectrical impedance and a needle-type multi-electrode array," *International Journal of Food Properties*, vol. 20, no. 11, pp. 2477-2486, 2017.
- [55] U. Pliquet, "Bioimpedance: a review for food processing," *Food Engineering Reviews*, vol. 2, pp. 74-94, 2010.
- [56] M. Rivola, P. Ibba, P. Lugli, and L. Petti, "Bioimpedance data statistical modelling for food quality classification and prediction," in *2021 IEEE International Symposium on Circuits and Systems (ISCAS)*, 2021: IEEE, pp. 1-5.
- [57] P. Ibba, A. Falco, B. D. Abera, G. Cantarella, L. Petti, and P. Lugli, "Bio-impedance and circuit parameters: An analysis for tracking fruit ripening," *Postharvest Biology and Technology*, vol. 159, p. 110978, 2020.
- [58] T. a. Prevc, B. Cigić, R. Vidrih, N. a. Poklar Ulrih, and N. a. Šegatin, "Correlation of basic oil quality indices and electrical properties of model vegetable oil systems," *Journal of Agricultural and Food Chemistry*, vol. 61, no. 47, pp. 11355-11362, 2013.
- [59] F. Ferrero, M. Valledor, and J. Campo, "Screening method for early detection of mastitis in cows," *Measurement*, vol. 47, pp. 855-860, 2014.
- [60] H. Kuttruff, *Ultrasonics: Fundamentals and Applications*. Springer Science & Business Media, 2012.
- [61] R. W. Wood and A. L. Loomis, "XXXVIII. The physical and biological effects of high-frequency sound-waves of great intensity," *The London, Edinburgh, and Dublin Philosophical Magazine and Journal of Science*, vol. 4, no. 22, pp. 417-436, 1927.

- [62] C. Rubin, M. Bolander, J. P. Ryaby, and M. Hadjiargyrou, "The use of low-intensity ultrasound to accelerate the healing of fractures," *JBJS*, vol. 83, no. 2, p. 259, 2001.
- [63] A. Fomenko, C. Neudorfer, R. F. Dallapiazza, S. K. Kalia, and A. M. Lozano, "Low-intensity ultrasound neuromodulation: an overview of mechanisms and emerging human applications," *Brain Stimulation*, vol. 11, no. 6, pp. 1209-1217, 2018.
- [64] J. Acheta, S. B. Stephens, S. Belin, and Y. Poitelon, "Therapeutic Low-Intensity Ultrasound for Peripheral Nerve Regeneration—A Schwann Cell Perspective," *Frontiers in Cellular Neuroscience*, vol. 15, p. 544, 2022.
- [65] A. K. Wood and C. M. Sehgal, "A review of low-intensity ultrasound for cancer therapy," *Ultrasound in Medicine & Biology*, vol. 41, no. 4, pp. 905-928, 2015.
- [66] K. Beccaria, M. Canney, G. Bouchoux, S. Puget, J. Grill, and A. Carpentier, "Blood-brain barrier disruption with low-intensity pulsed ultrasound for the treatment of pediatric brain tumors: A review and perspectives," *Neurosurgical Focus*, vol. 48, no. 1, p. E10, 2020.
- [67] D. Gebauer, E. Mayr, E. Orthner, and J. P. Ryaby, "Low-intensity pulsed ultrasound: effects on nonunions," *Ultrasound in Medicine & Biology*, vol. 31, no. 10, pp. 1391-1402, 2005.
- [68] S. Zhou, A. Schmelz, T. Seufferlein, Y. Li, J. Zhao, and M. G. Bachem, "Molecular mechanisms of low intensity pulsed ultrasound in human skin fibroblasts," *Journal of Biological Chemistry*, vol. 279, no. 52, pp. 54463-54469, 2004.
- [69] N. M. Pounder and A. J. Harrison, "Low intensity pulsed ultrasound for fracture healing: a review of the clinical evidence and the associated biological mechanism of action," *Ultrasonics*, vol. 48, no. 4, pp. 330-338, 2008.

- [70] M. Marrelli *et al.*, "Dental pulp stem cell mechanoresponsiveness: effects of mechanical stimuli on dental pulp stem cell behavior," *Frontiers in Physiology*, vol. 9, p. 1685, 2018.
- [71] P. Palanisamy, M. Alam, S. Li, S. K. Chow, and Y. P. Zheng, "Low - Intensity Pulsed Ultrasound Stimulation for Bone Fractures Healing: A Review," *Journal of Ultrasound in Medicine*, vol. 41, no. 3, pp. 547-563, 2022.
- [72] S. Manaka *et al.*, "Low-intensity pulsed ultrasound-induced ATP increases bone formation via the P2X7 receptor in osteoblast-like MC3T3-E1 cells," *FEBS Letters*, vol. 589, no. 3, pp. 310-318, 2015.
- [73] G. Lin, A. B. Reed-Maldonado, M. Lin, Z. Xin, and T. F. Lue, "Effects and mechanisms of low-intensity pulsed ultrasound for chronic prostatitis and chronic pelvic pain syndrome," *International Journal of Molecular Sciences*, vol. 17, no. 7, p. 1057, 2016.
- [74] L. Claes and B. Willie, "The enhancement of bone regeneration by ultrasound," *Progress in Biophysics and Molecular Biology*, vol. 93, no. 1-3, pp. 384-398, 2007.
- [75] F. Padilla, R. Puts, L. Vico, and K. Raum, "Stimulation of bone repair with ultrasound: a review of the possible mechanic effects," *Ultrasonics*, vol. 54, no. 5, pp. 1125-1145, 2014.
- [76] J.-C. Wang and Y. Zhou, "Suppressing bubble shielding effect in shock wave lithotripsy by low intensity pulsed ultrasound," *Ultrasonics*, vol. 55, pp. 65-74, 2015.
- [77] M. S. Karthikesh and X. Yang, "The effect of ultrasound cavitation on endothelial cells," *Experimental Biology and Medicine*, vol. 246, no. 7, pp. 758-770, 2021.
- [78] Y. Tabuchi *et al.*, "Identification of genes responsive to low intensity pulsed ultrasound in a human leukemia cell line Molt-4," *Cancer Letters*, vol. 246, no. 1-2, pp. 149-156, 2007.

- [79] R. Mundi, S. Petis, R. Kaloty, V. Shetty, and M. Bhandari, "Low-intensity pulsed ultrasound: Fracture healing," *Indian Journal of Orthopaedics*, vol. 43, no. 2, p. 132, 2009.
- [80] O. Altland, D. Dalecki, V. Suchkova, and C. Francis, "Low-intensity ultrasound increases endothelial cell nitric oxide synthase activity and nitric oxide synthesis," *Journal of Thrombosis and Haemostasis*, vol. 2, no. 4, pp. 637-643, 2004.
- [81] V. N. Suchkova, R. B. Baggs, S. K. Sahni, and C. W. Francis, "Ultrasound improves tissue perfusion in ischemic tissue through a nitric oxide dependent mechanism," *Thrombosis and Haemostasis*, vol. 88, no. 11, pp. 865-870, 2002.
- [82] K. Eguchi *et al.*, "Whole-brain low-intensity pulsed ultrasound therapy markedly improves cognitive dysfunctions in mouse models of dementia-Crucial roles of endothelial nitric oxide synthase," *Brain Stimulation*, vol. 11, no. 5, pp. 959-973, 2018.
- [83] P. Reher, M. Harris, M. Whiteman, H. Hai, and S. Meghji, "Ultrasound stimulates nitric oxide and prostaglandin E2 production by human osteoblasts," *Bone*, vol. 31, no. 1, pp. 236-241, 2002.
- [84] Y. Kang *et al.*, "Tumor vasodilation by N-Heterocyclic carbene-based nitric oxide delivery triggered by high-intensity focused ultrasound and enhanced drug homing to tumor sites for anti-cancer therapy," *Biomaterials*, vol. 217, p. 119297, 2019.
- [85] S. B. Tajali, P. Houghton, J. C. MacDermid, and R. Grewal, "Effects of low-intensity pulsed ultrasound therapy on fracture healing: a systematic review and meta-analysis," *American Journal of Physical Medicine & Rehabilitation*, vol. 91, no. 4, pp. 349-367, 2012.

- [86] R. Leighton, J. T. Watson, P. Giannoudis, C. Papakostidis, A. Harrison, and R. G. Steen, "Healing of fracture nonunions treated with low-intensity pulsed ultrasound (LIPUS): a systematic review and meta-analysis," *Injury*, vol. 48, no. 7, pp. 1339-1347, 2017.
- [87] M. Bayat, A. Viridi, R. Jalalifirouzkouhi, and F. Rezaei, "Comparison of effects of LLLT and LIPUS on fracture healing in animal models and patients: A systematic review," *Progress in Biophysics and Molecular Biology*, vol. 132, pp. 3-22, 2018.
- [88] K.-S. Leung, W.-S. Lee, H.-F. Tsui, P. P.-L. Liu, and W.-H. Cheung, "Complex tibial fracture outcomes following treatment with low-intensity pulsed ultrasound," *Ultrasound in Medicine & Biology*, vol. 30, no. 3, pp. 389-395, 2004.
- [89] G. J. Della Rocca, "The science of ultrasound therapy for fracture healing," *Indian Journal of Orthopaedics*, vol. 43, no. 2, p. 121, 2009.
- [90] Z. Xin, G. Lin, H. Lei, T. F. Lue, and Y. Guo, "Clinical applications of low-intensity pulsed ultrasound and its potential role in urology," *Translational Andrology and Urology*, vol. 5, no. 2, p. 255, 2016.
- [91] U. Farkash, O. Bain, A. Gam, M. Nyska, and P. Sagiv, "Low-intensity pulsed ultrasound for treating delayed union scaphoid fractures: case series," *Journal of Orthopaedic Surgery and Research*, vol. 10, pp. 1-7, 2015.
- [92] W. C. Lai, B. C. Iglesias, B. J. Mark, and D. Wang, "Low-Intensity Pulsed Ultrasound Augments Tendon, Ligament, and Bone–Soft Tissue Healing in Preclinical Animal Models: A Systematic Review," *Arthroscopy: The Journal of Arthroscopic & Related Surgery*, vol. 37, no. 7, pp. 2318-2333. e3, 2021.

- [93] A. Khanna, R. T. Nelmes, N. Gougoulis, N. Maffulli, and J. Gray, "The effects of LIPUS on soft-tissue healing: a review of literature," *British Medical Bulletin*, vol. 89, no. 1, pp. 169-182, 2009.
- [94] C. S. Enwemeka, O. Rodriguez, and S. Mendosa, "The biomechanical effects of low-intensity ultrasound on healing tendons," *Ultrasound in Medicine & Biology*, vol. 16, no. 8, pp. 801-807, 1990.
- [95] A. R. Hsu and G. B. Holmes, "Preliminary treatment of Achilles tendinopathy using low-intensity pulsed ultrasound," *Foot & Ankle Specialist*, vol. 9, no. 1, pp. 52-57, 2016.
- [96] Y. Takakura *et al.*, "Low - intensity pulsed ultrasound enhances early healing of medial collateral ligament injuries in rats," *Journal of Ultrasound in Medicine*, vol. 21, no. 3, pp. 283-288, 2002.
- [97] M. Xu *et al.*, "Review on experimental study and clinical application of low-intensity pulsed ultrasound in inflammation," *Quantitative Imaging in Medicine and Surgery*, vol. 11, no. 1, p. 443, 2021.
- [98] A. Binder, G. Hodge, A. Greenwood, B. Hazleman, and D. P. Thomas, "Is therapeutic ultrasound effective in treating soft tissue lesions?," *Br Med J (Clin Res Ed)*, vol. 290, no. 6467, pp. 512-514, 1985.
- [99] M. ElHag, K. Coghlan, P. Christmas, W. Harvey, and M. Harris, "The anti-inflammatory effects of dexamethasone and therapeutic ultrasound in oral surgery," *British Journal of Oral and Maxillofacial Surgery*, vol. 23, no. 1, pp. 17-23, 1985.
- [100] I. Hashish, W. Harvey, and M. Harris, "Anti-inflammatory effects of ultrasound therapy: evidence for a major placebo effect," *Rheumatology*, vol. 25, no. 1, pp. 77-81, 1986.

- [101] J. Engelmann *et al.*, "Pulsed ultrasound and dimethylsulfoxide gel treatment reduces the expression of pro-inflammatory molecules in an animal model of muscle injury," *Ultrasound in Medicine & Biology*, vol. 38, no. 8, pp. 1470-1475, 2012.
- [102] K. Nagata, T. Nakamura, S. Fujihara, and E. Tanaka, "Ultrasound modulates the inflammatory response and promotes muscle regeneration in injured muscles," *Annals of Biomedical Engineering*, vol. 41, pp. 1095-1105, 2013.
- [103] T. Nakamura, S. Fujihara, K. Yamamoto-Nagata, T. Katsura, T. Inubushi, and E. Tanaka, "Low-intensity pulsed ultrasound reduces the inflammatory activity of synovitis," *Annals of Biomedical Engineering*, vol. 39, pp. 2964-2971, 2011.
- [104] J.-I. Chung, S. Barua, B. Choi, B.-H. Min, H. Han, and E. Baik, "Anti-inflammatory effect of low intensity ultrasound (LIUS) on complete Freund's adjuvant-induced arthritis synovium," *Osteoarthritis and Cartilage*, vol. 20, no. 4, pp. 314-322, 2012.
- [105] X. Liu, D. Zou, Y. Hu, Y. He, and J. Lu, "Research progress of low-intensity pulsed ultrasound in the repair of peripheral nerve injury," *Tissue Engineering Part B: Reviews*, 2023.
- [106] D.-Y. Peng, A. B. Reed-Maldonado, G.-T. Lin, S.-J. Xia, and T. F. Lue, "Low-intensity pulsed ultrasound for regenerating peripheral nerves: potential for penile nerve," *Asian Journal of Andrology*, vol. 22, no. 4, p. 335, 2020.
- [107] P. R. Haffey *et al.*, "The regenerative potential of therapeutic ultrasound on neural tissue: a pragmatic review," *Pain Medicine*, vol. 21, no. 7, pp. 1494-1506, 2020.
- [108] A. R. Crisci and A. L. Ferreira, "Low-intensity pulsed ultrasound accelerates the regeneration of the sciatic nerve after neurotomy in rats," *Ultrasound in Medicine & Biology*, vol. 28, no. 10, pp. 1335-1341, 2002.

- [109] Y. H. Tsuang *et al.*, "Effects of low intensity pulsed ultrasound on rat Schwann cells metabolism," *Artificial Organs*, vol. 35, no. 4, pp. 373-383, 2011.
- [110] Y. Yue *et al.*, "Low - intensity pulsed ultrasound upregulates pro - myelination indicators of Schwann cells enhanced by co - culture with adipose - derived stem cells," *Cell Proliferation*, vol. 49, no. 6, pp. 720-728, 2016.
- [111] M. Sato, M. Motoyoshi, M. Shinoda, K. Iwata, and N. Shimizu, "Low - intensity pulsed ultrasound accelerates nerve regeneration following inferior alveolar nerve transection in rats," *European Journal of Oral Sciences*, vol. 124, no. 3, pp. 246-250, 2016.
- [112] W. Jiang *et al.*, "Low-intensity pulsed ultrasound treatment improved the rate of autograft peripheral nerve regeneration in rat," *Scientific Reports*, vol. 6, no. 1, p. 22773, 2016.
- [113] T. Yamaguchi *et al.*, "Current landscape of sonodynamic therapy for treating cancer," *Cancers*, vol. 13, no. 24, p. 6184, 2021.
- [114] Z. h. Jin *et al.*, "Combination effect of photodynamic and sonodynamic therapy on experimental skin squamous cell carcinoma in C3H/HeN mice," *The Journal of Dermatology*, vol. 27, no. 5, pp. 294-306, 2000.
- [115] W. Lopez *et al.*, "Ultrasound therapy, chemotherapy and their combination for prostate cancer," *Technology in Cancer Research & Treatment*, vol. 20, p. 15330338211011965, 2021.
- [116] T. Yu, J. Bai, K. Hu, and Z. Wang, "Biological effects of ultrasound exposure on adriamycin-resistant and cisplatin-resistant human ovarian carcinoma cell lines in vitro," *Ultrasonics Sonochemistry*, vol. 11, no. 2, pp. 89-94, 2004.

- [117] H. Li, H. Fan, Z. Wang, J. Zheng, and W. Cao, "Potentiation of scutellarin on human tongue carcinoma xenograft by low-intensity ultrasound," *PloS one*, vol. 8, no. 3, p. e59473, 2013.
- [118] L. B. Feril Jr, R. Ogawa, K. Tachibana, and T. Kondo, "Optimized ultrasound - mediated gene transfection in cancer cells," *Cancer Science*, vol. 97, no. 10, pp. 1111-1114, 2006.
- [119] N. A. Geis, H. A. Katus, and R. Bekeredjian, "Microbubbles as a vehicle for gene and drug delivery: current clinical implications and future perspectives," *Current Pharmaceutical Design*, vol. 18, no. 15, pp. 2166-2183, 2012.
- [120] H. Liang, J. Tang, and M. Halliwell, "Sonoporation, drug delivery, and gene therapy," *Proceedings of the Institution of Mechanical Engineers, Part H: Journal of Engineering in Medicine*, vol. 224, no. 2, pp. 343-361, 2010.
- [121] S. R. Sirsi and M. A. Borden, "Advances in ultrasound mediated gene therapy using microbubble contrast agents," *Theranostics*, vol. 2, no. 12, p. 1208, 2012.
- [122] T. E. Hewett *et al.*, "Biomechanical measures of neuromuscular control and valgus loading of the knee predict anterior cruciate ligament injury risk in female athletes: a prospective study," *The American Journal of Sports Medicine*, vol. 33, no. 4, pp. 492-501, 2005.
- [123] F. Margheritini, J. Rihn, V. Musahl, P. P. Mariani, and C. Harner, "Posterior cruciate ligament injuries in the athlete," *Sports Medicine*, vol. 32, no. 6, pp. 393-408, 2002.
- [124] M. A. Hopper and A. J. Grainger, "Knee Injuries," in *Essential Radiology for Sports Medicine*, P. Robinson Ed. New York, NY: Springer New York, 2010, pp. 1-28.
- [125] D. T. Felson, A. Naimark, J. Anderson, L. Kazis, W. Castelli, and R. F. Meenan, "The prevalence of knee osteoarthritis in the elderly. The Framingham Osteoarthritis Study,"

- Arthritis & Rheumatism: Official Journal of the American College of Rheumatology*, vol. 30, no. 8, pp. 914-918, 1987.
- [126] A. D. Woolf and B. Pflieger, "Burden of major musculoskeletal conditions," *Bulletin of the World Health Organization*, vol. 81, pp. 646-656, 2003.
- [127] B. H. Sun, C. W. Wu, and K. C. Kalunian, "New developments in osteoarthritis," *Rheumatic Disease Clinics of North America*, vol. 33, no. 1, pp. 135-148, 2007.
- [128] P. Ben-Galim, E. L. Steinberg, H. Amir, N. Ash, S. Dekel, and R. Arbel, "Accuracy of Magnetic Resonance Imaging of the Knee and Unjustified Surgery," *Clinical Orthopaedics and Related Research®*, vol. 447, pp. 100-104, 2006, doi: 10.1097/01.blo.0000203471.50808.b7.
- [129] G. W. Woods, R. F. Stanley JR, and H. S. Tullos, "Lateral capsular sign: x-ray clue to a significant knee instability," *The American Journal of Sports Medicine*, vol. 7, no. 1, pp. 27-33, 1979.
- [130] L. Friedman, K. Finlay, and E. Jurriaans, "Ultrasound of the knee," *Skeletal Radiology*, vol. 30, no. 7, pp. 361-377, 2001.
- [131] M. Lequesne, C. Mery, M. Samson, and P. Gerard, "Indexes of severity for osteoarthritis of the hip and knee: validation—value in comparison with other assessment tests," *Scandinavian Journal of Rheumatology*, vol. 16, no. sup65, pp. 85-89, 1987.
- [132] N. Bellamy, W. W. Buchanan, C. H. Goldsmith, J. Campbell, and L. W. Stitt, "Validation study of WOMAC: a health status instrument for measuring clinically important patient relevant outcomes to antirheumatic drug therapy in patients with osteoarthritis of the hip or knee," *Journal of Rheumatology*, 1988.

- [133] J. Lysholm and J. Gillquist, "Evaluation of knee ligament surgery results with special emphasis on use of a scoring scale," *The American Journal of Sports Medicine*, vol. 10, no. 3, pp. 150-154, 1982.
- [134] E. B. Neves, A. V. Pino, R. M. V. R. De Almeida, and M. N. De Souza, "Knee bioelectric impedance assessment in healthy/with osteoarthritis subjects," *Physiological Measurement*, vol. 31, no. 2, p. 207, 2009.
- [135] Z. Zhang, S. Barman, and G. Christopher, "The role of protein content on the steady and oscillatory shear rheology of model synovial fluids," *Soft Matter*, vol. 10, no. 32, pp. 5965-5973, 2014.
- [136] S. Sutton *et al.*, "The contribution of the synovium, synovial derived inflammatory cytokines and neuropeptides to the pathogenesis of osteoarthritis," *The Veterinary Journal*, vol. 179, no. 1, pp. 10-24, 2009.
- [137] S. Gabriel, R. Lau, and C. Gabriel, "The dielectric properties of biological tissues: II. Measurements in the frequency range 10 Hz to 20 GHz," *Physics in Medicine & Biology*, vol. 41, no. 11, p. 2251, 1996.
- [138] T. A. Blackburn and E. Craig, "Knee anatomy: a brief review," *Physical Therapy*, vol. 60, no. 12, pp. 1556-1560, 1980.
- [139] L. Goldman and D. A. Ausiello, *Cecil medicine*. Saunders Elsevier Philadelphia, 2008.
- [140] Z. Meyler, "Knee Anatomy," ed: Arthritis-Health, 2018.
- [141] H. Heilmann, K. Lindenhayn, and H. Walther, "Synovial volume of healthy and arthrotic human knee joints," *Zeitschrift fur Orthopadie und ihre Grenzgebiete*, vol. 134, no. 2, pp. 144-148, 1996.

- [142] V. B. Kraus, T. V. Stabler, S. Kong, G. Varju, and G. McDaniel, "Measurement of synovial fluid volume using urea," *Osteoarthritis and Cartilage*, vol. 15, no. 10, pp. 1217-1220, 2007.
- [143] S. Gabriel, R. Lau, and C. Gabriel, "The dielectric properties of biological tissues: III. Parametric models for the dielectric spectrum of tissues," *Physics in Medicine & Biology*, vol. 41, no. 11, p. 2271, 1996.
- [144] P. L. Nunez and R. Srinivasan, *Electric fields of the brain: the neurophysics of EEG*. Oxford University Press, USA, 2006.
- [145] C. Bédard, H. Kröger, and A. Destexhe, "Modeling extracellular field potentials and the frequency-filtering properties of extracellular space," *Biophysical Journal*, vol. 86, no. 3, pp. 1829-1842, 2004.
- [146] V. Vestergaard, A. B. Pedersen, P. T. Tengberg, A. Troelsen, and H. M. Schröder, "20-year trends of distal femoral, patellar, and proximal tibial fractures: a Danish nationwide cohort study of 60,823 patients," *Acta Orthopaedica*, vol. 91, no. 1, pp. 109-114, 2020.
- [147] M. Galla and P. Lobenhoffer, "Patella fractures," *Der Chirurg; Zeitschrift für Alle Gebiete der Operativen Medizin*, vol. 76, no. 10, pp. 987-97; quiz 998, 2005.
- [148] OrthoInfo, "Patellar (Kneecap) Fractures," *American Academy of Orthopaedic Surgeon*, January 2017. [Online]. Available: <https://orthoinfo.aaos.org/en/diseases--conditions/patellar-kneecap-fractures/>.
- [149] G. L. Sternbach, "Evaluation of the knee," *The Journal of Emergency Medicine*, vol. 4, no. 2, pp. 133-143, 1986.
- [150] J. S. Everhart, J. H. Sojka, C. C. Kaeding, A. L. Bertone, and D. C. Flanigan, "The ACL injury response: A collagen-based analysis," *The Knee*, vol. 24, no. 3, pp. 601-607, 2017.

- [151] N. Maffulli, P. Binfield, J. King, and C. Good, "Acute haemarthrosis of the knee in athletes. A prospective study of 106 cases," *The Journal of Bone and Joint Surgery. British volume*, vol. 75, no. 6, pp. 945-949, 1993.
- [152] D. J. Mathison and S. J. Teach, "Approach to knee effusions," *Pediatric Emergency Care*, vol. 25, no. 11, pp. 773-786, 2009.
- [153] M. B. Goldring and M. Otero, "Inflammation in osteoarthritis," *Current Opinion in Rheumatology*, vol. 23, no. 5, p. 471, 2011.
- [154] Q. Guo, Y. Wang, D. Xu, J. Nossent, N. J. Pavlos, and J. Xu, "Rheumatoid arthritis: pathological mechanisms and modern pharmacologic therapies," *Bone Research*, vol. 6, no. 1, pp. 1-14, 2018.
- [155] D. Wirtz, M. Marth, O. Miltner, U. Schneider, and K. Zilkens, "Septic arthritis of the knee in adults: treatment by arthroscopy or arthrotomy," *International Orthopaedics*, vol. 25, no. 4, pp. 239-241, 2001.
- [156] Y.-H. Pua, "The time course of knee swelling post total knee arthroplasty and its associations with quadriceps strength and gait speed," *The Journal of Arthroplasty*, vol. 30, no. 7, pp. 1215-1219, 2015.
- [157] C. Pichonnaz, J.-P. Bassin, E. Lécureux, D. Currat, and B. M. Jolles, "Bioimpedance spectroscopy for swelling evaluation following total knee arthroplasty: a validation study," *BMC Musculoskeletal Disorders*, vol. 16, no. 1, pp. 1-8, 2015.
- [158] C. Pichonnaz, J. P. Bassin, D. Currat, E. Martin, and B. M. Jolles, "Bioimpedance for oedema evaluation after total knee arthroplasty," *Physiotherapy Research International*, vol. 18, no. 3, pp. 140-147, 2013.

- [159] S. Hersek *et al.*, "Wearable vector electrical bioimpedance system to assess knee joint health," *IEEE Transactions on Biomedical Engineering*, vol. 64, no. 10, pp. 2353-2360, 2016.
- [160] A. A. Al-Ali, B. J. Maundy, and A. S. Elwakil, "Bio-impedance measurement and applications," in *Design and Implementation of Portable Impedance Analyzers*: Springer, 2019, pp. 1-14.
- [161] H. Abdi and L. J. Williams, "Principal component analysis," *Wiley Interdisciplinary Reviews: Computational Statistics*, vol. 2, no. 4, pp. 433-459, 2010.
- [162] C.-C. Chang and C.-J. Lin, "LIBSVM: a library for support vector machines," *ACM Transactions on Intelligent Systems and Technology (TIST)*, vol. 2, no. 3, pp. 1-27, 2011.
- [163] P. Deadman, K. Baker, and M. Al-Khafaji, "A Manual of Acupuncture: Journal of Chinese Medicine Publications," *Ann Arbor, MI: Cushing Mallory*, pp. 376-80, 2001.
- [164] S. Fenn, A. Datir, and A. Saifuddin, "Synovial recesses of the knee: MR imaging review of anatomical and pathological features," *Skeletal Radiology*, vol. 38, pp. 317-328, 2009.
- [165] S. Affatato, *Surgical Techniques in Total Knee Arthroplasty and Alternative Procedures*. Elsevier, 2014.
- [166] X. Ye *et al.*, "Bioimpedance measurement of knee injuries using bipolar electrode configuration," *IEEE Transactions on Biomedical Circuits and Systems*, vol. 16, no. 5, pp. 962-971, 2022.
- [167] R. P. Areny, "Tetrapolar bioimpedance measurements compared to four-wire resistance measurements," *Journal of Electrical Bioimpedance*, vol. 9, no. 1, pp. 1-2, 2018.
- [168] B. Brown, A. Wilson, and P. Bertemes-Filho, "Bipolar and tetrapolar transfer impedance measurements from volume conductor," *Electronics Letters*, vol. 36, no. 25, p. 1, 2000.

- [169] S. Grimnes and Ø. G. Martinsen, "Sources of error in tetrapolar impedance measurements on biomaterials and other ionic conductors," *Journal of Physics D: Applied Physics*, vol. 40, no. 1, p. 9, 2006.
- [170] M. Fernandez and R. Pallas-Areny, "Ag-AgCl electrode noise in high-resolution ECG measurements," *Biomedical Instrumentation & Technology*, vol. 34, no. 2, pp. 125-130, 2000.
- [171] Y. M. Chi, T.-P. Jung, and G. Cauwenberghs, "Dry-contact and noncontact biopotential electrodes: Methodological review," *IEEE Reviews in Biomedical Engineering*, vol. 3, pp. 106-119, 2010.
- [172] D. J. Hewson, J.-Y. Hogrel, Y. Langeron, and J. Duchêne, "Evolution in impedance at the electrode-skin interface of two types of surface EMG electrodes during long-term recordings," *Journal of Electromyography and Kinesiology*, vol. 13, no. 3, pp. 273-279, 2003.
- [173] C. Sidebottom, H. Rudolph, M. Schmidt, and L. Eisner, "IEC 60601-1—the third edition," *Journal of Medical Device Regulation-May*, vol. 9, 2006.
- [174] D. S. Jevsevar *et al.*, "The American Academy of Orthopaedic Surgeons evidence-based guideline on: treatment of osteoarthritis of the knee," *JBJS*, vol. 95, no. 20, pp. 1885-1886, 2013.
- [175] K. G. Shea *et al.*, "Management of anterior cruciate ligament injuries," *J Bone Joint Surg Am*, vol. 97, no. 8, pp. 672-676, 2015.
- [176] A. Searle and L. Kirkup, "Real time impedance plots with arbitrary frequency components," *Physiological Measurement*, vol. 20, no. 1, p. 103, 1999/02/01 1999, doi: 10.1088/0967-3334/20/1/008.

- [177] Z. Jiang *et al.*, "Development of a portable electrochemical impedance spectroscopy system for bio-detection," *IEEE Sensors Journal*, vol. 19, no. 15, pp. 5979-5987, 2019.
- [178] N. Meziane, J. Webster, M. Attari, and A. Nimunkar, "Dry electrodes for electrocardiography," *Physiological Measurement*, vol. 34, no. 9, p. R47, 2013.
- [179] R. Kusche, S. Kaufmann, and M. Ryschka, "Dry electrodes for bioimpedance measurements—Design, characterization and comparison," *Biomedical Physics & Engineering Express*, vol. 5, no. 1, p. 015001, 2018.
- [180] S. L. Colyer and P. M. McGuigan, "Textile electrodes embedded in clothing: A practical alternative to traditional surface electromyography when assessing muscle excitation during functional movements," *Journal of Sports Science & Medicine*, vol. 17, no. 1, p. 101, 2018.
- [181] A. Ankhili, X. Tao, C. Cochrane, D. Coulon, and V. Koncar, "Washable and reliable textile electrodes embedded into underwear fabric for electrocardiography (ECG) monitoring," *Materials*, vol. 11, no. 2, p. 256, 2018.
- [182] J.-Y. Baek, J.-H. An, J.-M. Choi, K.-S. Park, and S.-H. Lee, "Flexible polymeric dry electrodes for the long-term monitoring of ECG," *Sensors and Actuators A: Physical*, vol. 143, no. 2, pp. 423-429, 2008.
- [183] G. Iacobucci, "Pandemic has accelerated demand for private healthcare, report finds," ed: British Medical Journal Publishing Group, 2022.
- [184] G. J. Kost, "Guidelines for point-of-care testing. Improving patient outcomes," *American Journal of Clinical Pathology*, vol. 104, no. 4 Suppl 1, pp. S111-27, 1995.

- [185] P. B. Luppá, C. Müller, A. Schlichtiger, and H. Schlebusch, "Point-of-care testing (POCT): Current techniques and future perspectives," *TrAC Trends in Analytical Chemistry*, vol. 30, no. 6, pp. 887-898, 2011.
- [186] S. Kumar *et al.*, "Microfluidic - integrated biosensors: Prospects for point - of - care diagnostics," *Biotechnology Journal*, vol. 8, no. 11, pp. 1267-1279, 2013.
- [187] S. Choi, M. Goryll, L. Y. M. Sin, P. K. Wong, and J. Chae, "Microfluidic-based biosensors toward point-of-care detection of nucleic acids and proteins," *Microfluidics and Nanofluidics*, vol. 10, pp. 231-247, 2011.
- [188] P. A. Keahey *et al.*, "Point-of-care device to diagnose and monitor neonatal jaundice in low-resource settings," *Proceedings of the National Academy of Sciences*, vol. 114, no. 51, pp. E10965-E10971, 2017.
- [189] J. H. Soh, H.-M. Chan, and J. Y. Ying, "Strategies for developing sensitive and specific nanoparticle-based lateral flow assays as point-of-care diagnostic device," *Nano Today*, vol. 30, p. 100831, 2020.
- [190] J. Chen, Y. Feng, and S. MacKay, *Bionanotechnology: Engineering Concepts and Applications*. McGraw-Hill Education, 2022.
- [191] C. Ma, N. M. Contento, L. R. Gibson, and P. W. Bohn, "Redox cycling in nanoscale-recessed ring-disk electrode arrays for enhanced electrochemical sensitivity," *Acs Nano*, vol. 7, no. 6, pp. 5483-5490, 2013.
- [192] S. M. Radke and E. C. Alcocilja, "Design and fabrication of a microimpedance biosensor for bacterial detection," *IEEE Sensors Journal*, vol. 4, no. 4, pp. 434-440, 2004.

- [193] M. Varshney and Y. Li, "Interdigitated array microelectrodes based impedance biosensors for detection of bacterial cells," *Biosensors and bioelectronics*, vol. 24, no. 10, pp. 2951-2960, 2009.
- [194] N. Couniot, D. Flandre, L. Francis, and A. Afzalian, "Signal-to-noise ratio optimization for detecting bacteria with interdigitated microelectrodes," *Sensors and Actuators B: Chemical*, vol. 189, pp. 43-51, 2013.
- [195] N. G. Green, A. Ramos, and H. Morgan, "Numerical solution of the dielectrophoretic and travelling wave forces for interdigitated electrode arrays using the finite element method," *Journal of Electrostatics*, vol. 56, no. 2, pp. 235-254, 2002.
- [196] M. Ibrahim, J. Claudel, D. Kourtiche, and M. Nadi, "Geometric parameters optimization of planar interdigitated electrodes for bioimpedance spectroscopy," *Journal of Electrical Bioimpedance*, vol. 4, no. 1, pp. 13-22, 2013.
- [197] M. A. Ortega *et al.*, "Muscle-on-a-chip with an on-site multiplexed biosensing system for in situ monitoring of secreted IL-6 and TNF- α ," *Lab on a Chip*, vol. 19, no. 15, pp. 2568-2580, 2019.
- [198] L. Wang, M. Veselinovic, L. Yang, B. J. Geiss, D. S. Dandy, and T. Chen, "A sensitive DNA capacitive biosensor using interdigitated electrodes," *Biosensors and Bioelectronics*, vol. 87, pp. 646-653, 2017.
- [199] M. Xu, R. Wang, and Y. Li, "Rapid detection of Escherichia coli O157: H7 and Salmonella Typhimurium in foods using an electrochemical immunosensor based on screen-printed interdigitated microelectrode and immunomagnetic separation," *Talanta*, vol. 148, pp. 200-208, 2016.

- [200] G. Zhou, J. Chang, S. Cui, H. Pu, Z. Wen, and J. Chen, "Real-time, selective detection of Pb²⁺ in water using a reduced graphene oxide/gold nanoparticle field-effect transistor device," *ACS Applied Materials & Interfaces*, vol. 6, no. 21, pp. 19235-19241, 2014.
- [201] X. Ye, T. Jiang, Y. Ma, D. To, S. Wang, and J. Chen, "A portable, low-cost and high-throughput electrochemical impedance spectroscopy device for point-of-care biomarker detection," *Biosensors and Bioelectronics: X*, vol. 13, p. 100301, 2023.
- [202] M. Paeschke, U. Wollenberger, C. Köhler, T. Lisec, U. Schnakenberg, and R. Hintsche, "Properties of interdigital electrode arrays with different geometries," *Analytica Chimica Acta*, vol. 305, no. 1-3, pp. 126-136, 1995.
- [203] J. R. Scully and D. C. Silverman, *Electrochemical impedance: analysis and interpretation* (no. 1188). ASTM International, 1993.
- [204] S. MacKay, P. Hermansen, D. Wishart, and J. Chen, "Simulations of interdigitated electrode interactions with gold nanoparticles for impedance-based biosensing applications," *Sensors*, vol. 15, no. 9, pp. 22192-22208, 2015.
- [205] S. MacKay, G. N. Abdelrasoul, M. Tamura, D. Lin, Z. Yan, and J. Chen, "Using impedance measurements to characterize surface modified with gold nanoparticles," *Sensors*, vol. 17, no. 9, p. 2141, 2017.
- [206] Y. Ma *et al.*, "Improving immunoassay detection accuracy of anti-SARS-CoV-2 antibodies through dual modality validation," *Biosensors and Bioelectronics: X*, vol. 11, p. 100176, 2022.
- [207] B. Rigaud, J.-P. Morucci, and N. Chauveau, "Bioelectrical impedance techniques in medicine part I: bioimpedance measurement second section: impedance spectrometry," *Critical Reviews™ in Biomedical Engineering*, vol. 24, no. 4-6, 1996.

- [208] F. Lisdat and D. Schäfer, "The use of electrochemical impedance spectroscopy for biosensing," *Analytical and Bioanalytical Chemistry*, vol. 391, pp. 1555-1567, 2008.
- [209] K. R. Foster and H. P. Schwan, "Dielectric properties of tissues," *CRC Handbook of Biological Effects of Electromagnetic Fields*, pp. 27-96, 2019.
- [210] C. Tan, S. Lv, F. Dong, and M. Takei, "Image reconstruction based on convolutional neural network for electrical resistance tomography," *IEEE Sensors Journal*, vol. 19, no. 1, pp. 196-204, 2018.
- [211] J. Yao and M. Takei, "Application of process tomography to multiphase flow measurement in industrial and biomedical fields: A review," *IEEE Sensors Journal*, vol. 17, no. 24, pp. 8196-8205, 2017.
- [212] J. Guo, "Smartphone-powered electrochemical dongle for point-of-care monitoring of blood β -ketone," *Analytical Chemistry*, vol. 89, no. 17, pp. 8609-8613, 2017.
- [213] J. Guo and X. Ma, "Simultaneous monitoring of glucose and uric acid on a single test strip with dual channels," *Biosensors and Bioelectronics*, vol. 94, pp. 415-419, 2017.
- [214] J. Guo, "Uric acid monitoring with a smartphone as the electrochemical analyzer," *Analytical Chemistry*, vol. 88, no. 24, pp. 11986-11989, 2016.
- [215] A. Yúfera, A. Rueda, J. M. Muñoz, R. Doldán, G. Leger, and E. O. Rodríguez-Villegas, "A tissue impedance measurement chip for myocardial ischemia detection," *IEEE Transactions on Circuits and Systems I: Regular Papers*, vol. 52, no. 12, pp. 2620-2628, 2005.
- [216] C. Gabriel, S. Gabriel, and Y. Corthout, "The dielectric properties of biological tissues: I. Literature survey," *Physics in Medicine & Biology*, vol. 41, no. 11, p. 2231, 1996.

- [217] C. Gonzalez-Correa, B. Brown, R. Smallwood, T. Stephenson, C. Stoddard, and K. Bardhan, "Low frequency electrical bioimpedance for the detection of inflammation and dysplasia in Barrett's oesophagus," *Physiological Measurement*, vol. 24, no. 2, p. 291, 2003.
- [218] N. Beltran, G. Sanchez-Miranda, M. Godinez, U. Diaz, and E. Sacristan, "Gastric impedance spectroscopy in elective cardiovascular surgery patients," *Physiological Measurement*, vol. 27, no. 3, p. 265, 2006.
- [219] D. Naranjo-Hernández, J. Reina-Tosina, and M. Min, "Fundamentals, recent advances, and future challenges in bioimpedance devices for healthcare applications," *Journal of Sensors*, vol. 2019, 2019.
- [220] M. Reichmuth, S. Schürle, and M. Magno, "A non-invasive wearable bioimpedance system to wirelessly monitor bladder filling," in *2020 Design, Automation & Test in Europe Conference & Exhibition (DATE)*, 2020: IEEE, pp. 338-341.
- [221] M. T. Stratton *et al.*, "Longitudinal agreement of four bioimpedance analyzers for detecting changes in raw bioimpedance during purposeful weight gain with resistance training," *European Journal of Clinical Nutrition*, vol. 75, no. 7, pp. 1060-1068, 2021.
- [222] J. Ferreira, F. Seoane, and K. Lindecrantz, "Portable bioimpedance monitor evaluation for continuous impedance measurements. Towards wearable plethysmography applications," in *2013 35th Annual International Conference of the IEEE Engineering in Medicine and Biology Society (EMBC)*, 2013: IEEE, pp. 559-562.
- [223] N. Li, H. Xu, W. Wang, Z. Zhou, G. Qiao, and D. D. Li, "A high-speed bioelectrical impedance spectroscopy system based on the digital auto-balancing bridge method," *Measurement Science and Technology*, vol. 24, no. 6, p. 065701, 2013.

- [224] A. Ruiz-Vargas, J. Arkwright, and A. Ivorra, "A portable bioimpedance measurement system based on Red Pitaya for monitoring and detecting abnormalities in the gastrointestinal tract," in *2016 IEEE EMBS Conference on Biomedical Engineering and Sciences (IECBES)*, 2016: IEEE, pp. 150-154.
- [225] A. Kallel, D. Bouchaala, and O. Kanoun, "Critical implementation issues of excitation signals for embedded wearable bioimpedance spectroscopy systems with limited resources," *Measurement Science and Technology*, vol. 32, no. 8, p. 084011, 2021.
- [226] A. Hickling, "Studies in electrode polarisation. Part IV.—The automatic control of the potential of a working electrode," *Transactions of the Faraday Society*, vol. 38, pp. 27-33, 1942.
- [227] M. T. Koper, "Non-linear phenomena in electrochemical systems," *Journal of the Chemical Society, Faraday Transactions*, vol. 94, no. 10, pp. 1369-1378, 1998.
- [228] A. V. Oppenheim, A. S. Willsky, S. H. Nawab, and J.-J. Ding, *Signals and Systems*. Prentice hall Upper Saddle River, NJ, 1997.
- [229] M. Min, T. Parve, A. Ronk, P. Annus, and T. Paavle, "Synchronous sampling and demodulation in an instrument for multifrequency bioimpedance measurement," *IEEE Transactions on Instrumentation and Measurement*, vol. 56, no. 4, pp. 1365-1372, 2007.
- [230] T. Breugelmans *et al.*, "Odd random phase multisine EIS as a detection method for the onset of corrosion of coated steel," *Electrochemistry Communications*, vol. 12, no. 1, pp. 2-5, 2010.
- [231] M. Min, U. Pliquet, T. Nacke, A. Barthel, P. Annus, and R. Land, "Broadband excitation for short-time impedance spectroscopy," *Physiological Measurement*, vol. 29, no. 6, p. S185, 2008.

- [232] N. Lohmann, P. Weßkamp, P. Haußmann, J. Melbert, and T. Musch, "Electrochemical impedance spectroscopy for lithium-ion cells: Test equipment and procedures for aging and fast characterization in time and frequency domain," *Journal of Power Sources*, vol. 273, pp. 613-623, 2015.
- [233] P. Haußmann and J. Melbert, "Optimized mixed-domain signal synthesis for broadband impedance spectroscopy measurements on lithium ion cells for automotive applications," *Journal of Sensors and Sensor Systems*, vol. 6, no. 1, pp. 65-76, 2017.
- [234] J. Sihvo, D.-I. Stroe, T. Messo, and T. Roinila, "Fast approach for battery impedance identification using pseudo-random sequence signals," *IEEE Transactions on Power Electronics*, vol. 35, no. 3, pp. 2548-2557, 2019.
- [235] M. B. Howie, R. Dzwonczyk, and T. D. McSweeney, "An evaluation of a new two-electrode myocardial electrical impedance monitor for detecting myocardial ischemia," *Anesthesia & Analgesia*, vol. 92, no. 1, pp. 12-18, 2001.
- [236] E. Van der Ouderaa, J. Schoukens, and J. Renneboog, "Peak factor minimization of input and output signals of linear systems," *IEEE Transactions on Instrumentation and Measurement*, vol. 37, no. 2, pp. 207-212, 1988.
- [237] M. Schroeder, "Synthesis of low-peak-factor signals and binary sequences with low autocorrelation (Corresp.)," *IEEE transactions on Information Theory*, vol. 16, no. 1, pp. 85-89, 1970.
- [238] E. Van der Ouderaa, J. Schoukens, and J. Renneboog, "Peak factor minimization using a time-frequency domain swapping algorithm," *IEEE Transactions on Instrumentation and Measurement*, vol. 37, no. 1, pp. 145-147, 1988.

- [239] Y. Yang, F. Zhang, K. Tao, B. Sanchez, H. Wen, and Z. Teng, "An improved crest factor minimization algorithm to synthesize multisines with arbitrary spectrum," *Physiological Measurement*, vol. 36, no. 5, p. 895, 2015.
- [240] P. Guillaume, J. Schoukens, R. Pintelon, and I. Kollar, "Crest-factor minimization using nonlinear Chebyshev approximation methods," *IEEE Transactions on Instrumentation and Measurement*, vol. 40, no. 6, pp. 982-989, 1991.
- [241] A. Horner and J. Beauchamp, "A genetic algorithm - based method for synthesis of low peak amplitude signals," *The Journal of the Acoustical Society of America*, vol. 99, no. 1, pp. 433-443, 1996.
- [242] F. M. Janeiro, Y. Hu, and P. M. Ramos, "Peak factor optimization of multi-harmonic signals using artificial bee colony algorithm," *Measurement*, vol. 150, p. 107040, 2020.
- [243] J. Ojarand, M. Min, and P. Annus, "Crest factor optimization of the multisine waveform for bioimpedance spectroscopy," *Physiological Measurement*, vol. 35, no. 6, p. 1019, 2014.
- [244] J. Kennedy and R. Eberhart, "Particle swarm optimization," in *Proceedings of ICNN'95-International Conference on Neural Networks*, 1995, vol. 4: IEEE, pp. 1942-1948.
- [245] K. M. Passino, "Biomimicry of bacterial foraging for distributed optimization and control," *IEEE Control Systems Magazine*, vol. 22, no. 3, pp. 52-67, 2002.
- [246] D. Ensminger and L. J. Bond, *Ultrasonics: fundamentals, technologies, and applications*. CRC press, 2011.
- [247] D. L. Miller *et al.*, "Overview of therapeutic ultrasound applications and safety considerations," *Journal of Ultrasound in Medicine*, vol. 31, no. 4, pp. 623-634, 2012.

- [248] L. B. Feril and T. Kondo, "Biological effects of low intensity ultrasound: the mechanism involved, and its implications on therapy and on biosafety of ultrasound," *Journal of Radiation Research*, vol. 45, no. 4, pp. 479-489, 2004.
- [249] J. W. Busse, M. Bhandari, A. V. Kulkarni, and E. Tunks, "The effect of low-intensity pulsed ultrasound therapy on time to fracture healing: a meta-analysis," *Cmaj*, vol. 166, no. 4, pp. 437-441, 2002.
- [250] H. Shibaguchi, H. Tsuru, M. Kuroki, and M. Kuroki, "Sonodynamic cancer therapy: a non-invasive and repeatable approach using low-intensity ultrasound with a sonosensitizer," *Anticancer Research*, vol. 31, no. 7, pp. 2425-2429, 2011.
- [251] H. Baek, K. J. Pakk, and H. Kim, "A review of low-intensity focused ultrasound for neuromodulation," *Biomedical Engineering Letters*, vol. 7, pp. 135-142, 2017.
- [252] A. Bystritsky *et al.*, "A review of low-intensity focused ultrasound pulsation," *Brain Stimulation*, vol. 4, no. 3, pp. 125-136, 2011.
- [253] B. Xia, G. Chen, Y. Zou, L. Yang, J. Pan, and Y. Lv, "Low - intensity pulsed ultrasound combination with induced pluripotent stem cells - derived neural crest stem cells and growth differentiation factor 5 promotes sciatic nerve regeneration and functional recovery," *Journal of Tissue Engineering and Regenerative Medicine*, vol. 13, no. 4, pp. 625-636, 2019.
- [254] X.-Y. Zhou *et al.*, "Effects of low-intensity pulsed ultrasound on knee osteoarthritis: A meta-analysis of randomized clinical trials," *BioMed Research International*, vol. 2018, 2018.

- [255] S. M. Uddin and D. E. Komatsu, "Therapeutic potential low-intensity pulsed ultrasound for osteoarthritis: pre-clinical and clinical perspectives," *Ultrasound in Medicine & Biology*, vol. 46, no. 4, pp. 909-920, 2020.
- [256] T. El-Bialy *et al.*, "Effect of low intensity pulsed ultrasound (LIPUS) on tooth movement and root resorption: a prospective multi-center randomized controlled trial," *Journal of Clinical Medicine*, vol. 9, no. 3, p. 804, 2020.
- [257] X. Zhao *et al.*, "Low-intensity pulsed ultrasound (LIPUS) prevents periprosthetic inflammatory loosening through FBXL2-TRAF6 ubiquitination pathway," *Scientific Reports*, vol. 7, no. 1, p. 45779, 2017.
- [258] R. W. Poolman *et al.*, "Low intensity pulsed ultrasound (LIPUS) for bone healing: a clinical practice guideline," *BMJ*, vol. 356, 2017.
- [259] S. J. Warden, K. L. Bennell, J. M. McMeeken, and J. D. Wark, "Can conventional therapeutic ultrasound units be used to accelerate fracture repair?," *Physical Therapy Reviews*, vol. 4, no. 2, pp. 117-126, 1999.
- [260] B. G. Dijkman, S. Sprague, and M. Bhandari, "Low-intensity pulsed ultrasound: Nonunions," *Indian Journal of Orthopaedics*, vol. 43, no. 2, p. 141, 2009.
- [261] W. T. Ang *et al.*, "System-on-chip ultrasonic transducer for dental tissue formation and stem cell growth and differentiation," in *2008 IEEE International Symposium on Circuits and Systems (ISCAS)*, 2008: IEEE, pp. 1818-1821.
- [262] W. T. Ang, C. Scurtescu, W. Hoy, T. El-Bialy, Y. Y. Tsui, and J. Chen, "Design and implementation of therapeutic ultrasound generating circuit for dental tissue formation and tooth-root healing," *IEEE Transactions on Biomedical Circuits and Systems*, vol. 4, no. 1, pp. 49-61, 2009.

- [263] H. Kaur and T. El-Bialy, "Shortening of overall orthodontic treatment duration with low-intensity pulsed ultrasound (LIPUS)," *Journal of Clinical Medicine*, vol. 9, no. 5, p. 1303, 2020.
- [264] S. T. Ltd., "Piezoelectric material specifications," 2021. [Online]. Available: https://sensortechcanada.com/wp-content/uploads/2021/08/Piezo-spec-sheet_Final.pdf.
- [265] L. APC International, "ULTRASONIC POWER TRANSDUCERS," 2021. [Online]. Available: <https://www.americanpiezo.com/standard-products/ultrasonic-power-transducers.html>.
- [266] P. Instrumente, "Piezoelectric Disks," 2022. [Online]. Available: https://www.piusa.us/fileadmin/user_upload/physik_instrumente/files/datasheets/PRYY-Datasheet.pdf.
- [267] K. Hynynen, "MRI-guided focused ultrasound treatments," *Ultrasonics*, vol. 50, no. 2, pp. 221-229, 2010.
- [268] I. Schlesinger, A. Sinai, and M. Zaaroor, "MRI-guided focused ultrasound in Parkinson's disease: a review," *Parkinson's Disease*, vol. 2017, 2017.
- [269] A. Zafar *et al.*, "MRI - Guided High - Intensity Focused Ultrasound as an Emerging Therapy for Stroke: A Review," *Journal of Neuroimaging*, vol. 29, no. 1, pp. 5-13, 2019.
- [270] X. Jiang, X. Yu, K. Moez, D. G. Elliott, and J. Chen, "High-efficiency charge pumps for low-power on-chip applications," *IEEE Transactions on Circuits and Systems I: Regular Papers*, vol. 65, no. 3, pp. 1143-1153, 2017.
- [271] X. Jiang, W. T. Ng, and J. Chen, "A miniaturized low-intensity ultrasound device for wearable medical therapeutic applications," *IEEE Transactions on Biomedical Circuits and Systems*, vol. 13, no. 6, pp. 1372-1382, 2019.

- [272] M. Halesh, K. Rasane, and H. Rohini, "Design and implementation of voltage control oscillator (vco) using 180nm technology," in *Advances in Computing, Communication and Control: International Conference, ICAC3 2011, Mumbai, India, January 28-29, 2011. Proceedings*, 2011: Springer, pp. 472-478.
- [273] A. Hastings, *The art of analog layout*. Prentice Hall New Jersey, 2001.
- [274] A. Gopalan, E. Panneerselvam, G. T. Doss, K. Ponvel, and K. R. Vb, "Evaluation of Efficacy of Low Intensity Pulsed Ultrasound in Facilitating Mandibular Fracture Healing—A Blinded Randomized Controlled Clinical Trial," *Journal of Oral and Maxillofacial Surgery*, vol. 78, no. 6, pp. 997. e1-997. e7, 2020.
- [275] K. Shobara, T. Ogawa, A. Shibamoto, M. Miyashita, A. Ito, and R. M. Sitalaksmi, "Osteogenic effect of low - intensity pulsed ultrasound and whole - body vibration on peri - implant bone. An experimental in vivo study," *Clinical Oral Implants Research*, vol. 32, no. 5, pp. 641-650, 2021.
- [276] S. Xie *et al.*, "Low - intensity pulsed ultrasound promotes the proliferation of human bone mesenchymal stem cells by activating PI3K/AKt signaling pathways," *Journal of Cellular Biochemistry*, vol. 120, no. 9, pp. 15823-15833, 2019.
- [277] Z. Li, Y. Hua, J. Zhang, and Z. Fu, "Low-intensity pulsed ultrasound promotes the proliferation of bone marrow mesenchymal stem cells by inducing cyclin D1 up-regulation," *Chinese Journal of Tissue Engineering Research*, vol. 26, no. 13, p. 2006, 2022.
- [278] S.-P. Lin and M.-D. Ker, "Design of stage-selective negative voltage generator to improve on-chip power conversion efficiency for neuron stimulation," *IEEE*

- Transactions on Circuits and Systems I: Regular Papers*, vol. 67, no. 11, pp. 4122-4131, 2020.
- [279] K. Hofmann *et al.*, "Fully integrated high voltage charge pump for energy-efficient reconfigurable multi-band RF-transceivers," in *Intelec 2012*, 2012: IEEE, pp. 1-4.
- [280] A. Ballo, A. D. Grasso, and G. Palumbo, "A review of charge pump topologies for the power management of IoT nodes," *Electronics*, vol. 8, no. 5, p. 480, 2019.
- [281] J. K. Mai and G. Paxinos, *The Human Nervous System*. Academic press, 2011.
- [282] P. Y. Wen and J. T. Huse, "2016 World Health Organization classification of central nervous system tumors," *CONTINUUM: Lifelong Learning in Neurology*, vol. 23, no. 6, pp. 1531-1547, 2017.
- [283] E. A. Winkler, R. D. Bell, and B. V. Zlokovic, "Central nervous system pericytes in health and disease," *Nature Neuroscience*, vol. 14, no. 11, pp. 1398-1405, 2011.
- [284] L. R. Lizarraga - Valderrama, "Effects of essential oils on central nervous system: Focus on mental health," *Phytotherapy Research*, vol. 35, no. 2, pp. 657-679, 2021.
- [285] J. A. D'Andrea, C. Chou, S. A. Johnston, and E. R. Adair, "Microwave effects on the nervous system," *Bioelectromagnetics*, vol. 24, no. S6, pp. S107-S147, 2003.
- [286] G. McKhann, D. Drachman, M. Folstein, R. Katzman, D. Price, and E. M. Stadlan, "Clinical diagnosis of Alzheimer's disease: Report of the NINCDS - ADRDA Work Group* under the auspices of Department of Health and Human Services Task Force on Alzheimer's Disease," *Neurology*, vol. 34, no. 7, pp. 939-939, 1984.
- [287] M. Bains and E. D. Hall, "Antioxidant therapies in traumatic brain and spinal cord injury," *Biochimica et Biophysica Acta (BBA)-Molecular Basis of Disease*, vol. 1822, no. 5, pp. 675-684, 2012.

- [288] H. M. Bramlett and W. D. Dietrich, "Progressive damage after brain and spinal cord injury: pathomechanisms and treatment strategies," *Progress in Brain Research*, vol. 161, pp. 125-141, 2007.
- [289] D. Smajlović, "Strokes in young adults: epidemiology and prevention," *Vascular Health and Risk Management*, pp. 157-164, 2015.
- [290] P. Scheltens *et al.*, "Alzheimer's disease," *The Lancet*, vol. 388, no. 10043, pp. 505-517, 2016.
- [291] H. Seddon, "A classification of nerve injuries," *British Medical Journal*, vol. 2, no. 4260, p. 237, 1942.
- [292] H. Seddon, "Peripheral nerve injuries," *Glasgow Medical Journal*, vol. 139, no. 3, p. 61, 1943.
- [293] J. E. Schwob, "Neural regeneration and the peripheral olfactory system," *The Anatomical Record: An Official Publication of the American Association of Anatomists*, vol. 269, no. 1, pp. 33-49, 2002.
- [294] M. M. Steward, A. Sridhar, and J. S. Meyer, "Neural regeneration," *New Perspectives in Regeneration*, pp. 163-191, 2013.
- [295] J. Scheib and A. Höke, "Advances in peripheral nerve regeneration," *Nature Reviews Neurology*, vol. 9, no. 12, pp. 668-676, 2013.
- [296] A. Lavorato *et al.*, "Mesenchymal stem cell treatment perspectives in peripheral nerve regeneration: systematic review," *International Journal of Molecular Sciences*, vol. 22, no. 2, p. 572, 2021.
- [297] F.-J. Müller, E. Y. Snyder, and J. F. Loring, "Gene therapy: can neural stem cells deliver?," *Nature Reviews Neuroscience*, vol. 7, no. 1, pp. 75-84, 2006.

- [298] D. Joung, N. S. Lavoie, S. Z. Guo, S. H. Park, A. M. Parr, and M. C. McAlpine, "3D printed neural regeneration devices," *Advanced Functional Materials*, vol. 30, no. 1, p. 1906237, 2020.
- [299] A. Subramanian, U. M. Krishnan, and S. Sethuraman, "Development of biomaterial scaffold for nerve tissue engineering: Biomaterial mediated neural regeneration," *Journal of Biomedical Science*, vol. 16, pp. 1-11, 2009.
- [300] T. Gordon and A. W. English, "Strategies to promote peripheral nerve regeneration: electrical stimulation and/or exercise," *European Journal of Neuroscience*, vol. 43, no. 3, pp. 336-350, 2016.
- [301] J. Zhang *et al.*, "Conductive composite fiber with optimized alignment guides neural regeneration under electrical stimulation," *Advanced Healthcare Materials*, vol. 10, no. 3, p. 2000604, 2021.
- [302] C. L. Romano, D. Romano, and N. Logoluso, "Low-intensity pulsed ultrasound for the treatment of bone delayed union or nonunion: a review," *Ultrasound in Medicine & Biology*, vol. 35, no. 4, pp. 529-536, 2009.
- [303] J. Nakao *et al.*, "Low-intensity pulsed ultrasound (LIPUS) inhibits LPS-induced inflammatory responses of osteoblasts through TLR4–MyD88 dissociation," *Bone*, vol. 58, pp. 17-25, 2014.
- [304] Y. Iwanabe *et al.*, "The effect of low-intensity pulsed ultrasound on wound healing using scratch assay in epithelial cells," *Journal of Prosthodontic Research*, vol. 60, no. 4, pp. 308-314, 2016.
- [305] A. Bernal *et al.*, "Low-intensity pulsed ultrasound improves the functional properties of cardiac mesoangioblasts," *Stem Cell Reviews and Reports*, vol. 11, pp. 852-865, 2015.

- [306] C. Li *et al.*, "Wireless electrical stimulation at the nanoscale interface induces tumor vascular normalization," *Bioactive Materials*, vol. 18, pp. 399-408, 2022.
- [307] Y. Tsehay *et al.*, "Low-intensity pulsed ultrasound neuromodulation of a rodent's spinal cord suppresses motor evoked potentials," *IEEE Transactions on Biomedical Engineering*, 2023.
- [308] E.-D. Kim *et al.*, "Efficacy and safety of a stimulator using low-intensity pulsed ultrasound combined with transcutaneous electrical nerve stimulation in patients with painful knee osteoarthritis," *Pain Research and Management*, vol. 2019, 2019.
- [309] Y. Lv, P. Nan, G. Chen, Y. Sha, B. Xia, and L. Yang, "In vivo repair of rat transected sciatic nerve by low-intensity pulsed ultrasound and induced pluripotent stem cells-derived neural crest stem cells," *Biotechnology Letters*, vol. 37, pp. 2497-2506, 2015.
- [310] L. Zhao, Y. Feng, H. Hu, A. Shi, L. Zhang, and M. Wan, "Low-intensity pulsed ultrasound enhances nerve growth factor-induced neurite outgrowth through mechanotransduction-mediated ERK1/2-CREB-Trx-1 signaling," *Ultrasound in Medicine & Biology*, vol. 42, no. 12, pp. 2914-2925, 2016.
- [311] P. S. Green, K. E. Gridley, and J. W. Simpkins, "Estradiol protects against β -amyloid (25-35)-induced toxicity in SK-N-SH human neuroblastoma cells," *Neuroscience Letters*, vol. 218, no. 3, pp. 165-168, 1996.
- [312] X. Wang, E. Perez, R. Liu, L.-J. Yan, R. T. Mallet, and S.-H. Yang, "Pyruvate protects mitochondria from oxidative stress in human neuroblastoma SK-N-SH cells," *Brain Research*, vol. 1132, pp. 1-9, 2007.
- [313] S. Zhou, D. Zhang, J. Guo, Z. Chen, Y. Chen, and J. Zhang, "Deficiency of NEAT1 prevented MPP⁺-induced inflammatory response, oxidative stress and apoptosis in

- dopaminergic SK-N-SH neuroblastoma cells via miR-1277-5p/ARHGAP26 axis," *Brain Research*, vol. 1750, p. 147156, 2021.
- [314] Y. Pang *et al.*, "Inhibiting autophagy pathway of PI3K/AKT/mTOR promotes apoptosis in SK-N-sh cell model of Alzheimer's disease," *Journal of Healthcare Engineering*, vol. 2022, 2022.
- [315] R. A. Saxton and D. M. Sabatini, "mTOR signaling in growth, metabolism, and disease," *Cell*, vol. 168, no. 6, pp. 960-976, 2017.
- [316] R. Roskoski Jr, "ERK1/2 MAP kinases: structure, function, and regulation," *Pharmacological Research*, vol. 66, no. 2, pp. 105-143, 2012.
- [317] B. D. Manning and L. C. Cantley, "AKT/PKB signaling: navigating downstream," *Cell*, vol. 129, no. 7, pp. 1261-1274, 2007.
- [318] C. R. Bramham and E. Messaoudi, "BDNF function in adult synaptic plasticity: the synaptic consolidation hypothesis," *Progress in Neurobiology*, vol. 76, no. 2, pp. 99-125, 2005.
- [319] K. Hensel, M. P. Mienkina, and G. Schmitz, "Analysis of ultrasound fields in cell culture wells for in vitro ultrasound therapy experiments," *Ultrasound in Medicine & Biology*, vol. 37, no. 12, pp. 2105-2115, 2011.
- [320] D. Debanne, E. Campanac, A. Bialowas, E. Carlier, and G. Alcaraz, "Axon physiology," *Physiological Reviews*, vol. 91, no. 2, pp. 555-602, 2011.
- [321] H. Guo *et al.*, "Exploratory study on neurochemical effects of low-intensity pulsed ultrasound in brains of mice," *Medical & Biological Engineering & Computing*, vol. 59, pp. 1099-1110, 2021.